BERGISCHE
UNIVERSITÄT
WUPPERTAL

Data Processing and Trace Gas Retrievals for the GLORIA Limb Sounder

Dissertation

zur Erlangung des Grades

Doktor der Naturwissenschaften (Dr. rer. nat.)

vorgelegt der

Bergischen Universität

Wuppertal

Fachbereich C – Mathematik und Naturwissenschaften

von

Tobias Guggenmoser

Wuppertal 2014

Die Dissertation kann wie folgt zitiert werden:

urn:nbn:de:hbz:468-20150401-153714-6
[http://nbn-resolving.de/urn/resolver.pl?urn=urn%3Anbn%3Ade%3Ahbz%3A468-20150401-153714-6]

IGNORANTI QVEM PORTVM PETAT
NVLLVS SVVS VENTVS EST

"No wind favours him who knows not for which port he sails."

Seneca the Younger
Moral Letters to Lucilius, LXXI

Abstract

The chemical composition of the Upper Troposphere and Lower Stratosphere (UTLS) region and the dynamical processes occurring within it have a particularly strong effect on radiative forcing, and hence surface climate. A lack of quantitative understanding of the region around the tropopause, and especially of exchange of trace constituents between the stratosphere and the troposphere, severely limits the predictive capabilities of current climate models. More and spatially better resolved observations are needed in order to close this gap.

To this end, the *Gimballed Limb Observer for Radiance Imaging of the Atmosphere* (GLORIA) was developed in a collaboration between the German research centres *Forschungszentrum Jülich GmbH* and *Karlsruher Institut für Technologie*.GLORIA is the descendant of the highly successful MIPAS and CRISTA instruments and has been designed with both chemical and dynamical analysis of the UTLS in mind.

The imaging technology utilised by GLORIA and the resulting high data rate present unprecedented opportunities for data analysis, but also challenges for the processing of the recorded measurements. In this work, a new integrated data processing system designed for GLORIA is presented, as well as novel techniques for calibration and diagnosis.

As an application of the new data processing chain, a polar flight from the combined TACTS/ESMVal campaign is presented which was performed on September 23rd, 2012, along a trajectory mostly above the Scandinavian peninsula. A selection of measurements from this flight is processed into calibrated spectra and then analysed further using the JURASSIC2 retrieval processor. Retrieved cross-sections of ozone, nitric acid, water vapour and atmospheric temperature are shown and compared with calculations from the Chemical Lagrangian Model of the Stratosphere (CLaMS), as well as potential vorticity from the European

Centre for Medium-Range Weather Forecasts (ECMWF). The measurements reveal a highly inhomogeneous UTLS region suggesting that tropospheric air masses have been transported into the polar stratosphere, which is also indicated by the ECMWF data and further supported by CLaMS trajectory calculations. Two main structures can be identified. One is an anticyclone resulting from a mid-latitude wave-breaking event that transported tropospheric air into the observed region. The other is a vertically confined cyclone of seemingly stratospheric origin. The results are a successful application of both the newly-developed processing chain as well as the GLORIA instrument itself and highlights GLORIA's ability to observe the effect of dynamic and transport processes in the UTLS.

Kurzfassung

Die chemische Zusammensetzung der oberen Troposphäre und unteren Stratosphäre (UTLS[1]) und die dynamischen Prozesse, welche sich in dieser Region abspielen, nehmen großen Einfluss auf den Strahlungsantrieb, und mithin auf das Oberflächenklima. Ein mangelndes quantitatives Verständnis des Bereichs um die Tropopause, und hierbei insbesondere im Hinblick auf den Austausch von Spurenstoffen zwischen Stratosphäre und Troposphäre, begrenzt stark die Vorhersagekraft derzeitiger Klimamodelle. Mehr und räumlich besser aufgelöste Beobachtungen sind vonnöten, um diese Lücke zu schließen.

Zu diesem Zwecke wurde der *Gimballed Limb Observer for Radiance Imaging of the Atmosphere*[2] (GLORIA) entwickelt. GLORIA stellt ein Gemeinschaftsprojekt der deutschen Forschungszentren *Forschungszentrum Jülich GmbH* und *Karlsruher Institut für Technologie* dar. Es tritt in die Nachfolge der höchst erfolgreichen MIPAS- und CRISTA-Instrumente und wurde für die chemische und dynamische Analyse der UTLS gleichermaßen ausgelegt.

Die von GLORIA verwendete abbildende Technologie und die sich aus dieser ergebende hohe Datenrate bieten beispiellose Möglichkeiten für die Datenanalyse, stellen jedoch die Verarbeitung der aufgenommenen Messungen auch vor neue Herausforderungen. In dieser Arbeit wird ein neues, integriertes Datenverarbeitungssystem für GLORIA vorgestellt, zusammen mit neuartigen Techniken für die Kalibration und Diagnose.

Als Anwendung der neuen Prozessierungskette wird ein polarer Forschungsflug gezeigt, welcher am 23. September 2012 im Rahmen der TACTS/ESMVal-Messkampagne hauptsächlich oberhalb der skandinavischen Halbinsel durchgeführt wurde. Eine Auswahl von Messungen

[1] engl. *Upper Troposphere and Lower Stratosphere*

[2] zu deutsch etwa "Kardanischer Horizontsondierer für abbildende Strahlungsmessungen in der Atmosphäre"

dieses Fluges wird zu kalibrierten Spektren verarbeitet und dann unter Verwendung des JURASSIC2-Retrieval-Prozessors weiter analysiert. Abgeleitete Querschnitte für Ozon, Salpetersäure und Wasserdampf, sowie für die atmosphärische Temperatur, werden gezeigt und mit Rechnungen des Chemical Lagrangian Model of the Stratosphere (CLaMS), sowie mit Daten für die potentielle Vortizität, welche vom European Centre for Medium-Range Weather Forecasts (ECMWF) bereitgestellt wurden, verglichen. Die Messungen offenbaren eine in hohem Maße inhomogene UTLS-Region, welche einen vorangegangenen Transport troposphärischer Luftmassen in die polare Stratosphäre nahelegt. Dieser Schluss wird weiter bestärkt durch den Verlauf von mit CLaMS berechneten Rückwärtstrajektorien. Zwei hauptsächliche Strukturen können ausgemacht werden. Die eine ist ein Antizyklon, welcher von einem Wellenbrechereignis in den mittleren Breiten herrührt, die andere ist ein vertikal begrenzter Zyklon scheinbar stratosphärischen Ursprungs. Die Ergebnisse stellen eine erfolgreiche Anwendung sowohl der neu entwickelten Verarbeitungskette als auch des GLORIA-Instrumentes selbst dar und verdeutlicht die Fähigkeit desselben, die Auswirkungen dynamischer Vorgänge und Transportprozesse in der UTLS-Region zu beobachten.

Contents

1. Introduction

The earth's radiation budget is of particular scientific and societal interest. This is especially true in the context of climate change, which might drastically alter living and economic conditions on a global level. Accurate predictions of the earth's climate are necessary to evaluate this process and its impact on the biosphere. The driving factor of this change is *radiative forcing*, which determines the amount of thermal energy trapped near the surface by the greenhouse effect.

The atmospheric layers and the boundary regions between them are especially important for the atmosphere as a whole and the surface in particular. The *upper troposphere and lower stratosphere* (UTLS) region is one of these boundaries. Its most prominent feature is the *tropopause* which separates the troposphere and stratosphere, two atmospheric layers with very different physical properties and chemical composition. The stratosphere is statically stabilised by its positive vertical temperature gradient. This gradient is caused by the prevalence of UV-absorbing ozone in this layer, and suppresses vertical convection. The resulting stratification is in stark contrast to the troposphere, where air masses mix at a much faster rate (e.g. Roedel and Wagner, 2011).

Over the past years, research has shown that radiative forcing is especially sensitive to changes in UTLS trace gas and aerosol distributions (Solomon et al., 2007). Moreover, existing uncertainties for the region's composition contribute greatly to uncertainties in global climate forecasts (Riese et al., 2012). At the same time, the UTLS is also a region of high dynamic activity, and especially of mixing between stratospheric and tropospheric air masses (*stratosphere-troposphere exchange* or STE). In addition to the slow up- and downwelling of the Brewer-Dobson circu-

lation, STE also happens on much smaller scales in the form of isentropic transport across the extratropical tropopause and Rossby wave breaking events (Holton et al., 1995). More and spatially better resolved observations of the UTLS region are necessary to improve our understanding of these processes so that they can be adequately accounted for in climate models (Gettelman et al., 2011).

All candidate techniques for these observations fall into either of two categories: *in situ* or *remote sensing* measurements. In situ measurements are taken at the location of the observed air mass and typically offer very good spatial resolution. However, what they offer in sampling they lose in spatial coverage as the instrument can only measure one location at a given time. Consequently, while these measurements provide valuable high-density samples along a specific path, they can only be interpreted within the context of larger-scale data for the surrounding regions, e.g. model calculations.

Remote sensing instruments, on the other hand, typically make the opposite trade-off. Deployed on aircraft, balloons or satellites, they can observe large volumes of air from afar. However, due to the distance to their target, spatial resolution is traditionally limited – often in the range of several kilometres in the vertical, depending on direction and viewing geometry. What is needed for the examination of the UTLS are instruments that offer wide spatial coverage together with excellent resolution.

This requirement is fulfilled by the Gimballed Limb Observer for Radiance Imaging of the Atmosphere (GLORIA), developed jointly by the German research centres Forschungszentrum Jülich GmbH (FZJ) and Karlsruher Institut für Technologie (KIT). GLORIA is the successor of the CRISTA-NF and MIPAS-STR airborne infrared limb sounders. The former was primarily designed for the study of dynamic and transport processes with very fine spatial sampling in the vertical. CRISTA-NF data from the AMMA and RECONCILE measurement campaigns have been used to derive trace gas volume mixing ratios with unprecedented vertical resolution (Ungermann et al., 2012, 2013). MIPAS-STR, on

the other hand, was designed for a chemistry-centred analysis, offering a higher spectral resolution in order to derive more elusive trace gases (Woiwode et al., 2012).

Both of GLORIA's precursor instruments can themselves look back at a proud heritage of successful earth observation. MIPAS-STR is a sister instrument to both the MIPAS-B balloon limb sounder (Friedl-Vallon et al., 2004) and the Envisat MIPAS variant (Fischer et al., 2008). MIPAS-B has provided and continues to provide a multitude of observations especially in the polar regions (Oelhaf et al., 1994). The MIPAS instrument on board the European Space Agency's Envisat orbiter operated through the entirety of the spacecraft's ten-year mission, yielding a wealth of data still being analysed under ever new aspects. For instance, novel detection algorithms for volcanic aerosol have only recently been developed and successfully applied to this data set (Griessbach et al., 2014).

CRISTA-NF is an airborne modification of the original instrument which was deployed twice on the CRISTA-SPAS spacecraft. CRISTA was released into low-earth orbit during the NASA Space Shuttle missions STS-66 (OV-104 Atlantis, 1994) and STS-85 (OV-103 Discovery, 1997). During each mission, CRISTA recorded eight days of atmospheric measurements in the altitude region between 15-150 km. Several studies with different scientific focus have been performed on these two data sets. STS-66 data have been used to show significant variability in the middle atmosphere on horizontal scales smaller than 1,000 km (Offermann et al., 1999; Riese et al., 1997). The second mission, STS-85, revealed trace gas variability in the stratosphere which could be linked to planetary waves (Riese et al., 2002). In both data sets, thin cirrus clouds around the tropopause could be detected due to the instrument's excellent spatial resolution, providing insight into one of the most significant uncertainties in radiative forcing (Spang et al., 2002). Through assimilation of CRISTA observations into a chemical transport model, understanding of the dynamical context in which the measurements were made could be enhanced further (Riese et al., 1999b, 2000).

The GLORIA instrument builds upon the design of both MIPAS and CRISTA to enable both chemical and dynamical analysis of the atmosphere with unprecedented spatial resolution. This is achieved by combining a Michelson-type interferometer with a focal plane array and a gimbal frame with inertial attitude control. The result is an *infrared limb imager* capable of measuring thousands of spectra at once while staying precisely directed at its target volume. The gimbal frame also provides the ability to pan the instrument in between measurements so that the same target volume can be measured from many directions. This makes 3D tomographic data analysis possible, yielding trace gas distributions with unprecedented horizontal resolution of about 25 km without compromising the several hundred metres resolution in the vertical. These tomographic techniques have been developed specifically for GLORIA by Ungermann et al. (2010b) as an extension of the JURASSIC retrieval processor (Hoffmann et al., 2005). Chemistry-oriented measurements, on the other hand, take longer to record and are not suited for this type of analysis. Their advantage is their spectral resolution which is finer by an order of magnitude, enabling the retrieval of more elusive trace gases. These analyses are performed at KIT using the KOPRA radiative transfer model and associated KOPRAFIT retrieval processor (Stiller, 2000; Höpfner et al., 1998).

Before these retrievals can be performed, be they based on JURASSIC or KOPRAFIT, the recorded raw measurements first have to be processed into calibrated spectral radiances. This is achieved at the Level-0 and Level-1 stages of data processing. During GLORIA's initial development, existing software solutions for the Level-0 and Level-1 processing from MIPAS-STR and MIPAS-B were adapted for GLORIA. However, the processing chain was still far from operational at this point. The instrument's high data acquisition rate of over 70 MiBs/s means that a single measurement can be GiB-sized, and a complete flight can be between 1–2 TiBs large. In order to work with these amounts of data, an efficient, highly automated and flexible processing environment and associated tools are necessary.

For this work, the existing Level-0 and Level-1 processing components were highly modified and partially reimplemented to form an integrated processing suite. This software system, called *gloripy*, provides a unified framework for the development of GLORIA processing software. It also provides, for the first time, an automated programme which is able to process GLORIA raw data into calibrated spectra, without intermediate human intervention. As the terminal point of this chain for dynamics mode measurements, the JURASSIC2 retrieval processor was extended with a preprocessing module that prepares the calibrated measurements for the actual trace gas retrieval. Once these new tools were available, they were applied to the extensive data set gathered during the TACTS/ESMVal campaign in the summer of 2012. In addition to the results presented in this work, *gloripy* also enabled the first ever tomographic retrievals of GLORIA measurements (Blank, 2014).

This thesis is laid out as follows. In chapter 2, the measurement technique employed by GLORIA is presented. The principles of *Fourier transform spectrometry* are introduced to explain the relationship between GLORIA measurements and the atmospheric radiation. It is also described briefly how this radiation arrives at the instrument via the process of *radiative transfer*. Finally, the chapter introduces the theory behind the *inversion* or *retrieval* process which is used to obtain atmospheric variables, e.g. trace gas volume mixing ratios, from the measured spectra.

In chapter 3, an overview of the GLORIA instrument is given. The history of its development, its core components and main features is introduced. Additionally, the two measurement campaigns, i.e. ESSenCe (2011) and TACTS/ESMVal (2012) as well as the two carrier aircraft used by GLORIA are presented. The goal of this chapter is to familiarise the reader with how the principles laid out in chapter 2 are implemented on the instrument's side, and how the raw data at the beginning of the processing chain are acquired.

The GLORIA data processing chain, consisting of the Level-0, Level-1 and Level-2 stages, is described in chapter 4. This chapter is central

to this work. It introduces the basic principles behind the Level-0 and Level-1 processing stages, as well as the newly-developed *gloripy* software suite which integrates and builds upon all the components. New techniques for the generation of calibration data that are specific to GLORIA are given, as well as the preprocessing of the calibrated spectra for the JURASSIC2 retrieval processor.

These new tools and techniques are then applied to one of the scientifically most interesting flights from the TACTS/ESMVal campaign, which is presented in chapter 5. The flight in question was conducted on September 23rd, 2012, between the campaign base at Oberpfaffenhofen, Germany, and the northern polar regions, up to a latitude of 80° N. Level-2 results from the JURASSIC2 retrieval processor for a selection of measurements are shown and compared with simulations from the *Chemical Lagrangian Model of the Stratosphere* (CLaMS). Using trajectory simulations and auxiliary data from the *European Centre for Medium Range Weather Forecasts* (ECMWF), the observations are set in the context of the synoptic situation. This chapter highlights GLORIA's ability to produce highly resolved measurements of trace gas distributions in the UTLS, as well as the potential of the extensive TACTS/ESMVal data set which will be scientifically analysed in the coming years.

2. Measurement Technique

GLORIA is a remote sensing instrument, i.e. it provides information about targeted air masses at a distance. Its observations are therefore, by their very nature, *indirect measurements*. This chapter serves to introduce the fundamentals of the measurement technique upon which GLORIA is based. The relation between the atmospheric radiation and the recorded signal is derived, and it is explained how information about the target volume can be retrieved from the signal. How these principles are implemented on the hardware and software side is discussed further in subsequent chapters.

2.1. Fourier Spectroscopy

2.1.1. Simplified Instrument Model

The GLORIA instrument contains, as its core, a Michelson-type Fourier transform spectrometer (FTS) with a focal plane array for imaging. In order to understand the GLORIA data processing chain put forward in this work, some knowledge about this kind of instrument is necessary. This section will therefore discuss a simple model of the Michelson-type FTS and derive the relationship between measured radiation and instrument output. An extensive discussion of the FTS principle which includes a discussion of non-ideal instruments has been given by Beer (1992).

In principle, an instrument such as GLORIA can be understood as a variation of the apparatus developed for the Michelson-Morley ex-

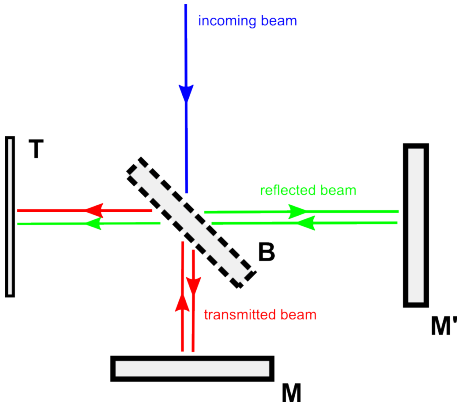

Figure 2.1.: *Simplified schematic of a Michelson-type Fourier transform spectrometer. The incoming light arrives at the beamsplitter B, where it is partially transmitted and partially reflected. The transmitted beam (red) is then reflected once at the fixed mirror M, and again at B until it finally arrives at the detector T. The reflected beam (green) is reflected at the moving mirror M', then transmitted at the beamsplitter before it hits the detector. At the target point T, the rays are recombined. The "red" ray has travelled a path of $2\overline{BM} + \overline{BT}$, whereas the "green" ray has covered a distance of $2\overline{BM'} + \overline{BT}$. The difference $\Delta s = 2\left(\overline{BM'} - \overline{BM}\right)$ is called the* optical path difference. *Upon recombination, Δs manifests as a phase shift between the two components, resulting in wave interference at the detector T.*

periment (see Michelson and Morley, 1887).[1] Different from grating spectrometers, which operate by diffracting incoming light and then sampling the spectrum, the FTS instead measures interference patterns in the spatial domain. To illustrate this, consider the schematic in figure 2.1. The simplified instrument presented here consists of a detector T, two mirrors M and M', and a beamsplitter B. Different from Michelson and Morley's classical experiment, the second mirror M' is mounted on

[1] The experiment is famous for its role in disproving the hypothesis of the "luminiferous aether" and paving the way towards the special theory of relativity developed later by Einstein (1905). It was honoured in 1907 with the Nobel Prize in Physics for Michelson.

a slide and thus movable. This is the simplest design and also the one employed by GLORIA. Other instruments, e.g. MIPAS, use different ones wherein both mirrors move. All these devices, however, implement the same basic measurement principle.

Due to the linear nature of Maxwell's equations, any light entering the optical path can be described as a linear combination of monochromatic waves of the form

$$y(x,t) = A\mathrm{e}^{i(kx-\omega t)} \tag{2.1}$$

where A is the wave's amplitude, k is the wavenumber and ω is the angular frequency. At the beamsplitter B, this wave is now split into two parts. For the sake of simplicity, it is assumed that the beamsplitter itself has vanishing emissivity. Futhermore, assume that the wave's energy is split equally with each pass, i.e. that the beamsplitter's reflexivity is exactly 50%.

In the end, both beams have been transmitted once and reflected twice when they arrive at the detector T. The first beam, which is transmitted and then reflected at the fixed mirror M, will always travel the distance D to the detector T. The second beam, reflected into and out of the arm with the moving mirror M', travels a distance $D + \Delta s = D + 2\Delta x$, where Δx is the position of M' with respect to the point of equal length with the fixed-mirror arm. The doubled distance Δs is called the *optical path difference* (OPD). Without loss of generality, let the detector be at $x = 0$. At this point, the recombined wave will take the form

$$\tilde{y}(t) = \frac{1}{2}\left(y(0,t) + y(\Delta s, t)\right) \tag{2.2}$$

$$= \frac{1}{2}A\mathrm{e}^{i\omega t}\left(1 + \mathrm{e}^{ik\Delta s}\right) \tag{2.3}$$

The factor $1/2$ is due to both incoming beams having passed the beamsplitter twice in the end. A factor of $1/2$ in the energy corresponds to a factor of $1/\sqrt{2}$ in the wave's amplitude. This factor being applied twice yields the result of $1/2$.

The actual signal registered by the detector is proportional to the incoming *intensity*:

$$I(t) = (\tilde{y}^* \cdot \tilde{y})(t) = \frac{1}{4}A^2(1 + \mathrm{e}^{ik\Delta s})(1 + \mathrm{e}^{-ik\Delta s}) \tag{2.4}$$

$$= \frac{1}{4}A^2(1 + \cos(k\Delta s)) \tag{2.5}$$

Introducing the *spectroscopic wavenumber* ν as the inverse of the wavelength λ, and using the dispersion relation for electromagnetic waves in a vacuum, k can be rewritten as

$$k = 2\pi\nu \tag{2.6}$$

For a fixed optical path difference Δs, the intensity is constant, which motivates the reformulation

$$I(\Delta s) = A^2(1 + \cos(2\pi\nu\Delta s)) \tag{2.7}$$

If the mirror M' is moved uniformly at a constant rate $v/2$, the optical path difference simply becomes

$$\Delta s = vt \tag{2.8}$$

Consequently, eq. (2.4) can be reexpressed with an explicit time dependency:

$$I(t) = A^2(1 + \cos(2\pi\nu vt)) \tag{2.9}$$

This intensity, which corresponds directly to the electric signal output of the detector, is conveniently separated into a constant or *unmodulated* and a *modulated* term. The unmodulated term is commonly referred to as the *DC component* and the modulated term as the *AC component*, owing to the nature of the electric detector signals they produce. The DC component is not relevant for spectrometric purposes and is eventually removed from the signal. This can be accomplished either using a

hardware-implemented highpass filter or at the software level during a later processing stage. GLORIA itself does not filter the DC component, which means that it is available in the early stages of data processing. This is useful for various non-spectrometric purposes, e.g. for infrared imaging (see section 4.5.1).

The AC component, on the other hand, can be understood as an oscillation whose frequency is determined by the frequency of the input wave and the interferometer's optical path velocity. It thus contains information about the incident light's frequency in an encoded form.

To gain further insight, consider now a continuous spectrum of radiation such as would be expected from an atmospheric measurement. In the interest of brevity, let the optical path difference from now on be called $x = \Delta s$. The intensity at the detector can then be expressed as a superposition of constituent signals of the form (2.7):

$$I(x) = \int_0^\infty a(\nu)(1 + \cos(2\pi\nu x))\mathrm{d}\nu \tag{2.10}$$

The weighting function a introduced here is called the *spectral radiance*. Let now a be symmetrically extended, i.e. $a(-\nu) = a(\nu)$ for all wavenumbers ν. The cosine function is naturally of the same even symmetry. Therefore, (2.10) can be written as:

$$I(x) = \frac{1}{2}\int_{-\infty}^\infty a(\nu)(1 + \cos(2\pi\nu x))\mathrm{d}\nu \tag{2.11}$$

$$= \frac{1}{2}\int_{-\infty}^\infty a(\nu)\mathrm{d}\nu + \frac{1}{2}\int_{-\infty}^\infty a(\nu)\cos(2\pi\nu x)\mathrm{d}\nu \tag{2.12}$$

$$= \mathrm{DC} + \frac{1}{4}\left(\int_{-\infty}^\infty a(\nu)\mathrm{e}^{i2\pi\nu x}\mathrm{d}\nu + \int_{-\infty}^\infty a(\nu)\mathrm{e}^{-i2\pi\nu x}\mathrm{d}\nu\right) \tag{2.13}$$

In this form, it becomes clear that the AC component of the signal intensity I is the *Fourier cosine transform*, i.e. a symmetrised *Fourier transform* of the spectrum $a(\nu)$. Exploiting the symmetry of a, one finds that the two integrals are of equal value. Therefore, one can reexpress (2.13) using either the regular or the inverse Fourier transform:

$$I(x) = \mathrm{DC} + \frac{1}{2}\int_{-\infty}^{\infty} a(\nu)\mathrm{e}^{-i2\pi\nu x}\mathrm{d}\nu = \mathrm{DC} + \frac{1}{2}\int_{-\infty}^{\infty} a(\nu)\mathrm{e}^{i2\pi\nu x}\mathrm{d}\nu \quad (2.14)$$

This relationship between the recorded measurements and the incoming spectrum is the distinguishing and defining property of Fourier transform spectrometry. More complicated instrument designs exist but still result in the same mathematical relation. It follows that the recorded signal must be subjected to another Fourier transform in order to retrieve the radiance spectrum $a(\nu)$.

2.1.2. Finite Interferogram Length and Instrument Line Shape

Each point in the interferogram contains information about the entire spectrum. In theory, the relationship is symmetrical, i.e. the spectrum a can be reconstructed from the AC signal $\tilde{I}$ via the inverse Fourier transform

$$a(\nu) = \int_{-\infty}^{\infty} \tilde{I}(x)\mathrm{e}^{i2\pi\nu x}\mathrm{d}x \quad (2.15)$$

For simplicity, the convention-dependent Fourier normalisation factor has been absorbed into $\tilde{I}$. In practice, the integration cannot be carried out in this fashion because the recorded interferogram is, naturally, of finite length, with a maximum optical path difference (MOPD) of L.

Interferometers can principally record one- or two-sided interferograms. One-sided interferograms range from OPD $x = 0$ to $x = L$.

GLORIA falls into the second category and records two-sided interferograms ranging from $x = -L$ to $x = +L$. The inverse transform can therefore be performed only within these limits:

$$a(\nu) = \int_{-L}^{L} \tilde{I}(x) \mathrm{e}^{i2\pi\nu x} \mathrm{d}x \tag{2.16}$$

This can be brought back into the form of a full Fourier integral using the *rectangular function* rect to limit the support of the integrand to the range $[-L, L]$:

$$a(\nu) = \int_{-\infty}^{\infty} \mathrm{rect}\left(\frac{x}{2L}\right) \tilde{I}(x) \mathrm{e}^{i2\pi\nu x} \mathrm{d}x \tag{2.17}$$

$$= 2L \left(\left(\nu' \mapsto \mathrm{sinc}\left(2L\nu'\right)\right) * \left(\nu' \mapsto \int_{-\infty}^{\infty} \tilde{I}(x) \mathrm{e}^{i2\pi\nu' x} \mathrm{d}x \right) \right) (\nu) \tag{2.18}$$

In the last expression, the Fourier convolution theorem was utilised to separate the rectangular function from the interferogram; the transform can then be written as a convolution (symbolised by the asterisk) of the Fourier transforms of the two functions. The functions themselves are defined by the mapping (symbolised by the arrow), and the *cardinal sine function*

$$\mathrm{sinc} : \mathbb{R} \to \mathbb{R}, \qquad x \mapsto \frac{\sin(\pi x)}{\pi x} \tag{2.19}$$

was introduced as the Fourier transform of the rectangular function. Equation (2.17) highlights an important feature of Fourier transform spectrometry: the spectrum retrieved from a real-life measurement device, which can necessarily only record finite-length interferograms, is effectively a convolution of the true spectrum with the sinc-function.

To illustrate this effect, consider a spectrum consisting of a single peak, i.e. the Fourier transform of a perfectly monochromatic wave. In this case, (2.17) is a convolution of the sinc-function with a delta distribution, and the result is another sinc-function centered around the original peak position. The cardinal sine can thus be interpreted as the response function of the spectrometer to spectral lines, which is why it is referred to as the *instrument line shape* or ILS.[2]

The ILS due to the limited interferogram length has two main effects on the spectrum. Firstly, peaks in the spectrum are smeared out, i.e. their energy is spread wider than it is in the source spectrum. This results in a *limited spectral resolution*. Secondly, it causes *sidelobes* to appear in the spectrum in addition to the main peaks, i.e. any given peak's energy is distributed not only over one, but infinitely many spectral ranges, although strongly reduced with growing distance from the peak position. The strength of both effects depends, of course, on the length of the interferogram (see fig. 2.2): peaks in longer interferograms are localised better than in short interferograms, approaching a perfect delta peak as L approaches infinity. For illustration, the sinc-functions plotted in fig. 2.2 correspond to the two operational modes used by the GLORIA interferometer. The nonlocality of spectral peaks is a problem for the subsequent data analysis, especially for the trace gas retrieval (see section 2.3), because it introduces correlations between distant regions of the spectrum that are difficult to account for. To counteract this effect, the spectrum is usually convolved with another function, called an *apodisation function*.[3] Apodisation suppresses the spectrum's sidelobes, but comes at the cost of a further diminished spectral resolution.

[2] Note that this is strictly the case only for the ideal interferometer discussed in this section. The ILS for a real device is a sinc-function modified by the properties of the instrument's optical components. For the GLORIA instrument, the ILS has been analysed in detail by Kretschmer (2014).

[3] The term *apodisation* comes from the Greek ἄ-ποδος, meaning "footless", from ποῦς ("foot"). This refers to the sidelobes, or "feet", being suppressed or removed by the apodisation process.

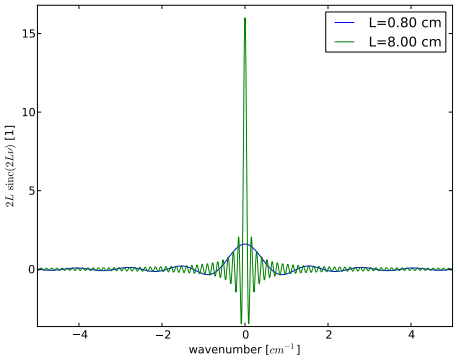

Figure 2.2.: *Cardinal sine functions plotted for varying interferogram lengths L. The two values shown correspond to GLORIA chemistry (*8.0 cm*) and dynamics mode (*0.8 cm*). The short interferogram length causes a wider central peak and sidelobes, while the peak in the long interferogram is much better localised, resulting in a better spectral resolution.*

In practice, the convolution is usually replaced by a pointwise multiplication of the interferogram with the apodisation function's Fourier transform.

2.1.3. Spectral Resolution

The spectral resolution $\delta\nu$ of a Fourier spectrometer is given by the full width at half maximum (FWHM) of the instrument line shape. For a sinc-function as discussed in the previous section, this results in (see Beer, 1992)

$$\delta\nu \approx \frac{0.603}{L} \tag{2.20}$$

However, this relation is valid only for the *non-apodised* spectrum. The resolution of the apodised spectrum depends on the particular choice of apodisation function. Several of these functions have been discussed in the literature (see Naylor and Tahic, 2007). For GLORIA interferograms, the "strong" variant of the *Norton-Beer apodisation* function

(Norton and Beer, 1976) is employed:

$$\mathrm{NB}(x) = \sum_{i=0}^{4} \alpha_i \left(1 - \left(\frac{x}{L}\right)^2\right)^i \tag{2.21}$$

is used, where $\alpha_0 = 0.045335$, $\alpha_1 = \alpha_3 = 0$, $\alpha_2 = 0.554883$ and $\alpha_4 = 0.399782$. This function is multiplied with the interferogram, corresponding to a convolution in the spectrum. The effect is a dampening of the ILS sidelobes, at the cost of spectral resolution. The resolution in the case of the Norton-Beer-strong apodisation is

$$\delta\nu_{\mathrm{apo}} \approx 1.6\,\delta\nu \approx \frac{0.96}{L} \approx \frac{1}{L} \tag{2.22}$$

The standard MOPD values for GLORIA are 0.8 cm (dynamics mode) and 8.0 cm (chemistry mode), implying an apodised spectral resolution of $1.2\,\mathrm{cm}^{-1}$ and $0.12\,\mathrm{cm}^{-1}$, respectively.

2.1.4. Discrete Sampling

The interference patterns generated by the interferometer are continuous in nature. However, the practical implementation of the data acquisition system is limited to discrete sampling of the detector signal. Let Δx be the *spatial sampling*, i.e. the distance between two optical path differences after which a new sample is recorded. The *maximum optical path difference* (MOPD) L then determines the number of samples N:

$$N = \frac{2L}{\Delta x} \tag{2.23}$$

This discretisation also necessitates application of the *discrete Fourier transform* or DFT (see appendix B.1) instead of the continuous trans-

form. The *spectral sampling* of the resulting spectrum is

$$\Delta\nu = \frac{1}{2L} \approx \frac{1}{2}\delta\nu_{\text{apo}} \tag{2.24}$$

where $\delta\nu_{\text{apo}}$ is the apodised spectral resolution according to eq. (2.22). A naïve application of the DFT results in a complex-valued spectrum which is of the same length N as the interferogram. Because the latter consists entirely of *real* values, however, the spectrum exhibits Hermitian symmetry. This means that half of the spectrum consists of the complex conjugates of the other half and carries no independent information (see appendix B.1.2). In practice, specific DFT algorithms are used that are optimised for real input data.

2.1.5. Complex Spectra

The Fourier transform needs both the positive and negative spatial axis as its input. In the case of one-sided interferograms from $x = 0$ to $x = L$, one would assume hypothetical two-sided interferogram to be perfectly symmetrical. The recorded data would be accordingly extended and the transform applied to this extended interferogram. Because real symmetry around the origin is a special case of Hermitian symmetry for real values, the corresponding spectrum would be strictly real-valued, as expected from an electromagnetic radiance spectrum.

In practice, one finds that the two-sided interferograms measured by instruments such as GLORIA are not perfectly symmetric, which results in nonvanishing imaginary parts in the spectrum. This is also to be expected because, like every measurement, the detector signal is subject to noise. However, the spectra do not show only a random imaginary component but also include systematic nonreal signals.

Although the presence of imaginary radiances might seem unphysical at first, it is entirely due to physical reasons. The simplest one is that the discrete sampling of the interferogram does not perfectly match its symmetry. In other words, the point of zero optical path difference (ZOPD)

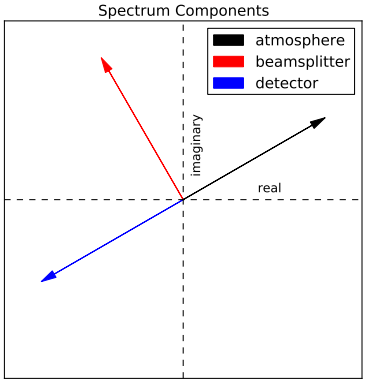

Figure 2.3.: *Components of the complex spectrum. The dashed lines represent the real and imaginary axes of the measured signal, and the principal components are rotated with respect to the measurement at three distinct angles: the atmospheric port, the beamsplitter port and the detector port. During the Level-1 processing stage, the atmospheric signal is rotated into the positive real axis via complex multiplication. The beamsplitter emissions then make up the imaginary part of the spectrum, and the detector contributes negatively to the real part.*

generally lies in between two interferogram samples, which results in a shift of the entire interferogram and breaks its Hermitian symmetry. The direct effect of this is a *linear phase component* in the spectrum, as shown in appendix B.1.3. This linear phase is different for each measurement. In the case of GLORIA, it is corrected for automatically in the earliest stages of the data processing (see section 4.4.5).

In addition, a more detailed treatment of the interferometer must take into account that the optical components within exhibit nonzero emissivity in the infrared. It has been shown that, due to a different number of transmissions and reflections, their thermal emissions enter the spectrum at different phase angles with respect to the atmospheric signal (see Trieschmann, 2000). The relation between these components in the complex plane is illustrated in fig. 2.3. Three distinct phase angles exist at which signals enter the spectrum. The first is called the *atmospheric*

port and encompasses the radiance from the observed atmosphere, as well as instrument emissions from the same side of the interferometer, e.g. those stemming from the instrument's external window. The second component is the *beamsplitter port* and is rotated against the atmospheric port at an angle of $\frac{\pi}{2}$. It consists mainly of thermal emission and absorption from the beamsplitter itself. The third component, the *detector port*, consists of signals generated by the instrument at the detector's side of the interferometer. This includes emissions from the instrument's housing as well as the detector seeing its own reflection as it is returned from the beamsplitter. The detector port is rotated another $\frac{\pi}{2}$ with respect to the beamsplitter port, i.e. π with respect to the atmospheric port. These components are implicitly separated at the Level-1 processing stage by calibration with a complex-valued instrument response function (see section 4.2.1).

2.2. Atmospheric Radiative Transfer

2.2.1. Trace Gas Emissions

Trace constituents inside the atmosphere emit a characteristic spectrum of electromagnetic radiation. Many species of interest, such as ozone (O_3) and carbon dioxide (CO_2), have emission lines in the thermal infrared range. The line shape associated with each excitation state of a given emitter is a function of atmospheric temperature and pressure. Parameters for these functions can be calculated theoretically or obtained from laboratory measurements. Data for a multitude of emitters are commonly aggregated in databases for easier access from radiative transfer algorithms. For the spectral range covered by the GLORIA instrument, one very comprehensive and periodically updated collection of transmission and emission data is *HITRAN* (Rothman et al., 2009), maintained and distributed by the Harvard-Smithsonian Center for Astrophysics. The database is the default source of line strength parameters for the radiative transfer calculations performed for GLORIA

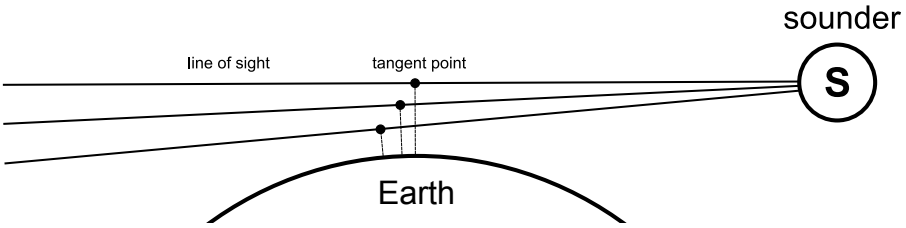

Figure 2.4.: *Schematic of the limb sounding geometry realised by GLORIA. The instrument's lines of sight follow a mostly horizontal, relatively long path through the atmosphere and end in space. The point nearest to the earth along these trajectories are the tangent points. This schematic neglects the influence of refraction, which would otherwise result in a slightly curved path, and the earth's curvature is exaggerated for clarity.*

trace gas retrievals.

2.2.2. Limb Geometry

A characteristic property of any remote sensing instrument is the measurement geometry it employs. Satellite instruments are often directed towards the earth's surface, whereas ground stations are usually pointed upwards into the atmosphere. These vertical viewing geometries are referred to as *nadir sounding* and *zenith sounding*, using the traditional Arabic terms for the two orientations.

GLORIA, on the other hand, is an instance of a *horizontal* viewing geometry, a technique referred to as *limb sounding*. A simplified schematic of limb geometry is shown in figure 2.4. The instrument's line of sight is horizontal, usually with a small downward component. Along any such line of sight, there is a point that is nearest to the earth's surface, called the *tangent point*. Due to the exponential decay of atmospheric density with altitude, the concentrations of trace gases, and therefore also their emissions, are heavily weighted around this point.

The main benefit of limb sounding, compared with nadir and zenith geometries, is that it allows for a finer vertical resolution. On the other

hand, horizontal resolution along the line of sight is traditionally limited. One of GLORIA's main features is *dynamics mode*, where quick measurements are combined with panning of the azimuth angle in between the observations. This mode allows GLORIA to image the same volume of air from multiple directions, thereby obtaining enough information for a full 3D-tomographic data analysis. Using tomographic techniques, horizontal resolution can be improved by an order of magnitude (Ungermann, 2011; Blank, 2014).

2.2.3. Radiative Transfer

The transfer of electromagnetic radiation along a path through a gaseous atmosphere is determined by *Schwarzschild's equation*.[4] If the effects of scattering are negligible, it can be written in the form of the differential equation

$$\frac{\mathrm{d}I}{\mathrm{d}s} = \beta_a(B - I) \tag{2.25}$$

where I is the intensity of the radiation, s is the position along the path, β_a is the absorption (and emission) coefficient, and B is the Planck function. Schwarzschild's equation was first formulated for a discussion of radiation within the solar atmosphere (Schwarzschild, 1914) and describes the contribution of each infinitesimal line element along a light ray to the total radiative intensity.

In order to find the radiance at the end of such a line of sight, (2.25) has to be integrated along its trajectory (e.g. Petty, 2006). It is conve-

[4] Schwarzschild's equation is not to be confused with the perhaps more widely known Schwarzschild metric, the solution for Einstein's equations for a spherically symmetric mass distribution (Schwarzschild, 1916).

nient to introduce the *optical path*

$$\tau(s) = \int_{s}^{S} \mathrm{d}s' \beta_a(s')$$
$$\tau(S) = 0 \tag{2.26}$$

where S is now used to denote the end of the ray, i.e. in practice the position of the instrument sensor. A coordinate substitution and subsequent integration of (2.25) yields

$$I(0) = I(\tau_0)\exp(-\tau_0) + \int_{\tau_0}^{0} \mathrm{d}\tau B \exp(-\tau) \tag{2.27}$$

where τ_0 is the starting point of the integration, and the sensor is located at $\tau(s) = \tau(S) = 0$. The integration constant $I(\tau_0)\exp(-\tau_0)$ is the background radiation whose value depends on the viewing geometry.

For a limb sounder such as GLORIA, the line of sight starts in deep space. In this case, the background term can therefore be omitted, provided the integration is started at a very high pressure altitude where emission can already be neglected. For nadir sounders, the term corresponds to the radiation coming from the earth's surface. For lunar or solar occultation measurements, the brightness temperature and emission characteristics of the respective celestial body have to be taken into account.

2.3. Inversion of Atmospheric Emission Spectra

2.3.1. The Problem

In the previous section, the propagation of infrared emissions through the atmospheric medium was discussed. Based on these fundamentals

and a more or less extensive set of simplifying assumptions, it is possible to develop mathematical models of the radiative transfer. Implemented as computer programmes, these models can subsequently be used to predict the incoming radiance from a specific direction at a specific point in space and time, given a definite atmospheric input state. In the context of atmospheric remote sensing, the output of such a model can be understood as a simulation of the radiance arriving at an instrument situated at the respective location and looking in the given direction. If the instrument's expected response to the radiance is incorporated into the model, then the output is a *simulated measurement*, or a theoretical *prediction* of a measurement taken inside the input atmosphere. For reasons which will become clear later on, such a model is called a *forward model*.

Consider now a model atmosphere consisting of n real-valued parameters. Such parameters could, for instance, be trace gas volume mixing ratios and temperature values on a discrete spatial grid. Any atmospheric state, i.e. any configuration of this model atmosphere, can then be represented by its *state vector* $\boldsymbol{x} \in \mathbb{R}^n$. Let now $\boldsymbol{F}$ be a forward model specialised to the particular set of parameters at hand, i.e. the n parameters of the model atmosphere introduced above. Then $\boldsymbol{F}$ can be considered a function

$$\boldsymbol{F} : \mathbb{R}^n \to \mathbb{R}^m, \qquad \boldsymbol{x} \mapsto \boldsymbol{F}(\boldsymbol{x}) \tag{2.28}$$

mapping atmospheric states $\boldsymbol{x}$ to their predicted measurements $\boldsymbol{F}(\boldsymbol{x}) \in \mathbb{R}^m$. The dimension m of the function $\boldsymbol{F}$'s image depends on how the measurement process is defined. For instance, in the case of a spectrometer, m could be a chosen number of spectral points to be simulated by $\boldsymbol{F}$.

In the next step, consider an *actual measurement* taken by the instrument which is simulated by $\boldsymbol{F}$. Let the measurement be accordingly represented by m parameters chosen to correspond to the output of the model $\boldsymbol{F}$, in the form of the *measurement vector* $\boldsymbol{y} \in \mathbb{R}^m$. One is

now usually interested in the atmospheric configuration that lead to the measurement $\boldsymbol{y}$ rather than in the measurement itself. In other words, what is needed is a model akin to an *inverse* of $\boldsymbol{F}$: a function $\boldsymbol{F}^{-1}$ mapping measurement vectors $\boldsymbol{y}$ to atmospheric states $\boldsymbol{F}^{-1}(\boldsymbol{y})$. This desired model is called the *inverse model* corresponding to the forward model $\boldsymbol{F}$.

Note that, in practice, the forward model will most often require more parameters than are to be retrieved. In the interest of simplicity, such parameters are factored out of the atmospheric state vector $\boldsymbol{x}$, and instead considered intrinsic parameters of $\boldsymbol{F}$ in this section. To illustrate this, consider a situation where atmospheric infrared emissions are recorded, but only the volume mixing ratios of ozone are of interest. The volume mixing ratios of other trace gases, as well as physical parameters like pressure and temperature, will still be necessary in order to compute the simulated measurements. However, as long as these parameters are not to be retrieved by the inverse model, they will not be considered part of the atmospheric state, but rather constants of the model itself. These non-retrieved parameters are, of course, only known to a finite precision and must therefore be considered again when the total error budget is calculated.

In general, finding an inverse model in the form of a function $\boldsymbol{F}^{-1}$ is not possible. The simple reason is that the function $\boldsymbol{F}$ is generally not a bijection: there may be more than one state vector $\boldsymbol{x}$ corresponding to a particular measurement $\boldsymbol{y}$. The problem is further complicated by the presence of measurement errors, which imply that $\boldsymbol{y}$ will not be the exact value of the forward model for the true atmospheric state $\boldsymbol{x}_t$, even if $\boldsymbol{F}$ were a "perfect" model of the physical measurement process.

Mathematically speaking, the problem of finding the inverse to the foward model $\boldsymbol{F}$ is an *ill-posed* problem. Therefore, the true atmospheric state $\boldsymbol{x}_t$ corresponding to a measurement $\boldsymbol{y}$ has to be found by an approximate *numerical inversion* of the forward model $\boldsymbol{F}$ at the point $\boldsymbol{y}$.

This problem can be reformulated as an optimisation problem where

the solution vector $\boldsymbol{x}_f \approx \boldsymbol{x}_t$ is identified with a minimum of an appropriately chosen function. This technique is further explained in the next subsection, following an inductive or "bottom-up" approach, meaning that mathematical concepts will first be motivated and then introduced as necessary. Rodgers (2000) has given an extensive and mathematically much more rigorous treatment of inverse problems in atmospheric remote sensing.

2.3.2. Cost Functions

Quantifying Solution Fitness

In the previous subsection, the *inverse problem* at the heart of remote sensing was introduced. In the following, this problem will be restated in terms of optimising (minimising) a quantity akin to a distance between an atmospheric state vector $\boldsymbol{x}$ and the true state $\boldsymbol{x}_t$, given a forward model $\boldsymbol{F}$ as introduced in the previous section. This can obviously not be done directly as the true state $\boldsymbol{x}_t$ is unknown.

Instead, one can compare the mapped value $\boldsymbol{F}(\boldsymbol{x})$ with the measured value $\boldsymbol{y}$, i.e. the comparison is done in measurement space instead of state space. The measured value $\boldsymbol{y}$ is identified with the mapped value of the true state, i.e. $\boldsymbol{y} \approx \boldsymbol{F}(\boldsymbol{x_t})$. In reality, however, this is not precisely true. The function $\boldsymbol{F}$ itself cannot fully model the physical measurement process with infinite precision. Likewise, the measurements themselves can only be recorded with a finite error margin. Therefore, the measurement $\boldsymbol{y}$ is more accurately represented as

$$\boldsymbol{y} = \boldsymbol{F}(\boldsymbol{x_t}) + \epsilon \tag{2.29}$$

where $\epsilon \in \mathbb{R}^m$ is the vector of measurement errors[5].

As a means of quantifying the proximity of a given state $\boldsymbol{x}$ to the true

[5]The term "error" here means the actual (unknown) deviation of the measurement from the true value, not to be confused with statistical notions of error used later.

state $\boldsymbol{x}_t$, one can construct a real-valued *cost function*

$$J : \mathbb{R}^n \to \mathbb{R}, \qquad \boldsymbol{x} \mapsto J(\boldsymbol{x}) \tag{2.30}$$

Note that while terms such as "distance" and "proximity" have been used here in a tentative sense, these are not to be understood in the mathematically strict sense as defined on a metric space or a Riemannian manifold.

For further illustration, consider the perhaps simplest example of such a function:

$$\begin{aligned} J_{L_2}(\boldsymbol{x}) &= |\boldsymbol{y} - \boldsymbol{F}(\boldsymbol{x})|^2 \\ &= \langle \boldsymbol{y} - \boldsymbol{F}(\boldsymbol{x}) |\, \boldsymbol{y} - \boldsymbol{F}(\boldsymbol{x}) \rangle \\ &= (\boldsymbol{y} - \boldsymbol{F}(\boldsymbol{x}))^T \, \mathbf{I}_m \, (\boldsymbol{y} - \boldsymbol{F}(\boldsymbol{x})) \end{aligned} \tag{2.31}$$

where $\mathbf{I}_m \in \mathbb{R}^{m \times m}$ is the m-dimensional identity matrix. This cost function is just the standard Euclidean L_2 norm of the difference between the simulated measurement for the state vector $\boldsymbol{x}$ and the actual measurement vector $\boldsymbol{y}$.

In practice, the measurement vector $\boldsymbol{y}$ will contain quantities with non-uniform uncertainties. For instance, the entries of the vector could be values measured by different detectors, or a signal from the same detector at several wavelengths, etc. The uncertainties for these quantities can vary by orders of magnitude, implying that the Euclidean metric, which treats each component of the vector with the same weight, is non-ideal. In other words, the cost function in (2.31) will punish deviations in all components equally, even if some of them can be *expected* to be much less exactly known than the others. Ideally, one would want to give less weight to deviations in poorly known components, and high weight to deviations from measurements one believes to be very exact.

For this reason, it is better to use a cost function that reflects the knowledge about measurement error margins. Let $\sigma_i^2 \in \mathbb{R}$ be the variance associated with the i-th component of $\boldsymbol{y}$. Consider then a new cost

function given by

$$\begin{aligned} J_{\tilde{S}}(\boldsymbol{x}) &= \|\boldsymbol{y} - \boldsymbol{F}(\boldsymbol{x})\|^2_{\tilde{\mathbf{S}}} \\ &= \langle \boldsymbol{y} - \boldsymbol{F}(\boldsymbol{x}) |\, \boldsymbol{y} - \boldsymbol{F}(\boldsymbol{x}) \rangle_{\tilde{\mathbf{S}}} \\ &= (\boldsymbol{y} - \boldsymbol{F}(\boldsymbol{x}))^T\, \tilde{\mathbf{S}}\, (\boldsymbol{y} - \boldsymbol{F}(\boldsymbol{x})) \end{aligned} \tag{2.32}$$

where $\tilde{\mathbf{S}} \in \mathbb{R}^{m \times m}$ is a diagonal matrix with entries

$$\tilde{\mathbf{S}}_{ii} = \frac{1}{\sigma_i^2} \tag{2.33}$$

The new metric defined by the matrix $\tilde{\mathbf{S}}$ effectively rescales the individual components of the vectors $\boldsymbol{y}$ and $\boldsymbol{F}(\boldsymbol{x})$ such that their difference is now measured in multiples of the measurements' standard deviation.

Note that, in principle, the measurements in $\boldsymbol{y}$ could now even stem from multiple instrument types, with each device recording a different quantity than the others, and in different units. The rescaling will strip the components of their physical dimension. This is not important for the inversion problems described here for GLORIA, but e.g. for the field of data assimilation, which uses similar mathematical techniques to integrate diverse measurements and model predictions into an optimally consistent state.

The cost function $J_{\tilde{\mathbf{S}}}$ still does not account for *correlations* between the components of the measurement vector. Consider the symmetrical *measurement error covariance matrix* $\mathbf{S}_\epsilon \in \mathbb{R}^{m \times m}$, with entries of the form

$$(\mathbf{S}_\epsilon)_{ij} = \sigma_{ij} = \sigma_{ji} \tag{2.34}$$

Each entry is the covariance of two of the m measurement vector components, and the main diagonal is filled with the variances:

$$(\mathbf{S}_\epsilon)_{ii} = \sigma_{ii} = \sigma_i^2 \tag{2.35}$$

This property precludes negative eigenvalues and thus ensures that the matrix $\mathbf{S}_\epsilon$ is at least positive semidefinite. In this work, vanishing variances will not occur; neither will cases where any two measurements are fully correlated. $\mathbf{S}_\epsilon$ will therfore be assumed to be a positive definite matrix, and consequently invertible, with its inverse $\mathbf{S}_\epsilon^{-1}$ also being a positive definite matrix.

Substituting the inverse measurement covariance matrix $\mathbf{S}_\epsilon^{-1}$ for $\tilde{\mathbf{S}}$, one obtains the cost function

$$\begin{aligned} J_m(\boldsymbol{x}) &= \|\boldsymbol{y} - \boldsymbol{F}(\boldsymbol{x})\|^2_{\mathbf{S}_\epsilon^{-1}} \\ &= \langle \boldsymbol{y} - \boldsymbol{F}(\boldsymbol{x}) |\, \boldsymbol{y} - \boldsymbol{F}(\boldsymbol{x}) \rangle_{\mathbf{S}_\epsilon^{-1}} \\ &= (\boldsymbol{y} - \boldsymbol{F}(\boldsymbol{x}))^T \, \mathbf{S}_\epsilon^{-1} \, (\boldsymbol{y} - \boldsymbol{F}(\boldsymbol{x})) \end{aligned} \tag{2.36}$$

This cost function is now an adequate means of judging the deviation of a simulated measurement $\boldsymbol{F}(\boldsymbol{x})$ from an actual measurement $\boldsymbol{y}$, and thus, indirectly, of the deviation of $\boldsymbol{x}$ from the true atmospheric state $\boldsymbol{x_t}$. The *trace gas retrieval*, i.e. the derivation of atmospheric state parameters from remote sensing measurements, consists mostly of finding a minimum of this cost function.

However, because of the uncertainties in the measurements and the forward model itself, there will not be an exact and unique solution to this problem. Using the pure cost function constructed in (2.36), any minimisation algorithm applied to J_m will probably converge on an unphysical solution, or not converge at all. As has been mentioned in the previous subsection, this is known mathematically as an ill-posed problem. A class of so-called *regularisation techniques* can be applied to transform this exact, but ill-posed problem into a slightly inexact, but well-posed problem.

Regularisation

Regularisation, in the context of remote sensing, is usually performed by modifying the cost function in order to impose a physically motivated constraint on the solution. For instance, one can have the cost function punish a deviation of the solution from an *a priori* state, derived from model calculations or climatologies. Let $\boldsymbol{x_a}$ be such an a priori state, and let $\mathbf{S_a} \in \mathbb{R}^{n\times n}$ be its associated *a priori error covariance matrix*. Instead of the cost function J_m introduced in eq. 2.36, consider the function

$$\begin{aligned} J(\boldsymbol{x}) &= J_m(\boldsymbol{x}) + J_r(\boldsymbol{x}) \\ &= \|\boldsymbol{y} - \boldsymbol{F}(\boldsymbol{x})\|^2_{\mathbf{S}_\epsilon^{-1}} + \|\boldsymbol{x} - \boldsymbol{x_a}\|^2_{\mathbf{S}_a^{-1}} \\ &= (\boldsymbol{y} - \boldsymbol{F}(\boldsymbol{x}))^T \mathbf{S}_\epsilon^{-1} (\boldsymbol{y} - \boldsymbol{F}(\boldsymbol{x})) + (\boldsymbol{x} - \boldsymbol{x_a})^T \mathbf{S}_a^{-1} (\boldsymbol{x} - \boldsymbol{x_a}) \end{aligned} \tag{2.37}$$

If the matrix $\mathbf{S}_a$ contains actual estimates of covariances, the resulting retrieval technique is called the *optimal estimation approach*. However, in many cases, an accurate covariance matrix cannot be found. In other cases, it may exist but the bias it introduces in the result is found to be excessive.

An alternative method of regularisation, and the one which will be employed for the trace gas retrievals in this work, is *Tikhonov* or *Tikhonov-Twomey* regularisation (Tikhonov and Arsenin, 1977; Twomey, 1977). The cost function J retains the same form as in the optimal estimation approach (2.37). However, the matrix $\mathbf{S}_a$ is not constructed from physical covariances and subsequently inverted. Instead, the regularisation matrix $\mathbf{S}_a^{-1}$ itself, or a root $\mathbf{S}_a^{-1/2}$, is constructed *ad hoc* in order to constrain the set of possible solutions in a more general way. A useful and physically reasonable constraint to impose on the solution is that it be smooth according to some smoothness metric.

If $\mathbf{D} \in \mathbb{R}^{n\times n}$ is a finite-difference operator along an appropriately chosen axis, then $(\mathbf{D}\xi)^T(\mathbf{D}\xi) = \xi^T(\mathbf{D}^T\mathbf{D})\xi$ is a measure of the smooth-

ness of $\xi \in \mathbb{R}^n$ along this axis. For a state vector $\boldsymbol{x}$ containing trace gas volume mixing ratios, for instance, one could construct a difference operator along the vertical axis for each gas, constraining the result to smooth vertical profiles. For a 2D, 3D or 4D problem, the other space (and time) axes can be added as necessary.

In general, the Tikhonov matrix $\mathbf{S}_a^{-1}$ will assume the form

$$\mathbf{S}_a^{-1} = \alpha_0^2 (\mathbf{D}^{(0)})^T (\mathbf{D}^{(0)}) + \sum_{k,l} \alpha_{kl}^2 (\mathbf{D}_l^{(k)})^T (\mathbf{D}_l^{(k)}) \tag{2.38}$$

where $\mathbf{D}_l^{(k)}$ is the k-th order difference operator along the l-th axis, and α_{kl}^2 are real-valued summation weights. The 0-th order operator $\mathbf{D}^{(0)}$ can just be an identity matrix, or an inverse covariance matrix. The latter case can be seen as a combination of the optimal estimation approach described above and the Tikhonov regularisation technique. Several ways of constructing $\mathbf{S}_a^{-1}$ have been examined by Steck and von Clarmann (2001) for the Envisat MIPAS orbital limb sounder, which shares technical similarities with GLORIA.

2.3.3. Retrieval of the Atmospheric State Vector

The true atmospheric state $\boldsymbol{x}_t$ is approximated by a solution $\boldsymbol{x}_f$ that minimises the cost function J (see eq. 2.37) discussed in the previous subsection. For $\boldsymbol{x}_f$ to be a minimum of J, a necessary condition is that the gradient of J vanish:

$$\boldsymbol{J}'(\boldsymbol{x}_f) = \left.\frac{\partial J}{\partial \xi}\right|_{\xi=\boldsymbol{x}_f} = \mathbf{o} \in \mathbb{R}^n \tag{2.39}$$

As both $\mathbf{S}_\epsilon^{-1}$ and $\mathbf{S}_a^{-1}$ in (2.37) are positive definite and symmetric, the cost function J is a sum of two inner products, i.e. the product rule

applies for their derivatives:

$$\boldsymbol{J}'(\boldsymbol{x}) = -2(\boldsymbol{y} - \boldsymbol{F}(\boldsymbol{x}))^T \mathbf{S}_\epsilon^{-1} \mathbf{F}'(\boldsymbol{x}) + 2(\boldsymbol{x} - \boldsymbol{x_a})^T \mathbf{S}_a^{-1} \mathbf{I}_n \tag{2.40}$$

A root of $\boldsymbol{J}'$ can be found e.g. by using some variant of Newton's algorithm. Several minimisation algorithms have been examined for GLORIA retrievals by Ungermann (2011). A basic and powerful one has been found to be the *Gauss-Newton algorithm* (Nocedal and Wright, 1999). It can be understood as a modification of the standard Newton procedure wherein terms containing the Hessian of the function F are neglected. This approximation negatively affects convergence in cases where the forward model is highly nonlinear, but greatly reduces the computational effort required.

Newton's algorithm is an iterative method based on a linear approximation of the function at any given iteration point $\boldsymbol{x}_i$:

$$\begin{aligned} J(\boldsymbol{x}) &= J(\boldsymbol{x}_i) + \boldsymbol{J}'(\boldsymbol{x}_i)(\boldsymbol{x} - \boldsymbol{x}_i) + \mathcal{O}\left((\boldsymbol{x} - \boldsymbol{x}_i)^2\right) \\ &= T(\boldsymbol{x}) + \mathcal{O}\left((\boldsymbol{x} - \boldsymbol{x}_i)^2\right) \end{aligned} \tag{2.41}$$

The root of the tangent function T is then used as the next iteration step:

$$\boldsymbol{x}_{i+1} = \boldsymbol{x}_i - (\boldsymbol{J}'(\boldsymbol{x_i}))^{-1} \boldsymbol{J}(\boldsymbol{x_i}) \tag{2.42}$$

Using the Gauss-Newton approximation $\mathbf{F}'' \approx \mathbf{0}$, the derivative of $\boldsymbol{J}'$ becomes

$$\begin{aligned} \mathbf{J}''(x) &= -2(\boldsymbol{y} - \boldsymbol{F}(\boldsymbol{x}))^T \mathbf{F}''(\boldsymbol{x}) + 2\mathbf{F}'(\boldsymbol{x})^T \mathbf{S}_\epsilon^{-1} \mathbf{F}'(\boldsymbol{x}) + \mathbf{S}_a^{-1} \\ &\approx 2\mathbf{S}_a^{-1} + 2\mathbf{F}'(\boldsymbol{x})^T \mathbf{S}_\epsilon^{-1} \mathbf{F}'(\boldsymbol{x}) \end{aligned} \tag{2.43}$$

and thus the the Gauss-Newton iteration is given by

$$\begin{aligned}\boldsymbol{x}_{i+1} &= \boldsymbol{x}_i - (\mathbf{J}''(\boldsymbol{x}_i))^{-1}\boldsymbol{J}'(\boldsymbol{x}_i) \\ &\approx \boldsymbol{x}_i - \Big\{ \left[\mathbf{S}_a^{-1} + \mathbf{F}'(\boldsymbol{x}_i)^T\mathbf{S}_\epsilon^{-1}\mathbf{F}'(\boldsymbol{x}_i)\right]^{-1} \\ &\qquad \cdot \left[-(\boldsymbol{y} - \boldsymbol{F}(\boldsymbol{x}_i))^T\mathbf{S}_\epsilon^{-1}\mathbf{F}'(\boldsymbol{x}_i) + (\boldsymbol{x}_i - \boldsymbol{x_a})^T\mathbf{S}_a^{-1}\right] \Big\}\end{aligned} \tag{2.44}$$

As the starting point of the iteration, $\boldsymbol{x}_0$, called the *initial guess*, usually the a priori state is chosen. The idea behind this is that $\boldsymbol{x}_a$ will already be a vector reasonably close to the true state.

The inverse of the Hessian $(\mathbf{J}''(\boldsymbol{x}_i))^{-1}$ is calculated in each step by using the *Conjugate Gradient* method (see Nocedal and Wright, 1999) to iteratively solve the associated linear equation system. In practice, the Gauss-Newton iteration has to be modified because the inverse of the Hessian $\mathbf{J}''$ does not always exist. This is done by adding a positive-definite matrix to the inversion term in (2.44), e.g.

$$\boldsymbol{x}_{i+1} = \boldsymbol{x}_i - (\mathbf{J}''(\boldsymbol{x}_i) + \lambda_{i+1}\mathbf{I}_n)^{-1} \tag{2.45}$$

This slightly modified Gauss-Newton iteration is known as the *Levenberg-Marquardt algorithm*. Correspondingly, the factor λ_{i+1} is called the *Levenberg-Marquardt parameter*, or *LM parameter* for short.. The LM parameter is changed with every iteration step, approaching zero as the algorithm converges on the solution (cf. Nocedal and Wright, 1999). Instead of the identity matrix $\mathbf{I}_n$, other matrices may be used, for instance the regularisation matrix $\mathbf{S}_a^{-1}$ itself.

2.3.4. Diagnostics

When the minimisation algorithm has converged on a solution $\boldsymbol{x}_f \in \mathbb{R}^n$, further diagnosis is necessary to estimate how it relates to the true state. The following questions present themselves:

- What is the total uncertainty associated with each component of the state vector?
- How is the actual atmospheric state mapped onto the result? What is the spatial resolution of the retrieved state?
- What influence does the regularisation technique exert on the result?

The discussion here will remain brief and be based on the linear error analysis described e.g. by Rodgers (2000). For practical applications, the direct calculation of the involved quantities can often be prohibitively expensive in the case of large-scale problems; an approach to implement the linear error diagnosis based on Monte Carlo computations was discussed by Ungermann (2013).

Sensitivity to Measurement Noise

The *gain matrix*, defined as

$$\begin{aligned}\mathbf{G} &= \mathbf{J}''(\boldsymbol{x}_f)^{-1}\mathbf{F}'(\boldsymbol{x}_f)\mathbf{S}_\epsilon^{-1} \\ &= \left[\mathbf{S}_a^{-1} + (\mathbf{F}'(\boldsymbol{x}_f))^T\mathbf{S}_\epsilon^{-1}(\mathbf{F}'(\boldsymbol{x}_f))\right]^{-1}(\mathbf{F}')^T\mathbf{S}_\epsilon^{-1}\end{aligned} \tag{2.46}$$

represents the linearisation of the retrieval process around the forward mapped solution $\boldsymbol{F}(\boldsymbol{x}_f)$. Any small disturbance $\delta\boldsymbol{y}$ in the measurements is propagated into the retrieval result as $\delta\boldsymbol{x} = \mathbf{G}\delta\boldsymbol{y}$. The gain matrix therefore characterises the robustness of the retrieval result against measurement errors. In order to illustrate this, consider the special case where the cost function was not regularised. Then the $\mathbf{S}_a^{-1}$ term in $\mathbf{J}''$ vanishes, and the gain matrix $\mathbf{G}$ is just the inverse of the forward model Jacobian:

$$\mathbf{G}_0 = (\mathbf{F}'(\boldsymbol{x}_f))^{-1} \tag{2.47}$$

Note that, for real-world problems, this is strictly formal notation, because the Jacobian $\mathbf{F}'$ is generally not of full rank. The gain matrix rep-

resents a *generalised inverse* or a *pseudo-inverse* of the forward model $\boldsymbol{F}$, linearised around $\boldsymbol{F}(\boldsymbol{x}_f)$.

As a linearisation of the inverse model, the gain matrix can also be used to transform measurement error covariances into retrieval result covariances:

$$\mathbf{S} = \mathbf{G}\mathbf{S}_\epsilon\mathbf{G}^T \tag{2.48}$$

In the special but commonly assumed case of uncorrelated measurement errors, i.e. where $\mathbf{S}_\epsilon$ is diagonal, the main diagonal of $\mathbf{S}$ assumes the form

$$\mathbf{S}_{ii} = \sum_{l=0}^{m-1} \mathbf{G}_{il}^2\sigma_l^2 = \sum_{l=0}^{m-1} \left(\frac{\partial(x_f)_i}{\partial y_l}\right)^2 \sigma_l^2 \tag{2.49}$$

In the second equation of (2.49), the gain matrix was identified with the derivative of the retrieved solution $\boldsymbol{x}_f$ with respect to the measurement $\boldsymbol{y}$. Any diagonal element $\mathbf{S}_{ii}$ itself is the variance associated with the i-th component of $\boldsymbol{x}_f$.

It becomes clear that (2.49) is just the well-known Gaussian error propagation theorem for uncorrelated errors:

$$\Delta f(x_0, \ldots, x_N) = \sqrt{\left(\frac{\partial f}{\partial x_0}\Delta x_0\right)^2 + \cdots + \left(\frac{\partial f}{\partial x_N}\Delta x_N\right)^2} \tag{2.50}$$

The gain matrix $\mathbf{G}$ characterises the inverted model around the retrieved solution $\boldsymbol{x}_f$, i.e. it provides a mapping $\mathbb{R}^m \to \mathbb{R}^n$. It has been shown how this linearised inversion can be used to propagate measurement errors into the retrieved state, thus answering the first question raised in the beginning of this subsection.

Sensitivity to the true state

For a better understanding of the role that the true state and the a priori play for the retrieval result, it is useful to view the retrieval process itself

as a function

$$\boldsymbol{R} : \mathbb{R}^m \times \mathbb{R}^n \to \mathbb{R}^n, \qquad (\boldsymbol{y}, \boldsymbol{x_a}) \mapsto \boldsymbol{R}(\boldsymbol{y}, \boldsymbol{x}_a) = \boldsymbol{x}_f \tag{2.51}$$

By composition of $\boldsymbol{F}$ and $\boldsymbol{R}$, the solution can now be expressed as a function of the unknown true state $\boldsymbol{x}_t$:

$$\boldsymbol{x}_f(\boldsymbol{x}_t) = \boldsymbol{R}(\boldsymbol{F}(\boldsymbol{x}_t) + \epsilon, \boldsymbol{x}_a) \tag{2.52}$$

Linearised around the a priori state $\boldsymbol{x}_a$, this becomes:

$$\begin{aligned} \boldsymbol{x}_f(\boldsymbol{x}_t) &\approx \boldsymbol{R}(\boldsymbol{F}(\boldsymbol{x}_a) + \mathbf{F}'(\boldsymbol{x}_t - \boldsymbol{x}_a) + \epsilon, \boldsymbol{x}_a) \\ &\approx \boldsymbol{R}(\boldsymbol{F}(\boldsymbol{x}_a), \boldsymbol{x}_a) + \mathbf{G}\mathbf{F}'(\boldsymbol{x}_t - \boldsymbol{x}_a) + \mathbf{G}\epsilon \end{aligned} \tag{2.53}$$

Assuming that the retrieval $\boldsymbol{R}$ reliably maps forward calculations of known states back onto themselves, the first term is just the a priori state $\boldsymbol{x}_a$ itself. From this follows the linearised equation

$$\boldsymbol{x}_f = \mathbf{A}\boldsymbol{x}_t + (\mathbf{I}_n - \mathbf{A})\boldsymbol{x}_a + \mathbf{G}\epsilon \tag{2.54}$$

with the *averaging kernel matrix*, defined by

$$\mathbf{A} = \mathbf{G}\mathbf{F}' \in \mathbb{R}^{n \times n} \tag{2.55}$$

The matrix $\mathbf{A}$ determines which parts of the atmospheric state are mapped into a given component of the solution. Consider the case of an atmosphere represented by a single one-dimensional trace gas profile. Then the i-th row of $\mathbf{A}$ is a vector of the weights with which each part of the true profile contributes to the i-th component of the solution. In other words, the row vectors determine the vertical averaging (hence the name) or smoothing caused by the regularisation. If no regularisation was employed, the averaging kernel would assume the form of the identity matrix, i.e. $\mathbf{A} = \mathbf{I}_n$.

Resolution and Information Content

The matrix $\mathbf{A}$ determines the resolution of the result components. The i-th row of $\mathbf{A}$ will assume the shape of a curve peaked around the i-th component; the peak will be narrower with lesser regularisation as the averaging kernel approaches the identity matrix. The *full width at half maximum* or *FWHM* of the row is used as a measure of the spatial resolution of retrieval results. This concept can be generalised to problems of higher dimension.

Equation (2.54) illustrates which sources of information enter the result. The averaging kernel $\mathbf{A}$ determines the contribution from the true atmospheric state. The complementary matrix $(\mathbf{I}_n - \mathbf{A})$, on the other hand, represents the influence of the assumed a priori state. By making use of concepts from information theory (see Shannon, 1948), one can find expressions for the *information content* associated with the measured signal (see Rodgers, 2000, for a derivation):

$$H = -\frac{1}{2}\log(\det(\mathbf{I}_n - \mathbf{A})) \tag{2.56}$$

This quantity is analogous to Gibb's entropy known from the context of thermodynamics. In the context of data processing, the logarithm in (2.56) is often replaced by the dual logarithm $\log_2$. In this case, the value of H is given in "bits".[6] The information content H can be used to evaluate the suitability of specific setups for the trace gas retrieval algorithm. Blank (2014) has developed a spectral window selection algorithm for use in tandem with the JURASSIC2 retrieval processor based on genetic optimisation.

[6] Analogolously, values obtained from the natural logarithm are sometimes assigned the unit "nats".

3. The GLORIA Instrument

The *Gimballed Limb Observer for Radiance Imaging of the Atmosphere* (GLORIA) is an airborne atmospheric sounder developed jointly by the German research centres *Forschungszentrum Jülich GmbH* and *Karlsruher Zentrum für Technologie*. Its main purpose is the examination of trace gas distributions in the upper troposphere and lower stratosphere (UTLS) region, in an altitude range between about 5 and 20 km. This is achieved using a combination of three principal technologies: limb sounding, Fourier spectroscopy, and infrared imaging.

GLORIA was envisioned as a satellite instrument with air- and balloonborne precursor instruments from the beginning (see Riese et al., 2005; Friedl-Vallon et al., 2006). It was then decided to develop the airborne version into a demonstrator for *PREMIER*, a candidate for an ESA Earth Explorer mission (see the report for mission selection by ESA, 2012). The PREMIER mission proposal included an infrared limb imager based on GLORIA, accompanied by a millimetre-wave limb sounder based on the airborne *MARSCHALS* instrument. Out of 26 proposals for Earth Explorer 7, PREMIER achieved Phase-A status among only two other candidates, but was ultimately not selected. However, PREMIER studies in the past have already proven the scientific potential of the instrument concept (see Ungermann et al., 2010a; Preusse et al., 2009), to be further supported by the first measurements of GLORIA presented in this work and by Blank (2014). Future designs based on GLORIA are already in planning, probably excluding the millimetre-wave sounder originally envisioned for PREMIER. Until then, development continues on the original airborne GLORIA as well as an upcoming balloon adaptation.

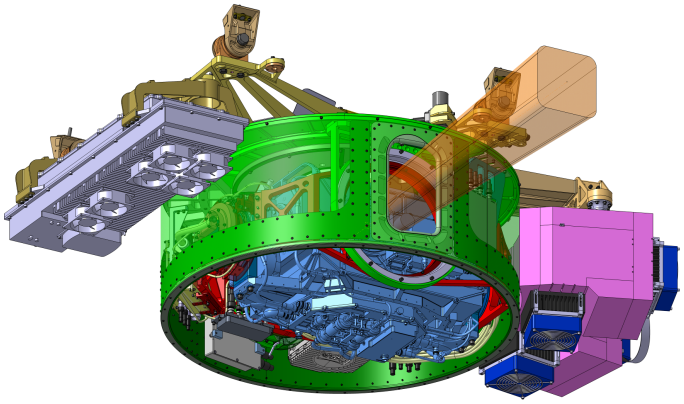

Figure 3.1.: *Schematic of the GLORIA instrument, with colour-coded components. The blue element in the centre is the interferometer unit, and the two pink coloured elements on the right side are the calibration blackbodies. Source: T. Kulessa (Forschungszentrum Jülich GmbH)*

This chapter serves to introduce the terminology and concepts that will be used throughout the technical descriptions to follow, and to clarify how the measurement principle outlined in chapter 2 is implemented by GLORIA.

3.1. Instrument Design

3.1.1. Overview

GLORIA is a complex instrument and consists of a multitude of partially independent devices, each performing a well-defined set of tasks. This modular design is reflective of the instrument's ambitious scientific scope and the number of specialists from various institutes collaborating on it. A (non-exhaustive) list of components includes:

- the *Michelson interferometer* (IFM), which modulates the incoming light (see ch. 2.1),

- the 2D *infrared detector array*, which records the modulated radiances,
- the *length measurement interferometer* (LMI), also referred to as the *laser interferometer*, which measures the optical path difference,
- the *inertial measurement and control unit* (IMCU), which measures and controls the instrument's attitude in space,
- the *gimbal frame*, which holds the instrument in place and executes the IMCU's control instructions,
- the two *calibration blackbodies*, which provide a stable and homogeneous radiation source to help determine the current instrument response function,
- and the *flight computer* (CHEFFE), which serves as the instrument's central control and communications unit.

The following sections will give a brief introduction to some of the GLORIA instrument's most important subsystems, grouped by the tasks they perform. This information will serve as a point of reference for the coming chapters.

3.1.2. In-Flight Control

Most devices within GLORIA have their own data processing and communication system. They are connected to a common network via Internet Protocol (IP) over Ethernet. The flight computer serves as the figurative "brain" of this system. Through the network, it collects status information from all the independently operating components. The computer continuously processes this information in real time and coordinates the components by issuing commands, also over the network, according to a pre-programmed set of rules.

It is also able to send instrument status information, called *housekeeping data*, to an on-board operator (if present), or to the ground control team via satellite. Both the local network and the satellite link are bidirectional, meaning that an operator on the plane or on the ground can issue commands to the flight computer if manual override is necessary. These manual commands are translated and relayed to the appropriate GLORIA components.

For instance, one of the rulesets defines GLORIA's behaviour in dynamics mode. The flight computer will coordinate GPS coordinates and attitude information supplied by the IMCU to calculate the target point. This information is then used by the IMCU to keep the point in the instrument's line of sight as the carrier plane moves. The interferometer notifies the flight computer once the current measurement is completed. On this signal, the computer calculates the next line of sight and has the IMCU rotate the instrument appropriately. After a set number of measurements, another programme (e.g. calibration mode) may be executed. If at any time an unforeseen problem occurs, the computer can be manually instructed to halt the current programme and switch into manual mode. For example, the encoders for the gimbal frame's angular position might be decalibrated due to mechanical shock, an incident that occured once during the TACTS campaign. In such an event, the on-board operator or the ground control team can then diagnose the error, recalibrate or restart the affected device, and recommence the measurement programme.

Another example for the value of this system is the *GloriaWatch*[1] application, an on-line tracking system for GLORIA first conceived during the ESSenCe measurement campaign, and later extended for use during TACTS/ESMVal. The GLORIA housekeeping protocol was partially reimplemented in a Python module. For GloriaWatch, it is used to request and receive general GLORIA status as well as the GPS and attitude information. These data packages are preprocessed and then sent

[1] developed by J. Blank and T. Guggenmoser

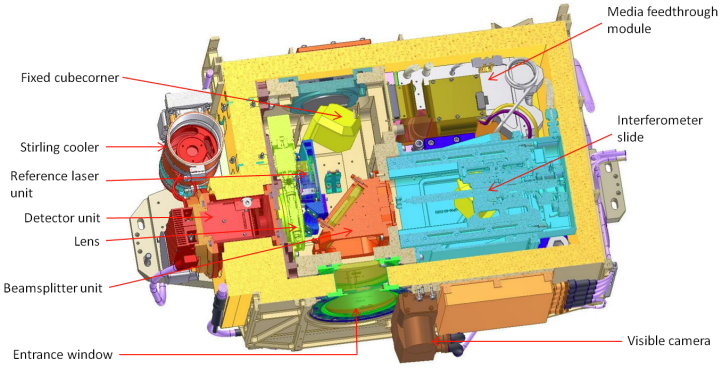

Figure 3.2.: *The GLORIA Michelson interferometer unit (IFM). The apparatus is shown here in a horizontal cross-section so that the individual elements are recognisable. Source: C. Sartorius (Karlsruher Institut für Technologie).*

to the GloriaWatch server, which is based on the Google Maps™ framework. The server provides a website, accessible from all over the world, which plots GLORIA's current position on a map, with some additional information about GLORIA's status. The same Python module was also used to create the *GLORIA Operator Tool*, which is a reduced version of the tracking system that does not require internet access, specifically tailored to be used by the GLORIA operator on board the aircraft.

Detailed information on the GLORIA control system is given in Kretschmer et al. (2014). The housekeeping and measurement data that are important for the data processing will be explained further in section 3.2.

3.1.3. Interferometer

The GLORIA interferometer (IFM) is an implementation of the measurement principle discussed in section 2.1. GLORIA's interferometer has been designed to generate two-sided interferograms with a maximum optical path difference of 8 cm. This is the OPD configuration for chem-

istry mode operations and results in a spectral sampling of $0.0625\,\mathrm{cm}^{-1}$. In dynamics mode, the IFM is configured for an optical path difference of 0.8 cm to match the dynamics mode spectral sampling requirement of $0.625\,\mathrm{cm}^{-1}$. In practice, the optical path difference is slightly larger to accomodate a safety margin and to ensure that the Level-0 processing (see 4.1) can be performed correctly for all pixels, regardless of their position relative to the optical axis. The IFM's slide velocity, i.e. the velocity at which the optical path difference is varied, is configurable. During the ESSenCe and TACTS/ESMVal campaigns, the IFM run at an optical velocity $v = 1.28\,\mathrm{cm/s}$. For two-sided measurements, this corresponds to a pure acquisition time of about 12.5 s (chemistry mode) or 1.25 s (dynamics mode), not including non-measuring periods during which the slide de- and accelerates.

The modulated light is imaged onto an infrared focal plane array custom-built by *AIM Infrarot-Module GmbH*. This 2-dimensional infrared detector is sensitive in a wavenumber range between approximately $750\,\mathrm{cm}^{-1}$ ($6.9\,\mu\mathrm{m}$) and $1450\,\mathrm{cm}^{-1}$ ($13.3\,\mu\mathrm{m}$). It can be configured to record image frames with up to 256x256[2] pixels, of which a subsection of 48x128 pixels was used during the previous two measurement campaigns. Using this subsection, a framerate of 6128 Hz was achieved. A high framerate allows for faster optical slide velocities with the same interferogram sampling. This reduces the relative effect of velocity variations on the accuracy of the Level-0 resampling algorithm and is therefore preferable in a high-vibration environment such as an aircraft. Moreover, the measurements take less time with the same spectral resolution and therefore provide a higher measurement density, leading to a better spatial resolution of the observed atmosphere.

In addition to the main infrared interferometer, a comodulated length measurement interferometer (LMI) using a visible-range laser source is installed in the device. Its signal is used as a reference for the interpolation of the time-sampled detector signal onto a spatial axis.

[2]The instrument's field of view is limited to 128x128 pixels.

3.1.4. Calibration Blackbodies

Instruments deployed in a liquid helium (LHe, 4 K) cryostat, such as CRISTA, show very little emission of the instrument's internal components. The GLORIA interferometer unit, on the other hand, is cooled prior to the measurement flight using liquid nitrogen (LN_2, 77 K) to a target temperature of about 200 K. During the flight, it is thermally stabilised using dry ice (CO_2, 194 K). Due to the resulting temperature drift, components within the spectrometer exhibit a continuously varying emission behaviour. These emissions partially enter the optical path and are measured by the detector. Because of this, the *instrument background* or *radiometric offset* changes with time. This is also true, although to a lesser extent, for the *radiometric gain*, i.e. the instrument's linearised response to incoming radiation.

GLORIA is equipped with two reference blackbodies which are used for the instrument's radiometric calibration. They have been developed by the atmospheric physics group at *Bergische Universität Wuppertal* and are designed to provide a homogeneous and almost perfectly Planckian infrared source with an emissivity close to 1 in the relevant spectral range (Olschewski et al., 2013).

The blackbodies are realized as rectangular cuboid cavities with an interior consisting of pyramids. Peltier elements in the back of the cavity are used to control the emitted brightness temperature. Several temperature sensors at the bases and in the middle of the pyramid surfaces are installed to monitor the homogeneity and current temperature of the blackbodies. The sensors have been calibrated by the *Physikalisch-Technische Bundesanstalt*, the German national metrological institute, using radiative measurements. This ensures that the measured values correspond to actual brightness temperatures, as opposed to surface temperatures. For more details about the temperature calibration, see Monte et al. (2013).

During flight, the spectrometer is periodically pointed to these sources and measurements are taken of the emitted infrared light. Using the sep-

arately recorded blackbody temperatures, the blackbody radiance can be modelled using Planck's function. Assuming a linear instrument response, the radiometric gain and offset of the instrument at the time of calibration can then be retrieved. This can be achieved either using both blackbodies stabilised at two distinct temperature levels or by using one of the blackbodies in conjunction with a so-called *deep-space measurement*. These techniques are further explained in chapter 4.2.1.

3.2. Measurement and Housekeeping Data

GLORIA records a variety of data which can be divided into two categories: the atmospheric measurement data and the stream of housekeeping data. The latter contains metainformation from the instrument's components, e.g. temperatures and voltages, and is important for instrument operation and diagnostics. Also part of the housekeeping stream are GPS geolocation and instrument attitude, both of which are crucial for the later data processing. This whole stream is recorded by the flight computer, mounted either in the fuselage together with GLORIA or in the passengers' cabin.[3] The flight computer dumps these data to disk and also redistributes part of the stream via network to the mission control centre via satellite phone. After a flight, the housekeeping data are fed into a relational database for permanent storage and more convenient use.

The actual measurement data consist of two files per record. Each record is identified by its initial UTC timestamp, e.g. "20120926_110000" for a measurement taken on 26 September 2012 and starting at exactly 11:00 UTC. The two files written to disk are the *cuboid file* (CUB), which contains the raw interferogram data, and the *laser axis file* (LXA), containing timestamps from the LMI. The number of frames in the CUB

[3]The former is the case for deployments on the M55 Geophysica aircraft, whose pressurised cabin is only designed to house the pilot. HALO, on the other hand, features a full passenger cabin with racks to mount computing equipment.

Figure 3.3.: *The Myasishchev M55 Geophysica high altitude aircraft deployed during the ESSenCe measurement campaign in 2011. The aircraft is shown being towed back from the runway towards the Arena Arctica hangar at Kiruna Airport, Sweden. The GLORIA instrument is visible behind the opening in the fuselage right below the cockpit.*

corresponds to the length of the measurement, i.e. ultimately the MOPD of the measurement mode. As the measurements are taken at a sampling frequency of 6128 Hz, a typical dynamics mode measurement would contain around 8,000 frames, while a chemistry mode CUB is an order of magnitude larger at around 80,000 frames.

3.3. Measurement Campaigns

3.3.1. ESSenCe

GLORIA's first campaign was the *ESA Sounder Campaign* (ESSenCe), performed during November and December of 2011. As the name suggests, the campaign was co-funded by the European Space Agency (ESA). At that time, GLORIA served as a demonstrator for PREMIER-IRLS, the infrared component of the PREMIER mission candidate for the Earth Explorer 7 satellite mission (see ESA, 2012). Consequently, the campaign's primary goal was to test GLORIA in conjunction with the MARSCHALS[4] instrument, which served as a demonstrator for STEAMR, PREMIER's microwave component.

Initially, the campaign was planned for a late summer of 2011 in a subtropical setting, to be based on Sicily. However, the campaign coincided with the Lybian Civil War, and the resulting airport and airspace restrictions made this impossible. Finally, it was decided that the campaign would take place during winter and based in the *Arena Arctica* at Kiruna Airport, Sweden. The Arena Arctica had previously served as the base of operations for several other measurement campaings, e.g. RECONCILE in 2010/2011 (von Hobe et al., 2013).

The carrier used for ESSenCE was the M55 Geophysica high-altitude aircraft (see fig. 3.3), built and operated by Myasishchev Design Bureau[5] (MDB). The plane is based on a Soviet reconnaissance aircraft and balloon interceptor design and produced during the 1980s. It now serves as a carrier aircraft for scientific instruments, featuring an exceptionally high service ceiling of up to 21.0 km which makes it ideal for research in the UTLS region. Figure 3.4 shows the GLORIA instrument deployed on the M55 during the ESSenCe campaign.

[4] *Millimetre-Wave Airborne Receivers for Spectroscopic Characterisation in Atmospheric Limb Sounding*

[5] Russian: *Экспериментальный машиностроительный завод им. В.М.Мясищева*

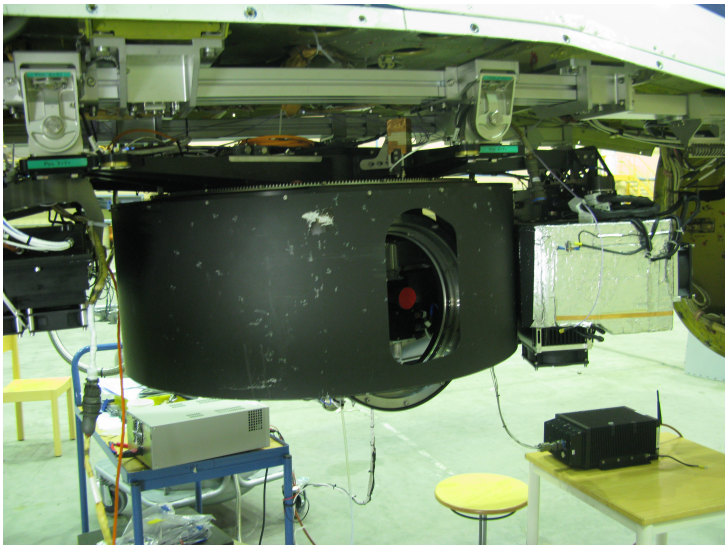

Figure 3.4.: *GLORIA installed inside the M55 Geophysica*

ESSenCe was GLORIA's first deployment and mainly served as a technical campaign with a focus on instrument performance analysis. The atmospheric data set which could be successfully processed therefore remained limited to a short period during one of the two flights. Results and performance evaluations have so far been presented by Kaufmann et al. (2013) and Blank (2014).

3.3.2. TACTS/ESMVal

TACTS and ESMVal were two measurement campaigns conducted during August and September 2012. Both campaigns made use of the newly introduced HALO aircraft (see fig. 3.5) operated by *Deutsches Zentrum für Luft- und Raumfahrt* (DLR), the German national space agency. They were separately funded and differed in their scientific focus, but they were performed in the same timeframe using the same instrumen-

Figure 3.5.: *The HALO aircraft, based on the Gulfstream G550 series business jet, was the platform used for the TACTS/ESMVal campaign. The aircraft is operated by DLR and can carry a multitude of instruments, including computing equipment and operating personnel. This figure shows HALO on in front of the DLR flight operations hangar in Oberpfaffenhofen, Germany.*

tation. For the rest of this work, they will therefore mostly be referred to as "the TACTS/ESMVal campaign".

TACTS stands for *Transport and Composition in the UT/LMS*.[6] Its main goal was to provide a data set for quantitative assessment of *stratosphere-troposphere exchange* (STE), especially across the so-called *extratropical tropopause transition layer* or ExTL (Fischer et al., 2000). Consequently, measurement flights were made for this campaign mainly between Central Europe, the Mediterranean, West Africa and the Atlantic Ocean.

ESMVal stands for *Earth System Model Validation*. This campaign's main focus was on data acquisition for the validation of large-scale

[6] UT/LMS stands for *upper troposphere and lowermost stratosphere*, a subset of the UT/LS region.

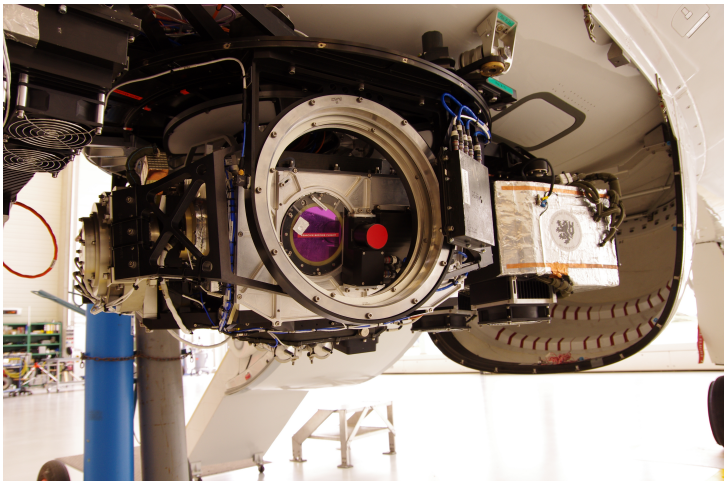

Figure 3.6.: *The GLORIA instrument mounted in the HALO aircraft's bellypod*

chemistry-climate models (CCMs). Therefore, a principal aim was to obtain a very diversified data set from a wide range of latitudes. This was achieved as flights were performed as far as Spitsbergen (80° N) and the northernmost parts of the Antarctic winter ice sheet (65° S).

The base of operations, and the primary mission control centre for GLORIA, was the flight operations hangar located at the DLR facilities in Oberpfaffenhofen, Germany. Auxiliary bases were installed at airports in Sal (Cape Verde), Cape Town (South Africa), Malé (the Maledives) and Larnaca (Cyprus).

During the two campaigns, a total of twenty flights were conducted. Of these, twelve had a scientific (rather than technical) focus. GLORIA successfully recorded atmospheric spectra on all of these flights with the exception of Flight 17, where a technical malfunction forced extensive maintenance at the main base in Oberpfaffenhofen. For a visual overview of the measurement flights and the wide spatial coverage achieved with GLORIA observations, see figure 3.7.

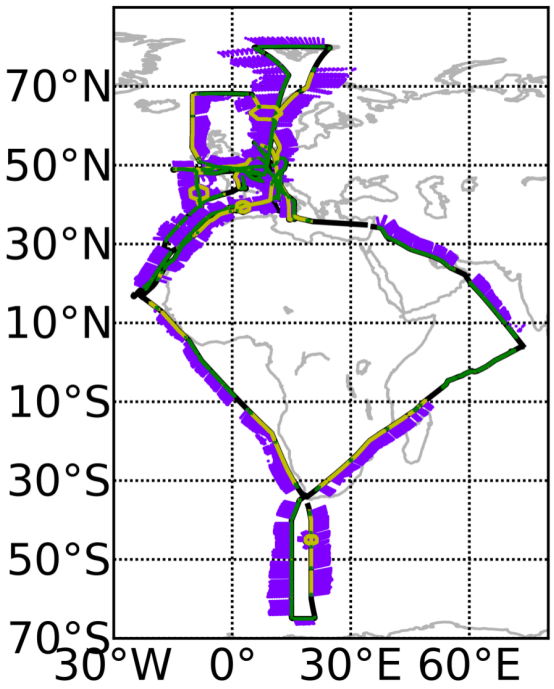

Figure 3.7.: *Overview of flights performed during the TACTS/ESMVal campaign, together with GLORIA tangent points. Figure courtesy Dr. Jörn Ungermann.*

Figure 3.6 shows the GLORIA instrument deployed within the HALO aircraft's bellypod, an extension to the stock Gulfstream G550 design specifically constructed to house remote sensing instruments.

4. Data Processing Chain

In chapter 3.2, the GLORIA instrument's data acquisition was described which is the point of origin for the data processing chain. This chain can be roughly divided into three principal stages:

Level-0 Resampling from the time domain into the spatial domain. Also correction of off-axis effects and linear phase correction.

Level-1 Transformation into spectral domain, radiometric calibration.

Level-2 Inversion of radiative transfer, retrieval of trace gas volume mixing ratios.

The present chapter will introduce these processing stages, with emphasis on Level-0 and Level-1, which have been extended and partially redesigned for this work. In addition, some auxiliary methods for quick data quality assessment and hardware diagnosis are presented.

4.1. Level-0 Processing

4.1.1. Motivation

The raw GLORIA measurements or cuboids (see 3.2) are sampled at a constant frequency in the time domain. Interferograms, however, are by their nature spatial structures: the recorded signal is modulated with the varying optical path difference (see 2.1). For further processing into a spectrum dependent on the wavenumber ν, a transfer into the spatial domain is necessary.

This does not pose a problem in the simple example discussed in 2.1 because there it was assumed that the optical path is varied in a perfectly uniform way, i.e. that the sliding mirror moves at a constant rate. In a real-life instrument such as GLORIA, this assumption does not hold – the optical path velocity varies considerably within each measurement. The obvious alternative would be to directly sample the interferograms in the spatial domain. This can be achieved e.g. by installing a laser interferometer which is modulated synchronously. The AC component of the interferogram for this monochromatic light source is just the single cosine function from (2.4):

$$\mathrm{AC}_\lambda(\Delta s) \propto \cos\left(2\pi\frac{\Delta s}{\lambda}\right) \tag{4.1}$$

The cosine function vanishes at $\pi/2$ and odd multiples thereof. Therefore, for each progression of the optical path difference by one wavelength, two zero-crossings are detected by the interferometer. The zero-crossing events can then be used to trigger the main detector to record its signal, resulting in a spatially equidistant axis for the interferogram. However, this approach is technically impractical for a high-speed data acquisition system.

A variant of this technique has been first proposed by Brault (1996). In this setup, a laser interferometer is installed as explained above. However, the signal is not used as a trigger for the interferometer, but is recorded separately. The main detector meanwhile samples the interferogram in the time domain at a constant framerate. Using a clock-driven acquisition system, this can be done fast and very precisely. The laser signal is used after the measurement is complete to provide the spatial information for the interferogram.

GLORIA's implementation of the laser interferometer (LMI) records only rising-flank zero-crossings, i.e. each timestamp in the LMI output corresponds to one laser wavelength. Using a method known as *Brault interpolation* or, more generally, *Whittaker-Shannon interpolation*, this

spatial reference axis can now be used to resample the main interferometer's output onto a pre-defined spatially equidistant abscissa. This is the main purpose of the *Level-0 processor* described in this section.

The original Level-0 processor for GLORIA was developed in the form of an IDL prototype by A. Kleinert (KIT). Later on, a fast C-based processor was developed by R. Ribalda and T. Neubert (FZJ) with a limited feature set. For this work, this C code was heavily extended and integrated into the new *gloripy* processing framework developed for this work. Additional performance improvements could also be made by reimplementing the most time-consuming algorithms in a vectorised form.

4.1.2. Description

Cuboid Data Preprocessing

Before the Level-0 processor can perform its core task, the resampling of the measurement data from the cuboid files onto a spatial grid, some preparatory work is necessary.

The first step to be performed is a transposition of the entire cuboid. GLORIA measurement data are recorded in the form of frames, with each frame containing one value for each pixel, just like an ordinary camera might. However, the resampling has to be performed on a per-pixel basis, and this can only be done efficiently when the interferogram samples of each pixel are contiguous in memory. Therefore, the first processing step of the Level-0 processor is the transposition of the cuboid input data.

Resampling

The main step the Level-0 processor has to perform is the resampling itself. The target spatial abscissa $\boldsymbol{x}$ is pre-defined by supplying the starting point x_0, the number of points N_x and the spatial sampling Δx to the Level-0 processor. The relationship between the timestamps and

the spatial points comes from the laser timestamps, with each timestamp signifying that the interferometer has progressed by an optical path difference of one laser wavelength. After accounting for a time delay between the laser timestamps $\tilde{\boldsymbol{u}}$ and cuboid timestamps $\boldsymbol{t}$, the former are interpolated linearly onto the desired spatial abscissa points x_i:

$$u_i = \tilde{u}_j + (x_i - j\lambda)\frac{\tilde{u}_{j+1} - \tilde{u}_j}{\lambda} \tag{4.2}$$

where $\tilde{u}_j$ is the laser timestamp with associated location $j\lambda$ closest to x_i. This new time axis $\boldsymbol{u}$ now contains the times at which the interferometer has reached the locations in $\boldsymbol{x}$. It is not equidistant like the cuboid time axis $\boldsymbol{t}$ but serves as a proxy for the spatially equidistant target axis $\boldsymbol{x}$, by giving the points in time corresponding to it. It will be used to translate between the time-sampled cuboid and the spatial interferogram that is the desired result.

The spatial resampling is accomplished by interpolating the interferogram samples from the cuboid onto the proxy axis $\boldsymbol{u}$ by way of a *Whittaker-Shannon interpolation* (Shannon, 1949). In the context of Fourier spectrometry, this procedure has originally been proposed and described by Brault (1996), who formulated it in the language of electronic filters. For this reason, it is sometimes also referred to as *Brault interpolation* or *Brault convolution*.

Let $\boldsymbol{y} \in \mathbb{R}^N$ be the original interferogram samples for one pixel with equidistant detector timestamps $t_n = n\Delta t$. Then the resampled values $\tilde{\boldsymbol{y}} \in \mathbb{R}^{N_x}$ can be found via the *Whittaker-Shannon formula*

$$\tilde{y}_m = \sum_{n=-\infty}^{+\infty} y_n \operatorname{sinc}\left(\frac{u_m - n\Delta t}{\Delta t}\right) \tag{4.3}$$

This assumes that the y_n are periodically extended for the summation. In the actual Level-0 processor, the interpolation must be approximated by summing only over a finite number K of values. Additionally, cal-

culating the cardinal sine function during runtime would be very computationally expensive. For an efficient application, these values should therefore be pre-tabulated. However, in order to achieve this, the interpolation (4.3) has to be slightly reformulated.

Suppose that, before the calculation itself, for each point u_m the original timestamp t_k nearest to the resampling point u_m is known. The resampling can then be rewritten as[1]

$$\tilde{y}_m = \sum_n y_n \operatorname{sinc}\left(k - n + \frac{u_m - t_k}{\Delta t}\right) \tag{4.4}$$

Here, the relation $t_k = k\Delta t$ was used. To simplify the expressions, the parameter $\xi_m = (u_m - t_k)/\Delta t$ shall be introduced. ξ_m is the difference between the resampling point and the nearest data timestamp, normalised by the original time sampling. Note that, because k is dependent on m, the label ξ_m is sufficient to denote it. The point t_k can now be used as the centre of the desired *finite* summation over K elements. Introducing a corresponding new summation index l with $l = n - k$, this new sum becomes

$$\tilde{y}_m = \sum_{l=-K/2}^{K/2-1} y_{k+l} \operatorname{sinc}(l - \xi_m) \tag{4.5}$$

Because t_k is by definition the *nearest* timestamp to the point u_m, the difference between t_k and u_m can never exceed half the sampling width Δt. Otherwise, another point $t_{k\pm1} = t_k \pm \Delta t$ would be closer to u_m. Due to this, the normalised time distance ξ_m can only assume a limited

[1] It should be noted that limiting the summation to a finite number of terms introduces a "ringing" effect in the resampled signal, similar to the effects of a finite interferogram length on the instrument line shape described in section 2.1.2. To counter this effect, the pretabulated sinc-values are modified with a *Kaiser* window function in practice.

range of values:

$$|\xi_m| = \frac{|u_m - t_k|}{\Delta t} \leq \frac{1}{2} \tag{4.6}$$

This restriction enables the desired lookup table approach mentioned above. The interval $[-\frac{1}{2}, +\frac{1}{2})$ of possible ξ-values can be sampled with an arbitrary precision, independent of any particular $\boldsymbol{t}$ and $\boldsymbol{u}$ axes. For each of these N_ξ values, the associated K values for the cardinal sine function in (4.5) can stored in a table of the form

$$\psi_{jl} = \operatorname{sinc}\left(l - \left(\frac{j}{N_\xi} - \frac{1}{2}\right)\right) \tag{4.7}$$

During the processing, these values can be looked up by matching the parameter ξ_m for the current point u_m with the closest tabulated value, i.e. $j_m = N_\xi(\xi + 1/2)$. In the end, the summation assumes the form

$$\tilde{y}_m = \sum_{l=-K/2}^{K/2-1} y_{k(m)+l} \cdot \psi_{j(m),l} \tag{4.8}$$

To summarise the procedure, first the laser timestamps are interpolated onto the new spatial abscissa points x_m, yielding the resampling points u_m. For each of these points, the nearest time sample $t_k = t_{k(m)}$ is found. The remaining difference between u_m and t_k, normalised by the time sampling Δt, yields the parameter ξ_m. This value is used to select a convolution kernel with the appropriate factors from a precomputed lookup table. The resampling is then performed according to (4.8).

Off-Axis Correction

The procedure outlined above is, stricly speaking, only valid for a pixel that lies exactly in the path of the instrument's optical axis. In general, a correction has to be applied which takes the angle between each pixel and the optical axis into account. If this correction is omitted, the

individual pixels cannot be processed together – it is therefore essential for an imaging FTS such as GLORIA.

Let $\boldsymbol{p_o} = (h_0, v_0)$ be the point on the detector at which it is penetrated by the optical axis, represented by its horizontal and vertical coordinates on the detector surface. Any given pixel with centre coordinates $\boldsymbol{p} = (h, v)$ is then removed from this point at the distance $d = \sqrt{(h - h_0)^2 + (v - v_0)^2}$.

The detector lies within the focal plane of an optical system which projects the interferometric image onto the array. Let f be the focal length. Then the angle α for each pixel can be calculated by using simple trigonometry:

$$\alpha = \arcsin\left(\frac{d}{f}\right) \tag{4.9}$$

This off-axis angle results in an effective stretching of the optical path difference. To normalise this influence among the pixels, a correction factor is applied to the proxy axis $\boldsymbol{u}$ before the resampling itself is performed:

$$\boldsymbol{u} \mapsto [\cos(\alpha)]^{-1}\,\boldsymbol{u} = \left[1 - \left(\frac{d}{f}\right)^2\right]^{-1/2} \boldsymbol{u} \tag{4.10}$$

The correction factors are pretabulated on a per-pixel basis. They are obtained by first determining the focal length f and the optical axis position $\boldsymbol{p_o}$. This is done during the *spectral calibration*, a procedure that is applied to preliminary, non-corrected spectra. Failure to correct for the off-axis effect results in a shift of the spectral lines. Well-known lines for carbon dioxyde (CO_2) are used as references to detect this shift and the off-axis correction parameters are then obtained from a fit to a mathematical model. Another parameter that results from the spectral calibration is the laser wavelength, which is essential for the Brault resampling to yield accurate results. Details about this procedure can be found in Kleinert et al. (2014).

Nonlinearity Correction

Nonlinearities in the detector response can lead to artifacts in the processed spectra (see Kleinert, 2006; Kleinert et al., 2007). As an optional step, the Level-0 processor can substitute the interferogram values with those read from a nonlinearity correction table. These values are the result of a 4-th order polynomial fit of detector characterisation measurements performed under laboratory conditions. A simple substitution is possible because the resampled interferograms are integers and the whole range of values can be tabulated. For more information about how the polynomial values are obtained, see Kleinert et al. (2014).

4.1.3. Implementation and Performance

GLORIA's imaging capabilities result in a particularly high data acquisition rate. Using the 48x128 pixel configuration and a frame rate of 6128 Hz, a total data rate of more than 70 MiBs/s is achieved. In order to process the high resulting data volumes in a reasonable time, the Level-0 processor was developed with a target of real-time performance in mind, meaning that the processing should not take longer than the measurement. This is especially motivated by the prospect of autonomous long-range balloon measurements. In this scenario, onboard data reduction, e.g. by pixel coaddition, may be necessary because storage on the platform is limited. This can only be done when the interferograms are already resampled on a common spatial abscissa, i.e. after the Level-0 processing is finished.

Several core design decisions reflect this early focus on optimisation. One of these is the lookup table approach to the Brault convolution algorithm already described in section 4.1.2. This prevents the need for expensive runtime computations of the cardinal sine function.

Another aspect is the decision to use integer instead of floating-point arithmetic for the convolution. The tabulated values have been rescaled and truncated to signed 16-bit integers. While the performance of

floating-point arithmetic is not necessarily worse than that of integer calculations on modern computers, the 16-bit representation allows for an overall smaller table which is able to fit in the CPU cache. This makes lookups extremely efficient as no intermediate memory access is required.

The runtime of the Level-0 processor is dominated by two tasks: the cuboid transposition and the actual resampling itself. Fortunately, both of these processes lend themselves nicely to shared-memory parallelisation, which is implemented in the Level-0 processor using the OpenMP library.

For this work, additional improvements have been made to the code. Among these are the reimplementation of the cuboid transposition and Brault resampling algorithms in low-level machine operations that exploit the vector-processing capabilities of modern CPUs, known as the SSE instruction set. These new implementations have resulted in substantial performance gains that put the Level-0 processor well beyond the real-time requirement. For details about these implementations, see appendix A.

Runtime measurements have been peformed (see Kleinert et al., 2014, with a contributed section) using a single GLORIA chemistry mode measurement. The cuboid file in question was about 945 MiB (990,173,696 Bytes) in size and took 12.9 seconds to record. The CPU used for the benchmark was an AMD Opteron 6128, an 8-core processor with a clock speed of 1800 MHz. To eliminate the impact of hard disk performance, file I/O has been performed on a RAM-based file system.

Figure 4.1 shows the total Level-0 processing time, and the specific runtime of the cuboid transposition and Brault convolution steps. With vectorisation deactivated, a single-thread (non-parallelised) process takes 56.4 seconds to run. Enabling all 8 CPU cores reduces this time to 12.4 seconds. This already matches the real-time performance goal. With the SSE vectorisation enabled, the runtimes reduce further to 36.9 seconds and 9.5 seconds, respectively.

In figure 4.2, the speedup factor is shown with increasing parallelisa-

tion. Here, the Brault convolution benefits the most, its performance scaling almost linearly with the number of parallel threads. The cuboid transposition does not scale equally well; this is due to a more extensive non-parallelisable overhead in the code as well as the limited memory bandwidth. The total speedup of using 8 cores and SSE vectorisation, compared with single-threaded non-vectorised mode, is 17 for the transposition, 9.5 for the convolution and 6 for the Level-0 processor as a whole.

From the vectorisation, the Brault convolution gains a speedup of about 25%, almost independently of the number of threads. The cuboid transposition is sped up immensely, by 400% in single-threaded and still over 300% in 8-core mode.

The resulting Level-0 processor is a high-performance programme that can process GLORIA measurements faster than the data acquisition rate on a reasonably powerful computer. Even without the on-board processing requirement of balloon flights, the Level-0 processor's performance is important for the processing chain as a whole, and indirectly for the scientific exploitation of GLORIA campaigns. Previously a standalone programme, the Level-0 processor has been heavily modified as part of the processing chain reimplementation presented in this work. The extensions involve making the processor's data structures and routines accessible from other parts of *gloripy*, allowing the C-based Level-0 processor to interoperate seamlessly with the Level-1 processing components.

A unified Level-0 and Level-1 environment is an essential development for the operational linear phase correction described in section 4.4.5. Diagnostics and auxiliary processes, e.g. the raw data pre-analysis tools presented in chapter 4.5, also benefit significantly. These programmes are now able to leverage the highly optimised cuboid reading and transposition routines of the Level-0 processor, reducing days of runtime to a few hours.

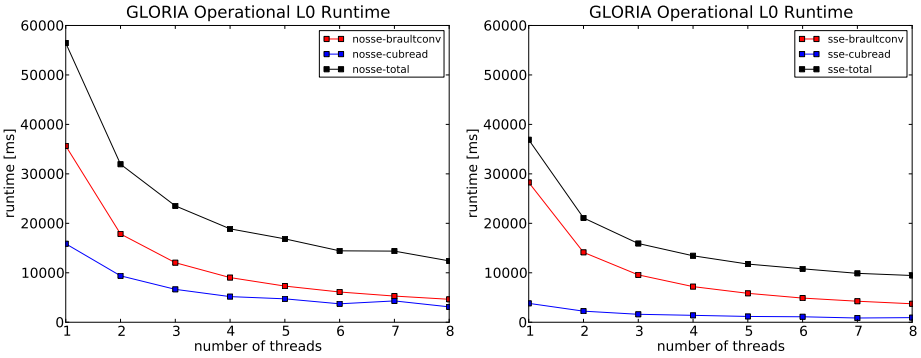

(a) without SSE *(b) with SSE*

Figure 4.1.: *Total runtimes and runtimes for the two most critical calculations with increasing level of OpenMP parallelisation, with and without the use of SSE vectorisation.*

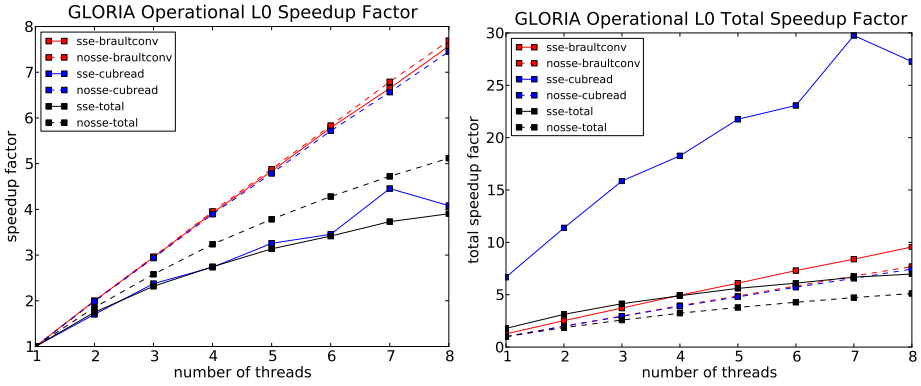

(a) *(b)*

Figure 4.2.: *Speedup factors for the Level-0 processor with increasing parallelisation. Figure a) shows the scaling factor of the vectorised and non-vectorised algorithms. Figure b) is normalised to the non-vectorised version, i.e. the speedup includes the effects of both vectorisation and parallelisation.*

4.2. Level-1 Processing

4.2.1. Overview

The Level-0 processing stage produces spatially sampled interferograms. While the values of the interferogram samples are a measure of the radiance measured by the detector at their respective OPD positions, they are not given in physically meaningful units.

It is the task of the Level-1 stage to retrieve from these interferograms the spectral radiance on a wavenumber-equidistant axis. The transfer of the data from the spatial into the spectral domain is achieved by way of a Fourier transform (see section 2.1). From these *uncalibrated spectra*, still in non-physical units, physically meaningful radiance values are obtained by applying the inverse of the *instrument response function*. This step is simple to perform in itself. However, finding the instrument response function can be a challenging task.

Due to the GLORIA spectrometer's components exhibiting a continuous thermal drift, the function changes over time, albeit slowly. Frequent calibration measurements using the on-board blackbodies are performed to provide the necessary reference points. This chapter introduces the principles of radiometric calibration, as well as some GLORIA-specific techniques developed for the processing of the TACTS/ESMVal data sets with *gloripy*.

4.2.2. Radiometric Calibration Basics

After resampling (see section 4.1), the measured interferograms are still in non-physical units, in the form of unsigned 16-bit integers limited by the range of the detector's 14-bit AD-converter. After Fourier transform, these values have been converted to 128-bit complex numbers. Via the process of *radiometric calibration*, the values are converted into absolute spectral radiances.

The detector response is not the only factor determining the total instrument response. Thermal infrared emissions and absorbtions by the

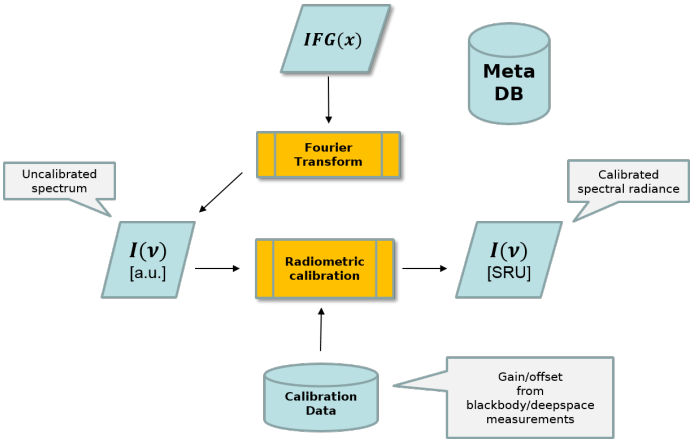

Figure 4.3.: *The basic steps of Level-1 processing. The result of the Level-0 algorithm discussed in section 4.1 is first Fourier transformed. Once in the spectral domain, the measurements are radiometrically calibrated using linear calibration coefficients obtained from reference blackbody and deep space measurements.*

instrument's components partially fall within the detector's sensitivity range. This leads to both a *radiometric offset* due to the instrument background radiation and a change in the response rate, the *radiometric gain*.

Instrument effects affect the spectrum at different phase angles (see section 2.1.5), which has to be accounted for at this stage. The most straightforward way of doing this is to perform the calibration entirely within the complex domain, an approach originally popularised by Revercomb et al. (1988). After complex calibration, the real part ideally contains only the atmospheric signal, while the imaginary part contains only noise. One criterion for the success of the calibration process is therefore the degree to which atmospheric signal is still present in the imaginary part of the output spectrum. This calibration scheme will be followed in this work.

The GLORIA instrument is assumed to exhibit a *linear response* to

the measured spectral radiances. That is, for each detector pixel (column i, row j) and each Fourier-sampled wavenumber ν, the uncalibrated values will be

$$y^{i,j}(\nu) = a^{i,j}(\nu)I^{i,j}(\nu) + b^{i,j}(\nu) \tag{4.11}$$

where $a^{i,j}(\nu)$ and $b^{i,j}(\nu)$ are the complex gain and offset parameters, $y^{i,j}(\nu)$ is the uncalibrated measurement, and $I^{i,j}(\nu)$ is the actually observed spectral radiance. In order to derive this linear instrument response function, at least two reference points are needed for each pixel and wavenumber. GLORIA is designed to provide three reference points. Two on-board Peltier-stabilised blackbody sources are installed in the instrument, serving as homogeneous sources of Planck radiation at a known temperature (see section 3.1.4). In addition, GLORIA's attitude control system and gimbal frame allow it to be pointed upwards at a pitch of 10°. These *deep space measurements* provide a third point of reference with very low atmospheric signal and therefore very close to the radiometric offset.

The GLORIA calibration blackbodies can be expected to emit radiation according to Planck's law:

$$y^{i,j}_{BB}(\nu) = a^{i,j}(\nu)B(T_{BB}, \nu) + b^{i,j}(\nu) \tag{4.12}$$

where T_{BB} is the blackbody temperature and $B(T, \nu)$ is the Planck function. The blackbody temperature sensors themselves have been calibrated pre-flight by the *Physikalisch-Technische Bundesanstalt*, the German national metrology institute, via radiometric reference measurements, guaranteeing that the temperatures used are actual brightness temperatures that characterise the blackbody's emission (Monte et al., 2013).

For the so-called "deep space" (DS) measurements, the instrument was pointed at an elevation of 10°. These measurements are performed periodically, in close proximity to the blackbody measurements, so that the same instrument background can be assumed. The purpose of deep

space measurements is to measure this instrument background, which is just $b^{i,j}(\nu)$, the radiometric offset.

Such offset measurements are a common technique for satellite and balloon instruments. For instruments operating at the much lower airplane altitudes, the information they contain is not as unambiguous. Even high-altitude research aircraft like the M55 Geophysica and HALO carriers can only fly at altitudes around 20 or 15 km, respectively, corresponding to pressure levels of 55 and 120 hPa as opposed to the maximum of about 40 km (3 hPa) at which earth observation balloons can operate. Consequently, the trace gas volume mixing ratios at and above flight level are much higher, resulting in comparatively high residual emission in the deep space spectra, especially from ozone.

For the purposes of data processing, it is best to consider, instead of eq. (4.11), the inverse mapping

$$I^{i,j}e(\nu) = \alpha^{i,j}(\nu)y^{i,j}(\nu) + \beta^{i,j}(\nu) \tag{4.13}$$

where $\alpha = a^{-1}$ is the "inverse gain" (IG) and $\beta = -a^{-1}b$ is the "negative calibrated offset" (NCO). These are the quantities that are actually used in the processing software. Another advantage of using the IG and NCO is that the NCO corresponds to an actual physical quantity that is readily interpreted as the radiometric instrument background.

Due to the detrimental effect of calibration noise on the recorded 2D image, the calibration data need to be smoothed before they can be used to generate calibrated spectra. Calibration data are therefore generated with a reduced interferogram length resulting in a spectral sampling of $5\,\mathrm{cm}^{-1}$, i.e. an implicit lowpass filter is applied to reduce noise. In addition, smoothing based on *singular value decomposition* can be applied to the calibration measurements. Specifically for the NCO function, a method has been developed that makes use of the radiometric offset's spatial correlation (see section 4.3.2).

4.2.3. Blackbody-Blackbody Calibration

Combining equations 4.11 and 4.12 for the two reference blackbodies, one obtains for the IG α

$$\alpha^{i,j}(\nu) = \frac{B(T_{BB2}, \nu) - B(T_{BB1}, \nu)}{y^{i,j}_{BB2}(\nu) - y^{i,j}_{BB1}(\nu)} \tag{4.14}$$

Having thus determined α for each detector pixel (i, j), the NCO function β can be extrapolated using either one of the blackbody measurements:

$$\beta^{i,j}(\nu) = y^{i,j}_{BB} - \alpha^{i,j}(\nu) B(T_{BB}, \nu) \tag{4.15}$$

The extrapolation of β purely from blackbody measurements has been found to be problematic in the case of the TACTS and ESMVal campaigns. This is due to reference blackbodies having operated at temperatures around 20 K higher than expected in pre-campaign calculations (see Kleinert et al., 2014). Additionally, the temperature *difference* between both blackbodies was smaller, further exacerbating the magnification of uncertainties in T_{BBi} and y_{BBi}.

4.2.4. Blackbody-Deepspace Calibration

Instead of two blackbody measurements, it is also possible to use a single reference blackbody in combination with a deepspace measurement for calibration. The deepspace measurement is an atmospheric measurement using an elevation of 10°. Consequently, the instrument is pointing upwards (into space), instead of its regular limb geometry. Due to the exponential decay of atmospheric density with altitude, the total radiance integrated along the line of sight is low, and the radiometric offset becomes the chief component of the measurement. Ideally, the atmospheric radiance would be zero, i.e.

$$\beta^{i,j}(\nu) = y^{i,j}_{DS}(\nu) \tag{4.16}$$

Knowing the NCO function β, the IG parameter can be determined from the blackbody measurement using (4.15):

$$\alpha^{i,j}(\nu) = \frac{\beta^{i,j}(\nu) - y_{BB}^{i,j}}{B(T_{BB}, \nu)} \tag{4.17}$$

This kind of measurement is common for balloon and satellite instruments. One advantage over the previously introduced method (section 4.2.3) is that only a single reference blackbody is required, reducing instrument weight, power usage and overall complexity. Moreover, the extrapolation method in (4.15) magnifies uncertainties of the blackbody temperatures when they are propagated into the NCO function. However, the blackbody-deepspace method also has one prominent disadvantage: the ideal assumption that no atmospheric radiance is recorded does not hold true in practice for in-atmosphere instruments. Emissions from stratospheric trace species, especially ozone, show up in deep space measurements from balloons and especially aircraft due to their limited flight altitude. Spacecraft, of course, are not affected by this.

To alleviate this problem, the deep space measurements can be *shaved*, i.e. freed of trace gas emission lines, before use. This is achieved by performing forward calculations with the KOPRA model and then using an iterative approach described in Kleinert et al. (2014) to remove the stratospheric emissions.

4.3. Novel Techniques for the Radiometric Calibration

4.3.1. Three-Point Nonlinearity Correction

When the first calibration for the TACTS/ESMVal (see section 3.3.2) data set was developed, it became apparent that NCO and IG functions obtained from the blackbody-blackbody and blackbody-deepspace techniques (see sections 4.2.3 and 4.2.4, respectively) were inconsistent.

While it was expected that the blackbody-blackbody approach would yield a more accurate estimate of the IG and the deepspace variant a better NCO function, a systematic deviation of unknown origin persisted.

The signal from blackbody measurements is stronger than that of either deepspace or limb measurements. The inconsistencies between the two calibration methods leads to the hypothesis that the linearised instrument response varies with the total irradiance. For the nonlinearity correction applied at the Level-0 stage (see section 4.1.2), it is assumed that the detector response is linear except for capacitive saturation effects in the electronics. This effect is then corrected for with laboratory measurements that sample the range of the detector's analog-digital converter by varying the integration time while observing a constant radiation source (see Kleinert et al., 2014). However, this method cannot account for effects which are dependent on the strength of the incident light.

To compensate for this unexpected effect, the following empirically motivated ansatz was made *ad hoc* for the measured radiances:

$$y^{i,j}_{BB1}(\nu) = \lambda^{i,j}_1 a^{i,j}(\nu) B(T_{BB1}, \nu) + b^{i,j}(\nu) \tag{4.18}$$

$$y^{i,j}_{BB2}(\nu) = \lambda^{i,j}_2 a^{i,j}(\nu) B(T_{BB2}, \nu) + b^{i,j}(\nu) \tag{4.19}$$

$$y^{i,j}_{DS}(\nu) = b^{i,j}(\nu) \tag{4.20}$$

where the $\lambda_k \in \mathbb{R}$ are real-valued correction factors for the measured blackbody radiances. These factors are assumed to be fully correlated spectrally, but are allowed to vary freely across the detector array. The ansatz leads to a cost function

$$J(\lambda^{i,j}_1, \lambda^{i,j}_2) = \frac{\lambda^{i,j}_2 y^{i,j}_{BB2} - \lambda^{i,j}_1 y^{i,j}_{BB1}}{B_{BB2} - B_{BB1}} - \frac{\lambda^{i,j}_2 y^{i,j}_{BB2} - y^{i,j}_{DS}}{B_{BB2}} \tag{4.21}$$

which can be minimised using a least-squares optimisation algorithm such as the Levenberg-Marquardt method also employed for the Level-2

processing (cf. 2.3.3). Best results have been achieved by performing this fit at $\nu = 831\text{cm}^{-1}$. This spectral point lies within an atmospheric window region, i.e. trace gas emissions are negligible and most of the radiance is due to blackbody emissions from aerosols.[2]

The retrieved correction factors $\lambda_1^{i,j}$ and $\lambda_2^{i,j}$ are then applied to the blackbody radiances y_{BB1} and y_{BB2} prior to the standard blackbody-blackbody calibration (see section 4.2.3). It should be noted that the cause of the nonlinearity effect is currently not known and is still being investigated. Once the problem is identified, the method described in this section will be reevaluated.

4.3.2. Spatial Correlation of the Calibrated Offset

Obtaining the NCO function via blackbody-deepspace calibration is generally preferable to blackbody-blackbody calibration. However, both approaches yield rather noisy results for the individual pixels. If these noisy values are used to calibrate the atmospheric spectra, the resulting calibrated data exhibit an irregular radiance offset which is hard to account for. These offsets result in artifacts in the trace gas distributions retrieved in the Level-2 stage (see fig. 4.4). Therefore, a denoising of the NCO values is necessary at the Level-1 stage.

The GLORIA instrument's radiometric offset varies both spectrally and spatially, i.e. from pixel to pixel. The NCO is the *calibrated* radiometric offset and represents the instrument's self-emission. Due to this radiative nature of the NCO, it can be expected to vary smoothly across the detector, and be symmetric around a central point on the array. This can be exploited by fitting a radially symmetric function to the NCO values for each spectral point. The fitted values are then used to replace the original NCO before it is used to calibrate the atmospheric measurements.

[2] A neighbouring spectral range within the window is used for cloud detection, for the same reason (cf. 4.6.2).

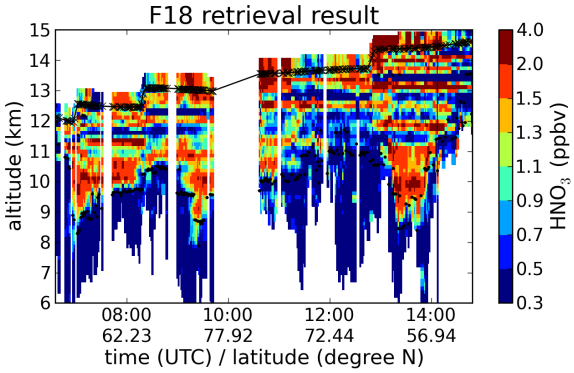

Figure 4.4.: *Effect of radiometric offset artifacts on retrieval cross-sections.*

The function currently used for this purpose is a pseudo-hyperbola of the form

$$\tilde{\beta}^{i,j}(\nu) = c + \left[b^4 + a^4((i - x_c)^2 + d^2(j - y_c)^2)^2\right]^{1/4} \tag{4.22}$$

with the fitting parameters being the symmetry axis position (x_c, y_c), the constant background radiation c and shape parameters a, b and d. Using this ad-hoc function, the shape of the NCO can be approximated very well, as is shown in 4.5.

4.4. The *gloripy* Software Suite

4.4.1. Motivation

In the previous sections 4.1 and 4.2.1, the Level-0 and Level-1 processing steps have been described separately. This reflects their original conception as to be performed by separate programmes and possibly on different hardware systems altogether. Coupled with GLORIA's exceptionally high data acquisition rate of over 70 MiBs/s, the amount of

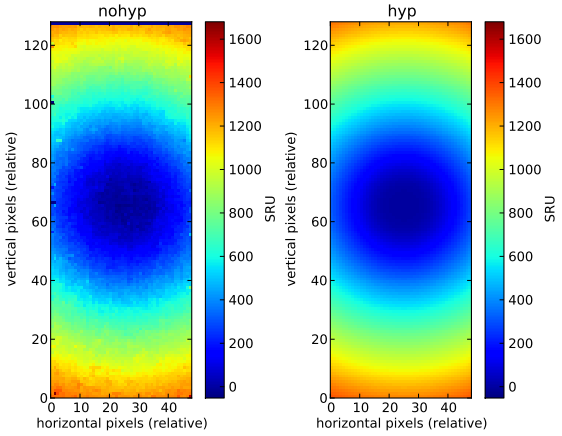

Figure 4.5.: *The NCO value for the detector pixels at* $\nu = 800.0\,\mathrm{cm}^{-1}$*, determined using a blackbody-deepspace calibration from the ESMVal flight on September 23rd, 2012. Figure a) shows the original values, figure b) the pseudo-hyperbola.*

human intervention inherent in this design was not practical. The number of different independent programmes also produced redundancies in the software codebases and the need to maintain multiple interfaces for the reading and writing of intermediate data.

One of the principal challenges for this work was to integrate the different components to create a unified processing chain. This has been realized in the form of *gloripy*, an integrated library that provides Level-0 and Level-1 processing algorithms and interfaces to connect them seamlessly. With the help of this new development, the timely availability of calibrated GLORIA measurements after the TACTS/ESMVal campaign (cf. section 3.3.2) was made possible. Preliminary Level-2 results suited for scientific pre-evaluation of the campaign flights were obtained in early 2013, and were ready to be presented at the EGU General Assembly in April of that year (Guggenmoser et al., 2013; Suminska-Ebersoldt, 2013). While finding the optimal calibration scheme for the TACTS/ESMVal data set is still an ongoing process, the necessary it-

erations of the whole processing chain are sped up significantly by the unified and highly automated framework provided by *gloripy*.

The following sections will briefly introduce the technical design of *gloripy* and highlight some of its most important features. As a concrete example for the synergy between the Level-0 and Level-1 components integrated into a single framework, the operational fringe count error correction is explained in detail.

4.4.2. Structure and Technical Overview

The *gloripy* software suite is designed around the following core principles:

Extensibility *gloripy* is designed to be easily modified and extended.

Integration All core processing components are contained within *gloripy*.

Automation The processing should be as automated as possible.

Minimal file I/O Critical processing paths should be performed completely in memory without file interfacing.

Simplicity At least the top-level components of *gloripy* should be kept simple and complexity hidden from the programmer.

It was decided early on that Python would be the project's main programming language. Python provides extensive library support, excellent readability, short development cycles and very easy interfacing with other programming languages, especially C and C++. Another advantage is scalability: auxiliary scripts, e.g. for plotting or automation, can be written in the same language as the core software and new functionality easily tested and integrated. Moreover, the JURASSIC2 retrieval processor already employed Python extensively, resulting in synergies between *gloripy* and the Level-2 processing stage.

A limited set of performance-critical operations, e.g. the complex calibration (cf. eq. 4.13), are implemented in the C++ language. These

procedures are bundled in a single extension module, with front-end interfaces within the main Python layer hiding the implementation details from *gloripy* users.

In addition, *gloripy* incorporates the Level-0 processor (see section 4.1), written in the C language, as an integral component. This is a heavily modified version of the original C code fitted with an extensive Python interface which can be used seamlessly from the rest of *gloripy*. An example of how this is done in practice is the linear phase correction described in section 4.4.5. Even parts of *gloripy* that are not related to Brault resampling at all benefit from this integration. For instance, the highly optimised interferogram data reading and transposition routine is implicitly used whenever interferogram cuboids are read in *gloripy*, completely hidden from the user.

The most important end-user application in the *gloripy* suite is the *JULAF* automated processor which reads raw interferograms, together with pregenerated calibration data, and produces calibrated spectra. It employs the Level-0 and Level-1 algorithms implemented in *gloripy* to efficiently process the data without intermediate data storage or human intervention.

4.4.3. The Level-0 Processing Submodule

The Level-0 processor (see 4.1) has been heavily restructured and modified for integration in *gloripy*. It is now modeled as an *object*, i.e. a collection of functions coupled with a *state* containing all relevant data structures. This means that the individual functions it implements can be accessed and the results read out from other parts of *gloripy* as needed.

Together with the integration, the code has also generally be made much more flexible. For instance, the original version required recompilation for frequently occuring changes in parameterisation from measurement to measurement, and could only run the resampling on the whole measurement. Crucial processing steps such as the linear phase

correction described in section 4.4.5 can now run the Level-0 code efficiently on a restricted selection of pixels, and with fully flexible runtime parametrisation.

4.4.4. Level-1 Processing

As has been discussed in section 4.2, the Level-1 stage encompasses the transformation of the spatially sampled Level-0 product into the spectral domain and subsequent radiometric calibration.

For the Fourier transform, the high-performance FFTW[3] library is used (Frigo and Johnson, 1998) which dynamically selects the best algorithm for any given interferogram input length. As the recorded interferograms are all real-valued, the *RFFT* class of algorithms is used after the input data have been converted to 64-bit floating point numbers.

In order to calibrate the resulting spectra, pre-generated IG and NCO calibration values are needed. These can be produced with auxiliary scripts included in *gloripy*, following the methods outlined in section 4.2. The IG and NCO values for a given measurement are calculated via linear interpolation between the calibration sequences, and the complex calibration itself is performed in a parallelised C++ subroutine for efficiency.

4.4.5. Linear Phase Correction

GLORIA records two-sided interferograms, with the ZOPD point approximately in the centre of the measurement. However, in practice, the measurement will never be exactly centred around this point. A similar effect occurs whenever the reference laser interferometer misses one of the rising zero-crossings, also denoted as *fringes*. This is known as a *fringe count error* (FCE) and will result in a missing timestamp in the laser reference time axis (cf. section 4.1.2). These FCEs typically occur when the interferometer is in its turnaround phase between two

[3] *Fastest Fourier Transform in the West*

measurements. In this case, they will result in a shifted spatial axis after the Level-0 processing is complete.

A constant shift of the interferogram caused by either non-centered ZOPD or turnaround-FCEs will lead to a linear phase component in the spectrum (see appendix B.1.3). As the occurence of this shift is rather arbitrary, there will not necessarily be a correlation between atmospheric and calibration measurements, or indeed between any two measurements at all. In consequence, the effect cannot be compensated by complex calibration and needs to be handled separately for each measurement at the Level-0 stage, i.e. the spatial shift has to be found and the interferogram resampled anew.

A method for the correction of linear phase components has been developed for the ESSenCe campaign data by Kleinert et al. (2014) (see also the ESA campaign report Kaufmann et al. (2013)). Taking advantage of the integrated Level-0 and Level-1 environment provided by *gloripy*, this procedure has been successfully automated as part of this work. The new algorithm works as follows:

1. Data from the interferogram and laser timestamp files are read using the optimised Level-0 processing library.

2. The pixel closest to the optical axis position is selected and Brault-resampled using a first guess for the resampling parameters.

3. From the processed centre interferogram, the maximum position, approximated by Fourier interpolation, is taken as a proxy for the ZOPD. A new spatial axis is calculated centred around this point. This step removes the greatest part of the linear phase slope and is essential to ensure that the residual slope can be fitted in step 6.

4. A rectangular selection of 11x11 resampled interferograms around the optical axis are coadded and Fourier transformed and the phase angle ϕ of the spectrum is computed. In order to reduce

the influence of noise, the interferogram is processed with a truncated length of 10 mm, i.e. a spectral sampling of $5.0\,\mathrm{cm}^{-1}$.

5. A *standard phase* is subtracted from the spectrum's individual phase. This phase is determined from the averaging of blackbody measurements. It represents the general baseline phase of the atmospheric port (cf. 2.1.5).

6. A linear regression fit is performed on the residual phase in a limited spectral range between 1025 and $1060\,\mathrm{cm}^{-1}$. This region is dominated by strong ozone emissions in atmospheric measurements, thereby ensuring that the atmospheric port is the principal component of the signal. The intercept of the linear fit is set to zero.

7. The slope $m = \frac{\partial \phi_{\mathrm{lin}}}{\partial \nu}$ of the linear phase component ϕ_{lin} is used to compute the associated interferogram shift (see appendix B.1.3 for a derivation):
$$s = -\frac{2L\Delta x \Delta \nu}{\pi} \tag{4.23}$$
where $L = 0.1\,\mathrm{cm}$ is the length of the interferogram and $\Delta\nu$ and Δx are the spectral and spatial sampling, respectively.

8. The abscissa used for the resampling of the central 11x11 pixels is shifted by s and subsequently used to finally resample the full measurement, completing the Level-0 stage.

At the end of this linear phase correction, the interferogram is ready for the full Fourier transform and subsequent calibration.

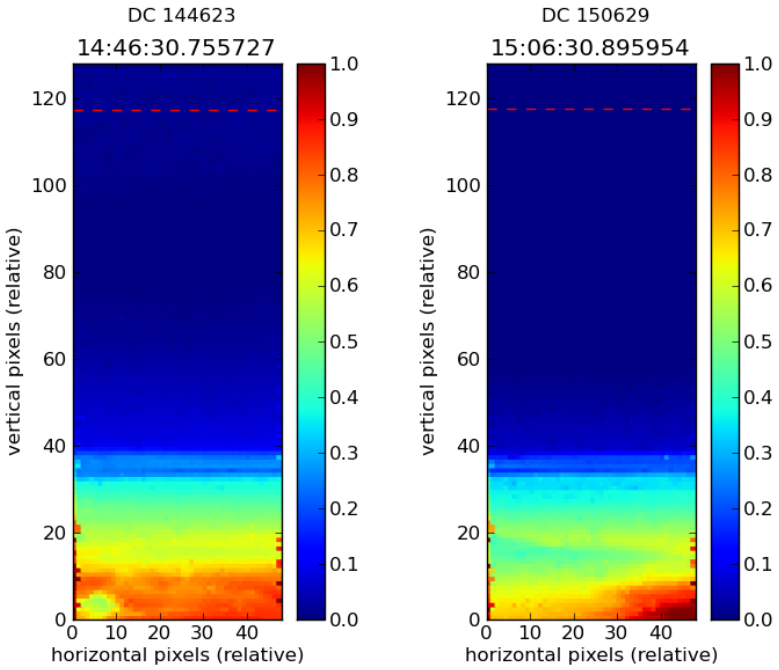

Figure 4.6.: *Example DC-processed GLORIA measurements from the ESSenCe campaign. Both images were recorded during ESSenCe Flight 2 on December 16th, 2011. The colour scale represents the total irradiance for the 48x128 detector pixels in normalised units. The dashed red line represents GLORIA's horizon, i.e. the zero-elevation line. In both images, tropospheric clouds are visible as especially bright infrared sources in the lower third of the image. Additionally, a thin layer atop the tropopause can be identified, which suggests the presence of cirrus clouds in the field of view. Both images were produced by DC extraction at a rate of 25 Hz, providing a time resolution of 40 ms.*

4.5. Raw Data Pre-Analysis

4.5.1. DC Image Visualisation

The core data processing chain developed for GLORIA works only on the AC-coupled component of the recorded interferograms. The unmodulated DC component, however, can still be extracted from the raw, undetrended data files.[4] Considering eq. (2.4), it becomes clear that the DC-coupled part of the signal is a direct measure of the *total irradiance*, i.e. the spectral radiance integrated over the detector's whole sensitivity range. As the AC component is periodic, the DC component can be obtained (approximately) by simply computing the arithmetic mean over either a whole interferogram or a sufficiently large number of frames therein.

This DC signal can then be used outside of the main processing path for diagnostic and visualisation purposes. For the ESSenCe campaign, a simple DC processing chain was developed. The goal was to gain an overview of the measured scene, especially horizon position and stability as well as cloud presence and structure. By foregoing the spectral information contained indirectly in the AC part and processing only the total irradiance, GLORIA can be effectively used as a high-speed infrared camera.

In a first step, the DC signal is extracted from the input cuboid file by calculating the average of non-overlapping time windows over the raw time-sampled interferograms for each pixel. The width of these windows is determined by the desired frame rate. Of course, as the DC window size approaches the time sampling, the AC component will become less completely removed.

A second step then involves calibrating these data, using DC values from blackbody and deep space measurements. The absolute scale of the DC images can be arbitrary; the calibration only serves to homogenise the image by removing variations of the instrument response from pixel

[4] See section section 2.1 for an explanation of the AC and DC signal components.

to pixel which would otherwise significantly impair the image quality.

Figure 4.6 shows DC images with an averaging rate of 25 Hz from ESSenCe Flight 2 measurements, with cloud structures in the troposphere and a thin layer in the stratospheric portion clearly visible. It should be noted here that a pixel near the centre of the image has a vertical extent of around 125 m at the tangent height; the images thus demonstrate very effectively GLORIA's capabilities to yield spatially highly resolved measurements in the UTLS region. The configurable framerate also provides a time resolution below the actual interferogram scanning time. For a first qualitative survey of the scenery and attitude stability, DC images were generated from longer timeframes and animations were then produced from these samples, making pointing variations and moving cloud structures discernible.

4.5.2. Raw Data Spectral Analysis

In the preceding section, a method was described to obtain time-resolved information about the total measured irradiance from the raw CUB data. In a similar vein, one can also obtain spectral information for a specific time from the raw data with a moving-window approach.

The motivation for such an analysis comes from several odd features seen in the processing products (uncalibrated and calibrated spectra) from GLORIA interferograms recorded during the TACTS and ESMVal campaigns. In fig. 4.7, for instance, one can see several apparent emission or absorption lines in an otherwise smooth (apart from noise) blackbody calibration measurement.

Two properties of these lines are particularly noteworthy. The first is their spacing: they seem to be distributed equidistantly across the spectrum, at multiples of the leftmost one at $\nu_0 \approx 376.875\,\mathrm{cm}^{-1}$. The second fact to consider is that some of the lines, including the one at ν_0, appear far outside the detector sensitivity range, which begins and ends at roughly $750\,\mathrm{cm}^{-1}$ and $1450\,\mathrm{cm}^{-1}$, respectively. Together, these two properties indicate that they are an electronic disturbance rather

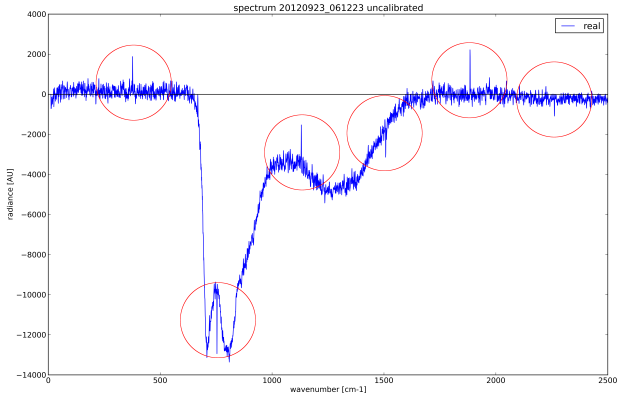

Figure 4.7.: *Example calibration blackbody measurement (real part only) from the ESMVal flight performed on September 23rd, 2012. The spectrum has not been calibrated; the spectral radiance values are therefore given in arbitrary units. Clearly visible are several apparent emission or absorption lines which correspond to time-domain frequencies of almost exactly 500 Hz and multiples. Also, the lines appear outside the detector sensitivity range, furhter indicating that they may be due to an electric disturbance.*

than an optically coupled signal. The optical interferogram consists of a superposition of oscillations in the spatial domain.[5] A "rogue signal" coupled into the detector read-out or data acquisition circuitry, on the other hand, can be expected to be an oscillation in the time domain.

For an exact identification of these rogue frequencies, the signal has to be analysed in the time domain, i.e. the original raw CUB files have to be investigated. This can be done by computing a windowed Fourier transform along the time axis of the interferograms. An example of this technique is presented in figure 4.8, where it has been applied to the data of the ESMVal flight conducted on September 13th, 2012. At

[5] Refer to 2.1 for an introduction into the principles of Fourier transform spectrometry.

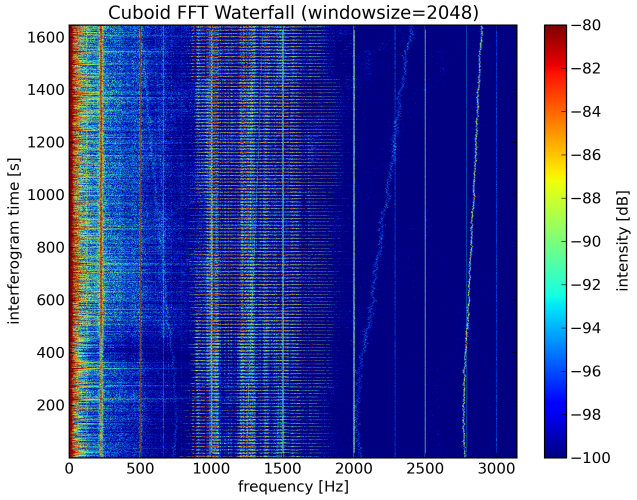

Figure 4.8.: *Spectral analysis of raw time domain interferograms recorded during the ESMVal flight on September 13th, 2012, from Cape Verde to South Africa. The horizontal lines between 900 and 1800 Hz are the intensitites in the sensitivity range of the infrared detector at the ZOPD point. Very pronounced components exist constantly at about 500 Hz and multiples thereof.*

500 Hz and its harmonic overtones at 1000, 1500, 2000 and 2500 Hz, a peak is visible consistently across all analysed interferograms.

Usually these disturbances are not particularly important because they very well localised in the spectrum and can just be avoided in the Level-2 processing. However, they present a problem whenever spectra are smoothed, because then their energy is spread out over a wider wavenumber range. Therefore, whenever smoothing of any kind is performed, the rogue peaks have to be interpolated first.

4.6. Level-2 Processing

4.6.1. The JURASSIC2 Retrieval Processor

Radiative transfer calculations in the atmosphere (see section 2.2) are computationally expensive when performed for each emission line separately. The retrieval of trace gas distributions from recorded measurements, as presented in section 2.3, is an iterative process that calls for repeated evaluation of the radiative transfer model. Consequently, whenever a fast trace gas retrieval is desired, a fast forward model is a natural first step. This is especially true for instruments with a high measurement density such as GLORIA.

JURASSIC2[6] is a comprehensive software suite developed and employed to derive trace gas volume mixing ratios, temperature and other interesting quantities from GLORIA dynamics mode measurements. At its core, it consists of a C++ library (libjurassic) with the JURASSIC forward model and a collection of numerical inversion algorithms dubbed JUTIL[7].

The JURASSIC forward model rapidly simulates radiative transfer through the atmosphere using pretabulated emissivity or optical path values and a combination of the *Curtis-Godson Approximation* (CGA, see Curtis, 1952; Godson, 1953) and *Emissivity Growth Approximation* (EGA, see Gordley and Russell, 1981). The comparatively low spectral sampling of the GLORIA dynamics mode allows for the use of *integrated spectral windows* (ISWs) instead of line-by-line calculations, an approach based originally on the BANDPAK model (Marshall et al., 1994) and applied to CRISTA measurements (Riese et al., 1997, 1999a). The success of these applications motivated the development of the JURASSIC model (see Hoffmann et al., 2005). Tables for JURASSIC calculations are computed using a line-by-line radiative transfer model, in practice the Reference Forward Model (RFM).

[6] Jülich Rapid Spectral Simulation Code version 2
[7] Jülich Tomographic Inversion Library

In addition to the rapid forward model, JURASSIC2 also features an improved inversion library optimised for large-scale 3-dimensional tomographic retrievals (see Ungermann et al., 2011). It has been designed specifically for the retrieval of spatial structures using high-resolution instruments such as GLORIA. Most recently, it was used successfully for studies of UTLS dynamics with GLORIA's precursor instrument CRISTA-NF by Ungermann et al. (2012, 2013). First results from a tomographic flight during the TACTS/ESMVal campaign have been presented by Blank (2014).

4.6.2. GLORIA Preprocessing

Cloud Filtering

Clouds are quasi-greybody radiation sources with high emission and absorption in the infrared range. Due to this, infrared limb sounding instruments such as GLORIA, MIPAS or CRISTA are highly sensitive to the presence of clouds in their line of sight. The greybody emission quickly obfuscates the signature of the atmospheric trace gases that one is interested in measuring. When coadding detector pixels from an imaging instrument, special care has to be taken to ensure that no cloudy pixels enter the aggregated superpixel.

Spang et al. (2004) have presented a method for cloud detection using infrared spectra, originally for the CRISTA instrument, later adapted to the MIPAS and CRISTA-NF instruments. The CRISTA-NF variety (see Spang et al., 2008) has been adapted for use with GLORIA measurements.

The *cloud index* CI is a colour ratio defined as

$$CI = \frac{rad_{\mathrm{SW1}}}{rad_{\mathrm{SW2}}} \tag{4.24}$$

where rad_{SW1} and rad_{SW2} are the mean radiances for two distinct spectral windows. The windows are chosen such that SW1 contains a strong

trace gas emission, whereas SW2 is situated in an *atmospheric window* region and is therefore dominated by aerosol and cloud emissions. The stronger these emissions are, i.e. the lower CI is, the higher is the likelihood of cloud or dense aerosol presence at or near the tangent point.

For GLORIA dynamics mode measurements, the colour ratio windows have been chosen as

$$\begin{aligned} \text{SW1}: &\quad 791.00\text{cm}^{-1} <= \nu <= 793.00\text{cm}^{-1} \\ \text{SW2}: &\quad 832.30\text{cm}^{-1} <= \nu <= 834.40\text{cm}^{-1} \end{aligned} \tag{4.25}$$

This choice provides high contrast and is thus suited for a high-sensitivity setup which filters clouds very conservatively, i.e. erring on the side of false positives. For a less sensitive setup which also allows for the separation of clouds from e.g. high amounts of tropospheric water vapour, an altitude-dependent threshold is necessary.

Note that, mostly due to the low emission in region SW2, the cloud index is susceptible to calibration errors. If $\Delta\beta_1$ and $\Delta\beta_2$ are small *systematic* deviations of the radiances in SW1 and SW2, then the resulting cloud index $\widetilde{CI}$ will be

$$\widetilde{CI} \approx CI \left\{ 1 + \left(\frac{\Delta\beta_1}{rad_{\text{SW1}}} \right) - \left(\frac{\Delta\beta_2}{rad_{\text{SW2}}} \right) \right\} \tag{4.26}$$

Similarly, noise errors Δrad in the calibrated spectra are propagated like

$$\Delta CI = CI \sqrt{ \left(\frac{\Delta rad_{\text{SW1}}}{rad_{\text{SW1}}} \right)^2 + \left(\frac{\Delta rad_{\text{SW2}}}{rad_{\text{SW2}}} \right)^2 } \tag{4.27}$$

Because the radiance in SW2 is, by design, typically much smaller than in SW1, absolute offset or noise erros in SW2 correspond to a higher relative error. At the time of writing, the instrument characterisation of GLORIA is still under completion. For further studies on clouds along the lines of e.g. Spang et al. (2008), the method will have to be refined, e.g. by including the spatial information provided by the detector array.

Pixel Coaddition

As a limb imager, GLORIA uses a 2-dimensional focal plane array to detect incoming radiance. In theory, the 48x128 pixels could be interpreted as 48 vertical profiles and processed separately. However, this is impractical for several reasons.

Due to inevitable imperfections in the detector, not all pixels are functional. In the most extreme case, a pixel may be "dead", i.e. provide no signal at all, or have a constant output voltage. These parts of the detector array cannot be used at all; if separate profiles were retrieved for each of the columns, this would result in information gaps corresponding to several hundred metres in the plane of tangent points. Less extreme cases are mostly given by inhomogeneous noise levels over the detector array. Finally, the overall noise level of the individual pixels outweighs the use of retrieving individual profiles.

Instead of retrieving a profile for each individual detector column, the calibrated GLORIA measurements are first averaged along the horizontal direction, yielding one vertical profile per image. When the individual pixel's relative noise characteristics are known, the averaging can be performed using a weighting matrix $\mathbf{W} = w_{ij} \in \mathbb{R}^{128\times48}$:

$$w_{ij} = \begin{cases} 0 & \text{if pixel } ij \text{ broken or cloudy} \\ \sigma_{ij}^{-2} & \text{else,} \end{cases} \tag{4.28}$$

where σ_{ij}^2 is the expected noise variance of the respective pixel, and the filter presented in 4.6.2 is used for the "cloudy" criterion. The averaging of a given horizontal detector line is only performed if the number of finite weights w_{ij} exceeds a configurable threshold. In this work, the noise variance weighting is not used because the detector characterisation is incomplete. A threshold value of 12 is used, i.e. any line that has fewer than a quarter of its pixels left unmasked is discarded completely.

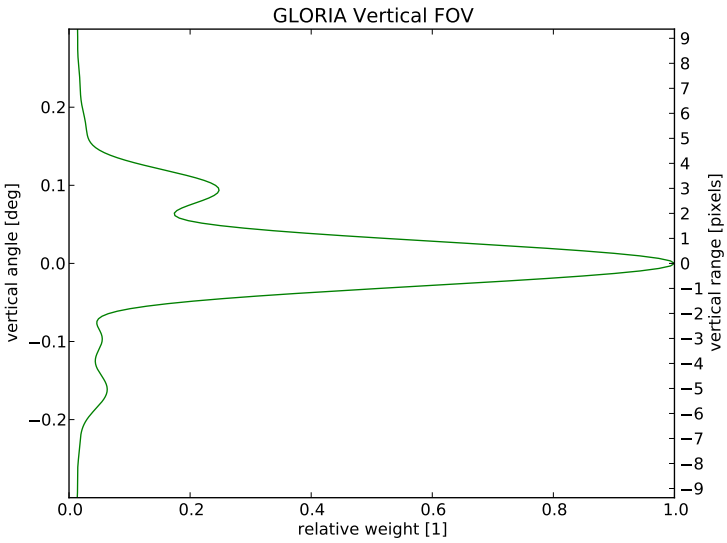

Figure 4.9.: *The vertical field of view weighting function of GLORIA.*

Preparation of Radiative Transfer

The Level-2 algorithm works by fitting a simulation of the measurement to the actual measurement (see section 2.3). Before the retrieval can be performed, the radiative transfer along the line of sight through the atmosphere has to be set up to accurately model the GLORIA observation.

Each detector pixel registers light from a range of directions, its *field of view* (FOV). The weight with which each direction contributes to the total irradiance is consequently called the *field of view function*. This function is known from laboratory measurements and optical model calculations. For each coadded line of pixels, the vertical field of view function (see fig. 4.9) is used to assign weights to three rays used to calculate the radiative transfer. As the horizontal dimension is averaged over, only the vertical FOV function is considered.

5. Calibration and Level-2 Results for Flight 18

During the TACTS and ESMVal campaigns, a large volume of data[1] was recorded by GLORIA during 12 scientific flights. The ESMVal flight conducted on September 23rd, 2012 is among the dynamically most interesting ones. As an application of the processing chain laid out in chapter 4, a subset of this flight's measurements is processed and Level-2 results are presented and compared with the result of computations from the *Chemical Lagrangian Model of the Stratosphere* (CLaMS, McKenna et al., 2002).

Note that the Level-2 processing in this work will limit itself to the retrieval of one-dimensional vertical trace gas and temperature profiles. Improvements of the vertical resolution may be possible in the future by employing a pseudo-2D approach with horizontal regularisation along the lines of Ungermann (2013). Another technique not explored here is linear flight tomography which exploits the multiple-angle coverage provided by the azimuth panning in dynamics mode. This method has been described by Ungermann et al. (2011), but has yet to be applied to real-world measurement data as of the time of writing.

5.1. Selection of Measurements

The calibrated measurements were preprocessed using the method described in section 4.6.2. For the cloud screening algorithm, a rather

[1] more than 25 TiB

conservative filter of $CI <= 5.5$ was chosen to further reduce the likelihood of residual cloud signatures entering the trace gas retrieval. As has been briefly explained in section 4.6.2, the cloud detection is sensitive to calibration errors, and can therefore be configured less conservatively as GLORIA's post-flight characterisation progresses.

For the analysis presented in this section, only a subset of the measurements was processed. These were selected according to the following criteria:

- Only the measurements with forward-moving interferometer slide were processed. The two available directions have to be calibrated separately, possibly introducing biases that make combined analysis problematic.
- The selection has been further reduced to measurements which are perpendicular to the aircraft's heading. This choice allows for the presentation of retrieval results in the form of cross-sections through the observed atmosphere along the flight path.
- Chemistry mode and dynamics mode measurements were both processed. For this purpose, chemistry mode interferograms were shortened to be technically identical to dynamics mode measurements.
- The sampling was reduced to at most 1 profile per minute.

The purpose of this reduction is to generate an overview over the whole flight that can be readily interpreted as a spatial cross-section with each air mass only measured once.

5.2. Calibration

Calibration data for flight 18 have been produced using the methods described in section 4.2. Due to data acquisition issues during the cam-

Number	Time (UTC)	Type
04	10:31	2BB + DS
07	11:38	2BB + DS
10	13:46	2BB + DS

Table 5.1.: *Calibration sequences used for the processing of flight 18. The first column is the identification tag of the calibration sequence; omitted numbers signify that a nominally existing calibration sequence was unusable because of issues with the data quality. The second column is the average UTC timestamp used for interpolation between the sequences.*

paign, one of the blackbodies has significantly fewer measurements available than the other. In these cases, calibration data can be generated using the other blackbody and deepspace measurements (see section 4.2.4). When both blackbodies and deepspace measurements were available, the more advanced three-point method described in section 4.3.1 can be employed. In order to avoid inconsistencies due to systematic differences between the calibration data, only the sequences that allowed for the full three-point method were used to calibrate the measurements in this chapter. Additionally, the very first calibration sequence has been discarded because the measurements have been taken during the aircraft's ascent from the troposphere. As the instrument components experience much faster thermal variations during such a manoeuvre, the resulting calibration does not model the instrument response on a long enough scale. The NCO function for the three remaining calibration sequences has been smoothed using the pseudo-hyperbola fit discussed in section 4.3.2. Each of the calibration functions was assigned the average timestamp of the sequence. For each measurement to be calibrated, the real and imaginary parts of the IG and NCO function were found by linear interpolation between these calibration points.

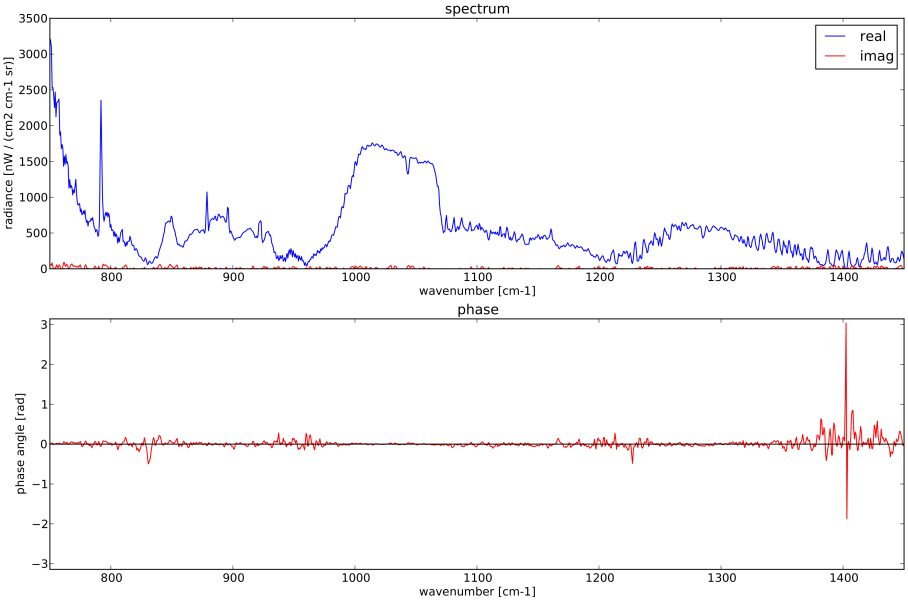

Figure 5.1.: *An example of a single-pixel calibrated atmospheric spectrum recorded during Flight 18. After calibration, the imaginary part (red curve in the top plot) is zero except for noise. Consequently, the phase angle (bottom plot) also vanishes.*

5.3. Synoptic Situation

The ESMVal flight conducted on September 23rd 2012, or *GLORIA Flight 18*, was the last measurement flight performed for the ESMVal campaign, as flights 19 and 20 were both TACTS flights. Technically a "local flight" in that the start and end point were the campaign base at Oberpfaffenhofen, Germany, the flight path itself went as far north as 80°N (above Svalbard), offering insight into a highly dynamic meteorological situation along an extensive flight path.

An important indicator for the origin of air masses is potential vorticity (PV). In an equilibrium state, the troposphere would consist only of low-PV air masses, while PV values above the tropopause would rise with altitude. When exchange processes between the troposphere and stratosphere occur, however, this monotonous behaviour can be broken due to the PV value of an air parcel being conserved until subjected to diabatic heating processes. In the absence of these, tropospheric air masses transported into the stratosphere will carry their low-PV field with them and assimilate only slowly into their surroundings via mixing.

Figure 5.2 shows the horizontal distribution of potential vorticity at 12:00 UTC on the day of of Flight 18, using data from ECMWF at three different altitude levels. A very prominent feature, especially at the 12 and 14 km levels, is the circular structure between about 60–80° N latitude and 10° W–10° E longitude, marked as region B. The evolution of ECMWF PV data during the days prior to the flight, shown in figure 5.3, suggests that this structure is a remnant of an eddy originally created by a Rossby wave breaking event in the mid-latitudes (about 40° N). Such wave breaking events facilitate irreversible stratosphere-troposphere exchange (STE) in that they transport tropospheric air from the extratropics into the polar stratosphere (see Holton et al., 1995, and references therein).

The PV distribution on the day of the flight suggests that precisely such an event has taken place. The air, originally from the subtropical upper troposphere, seems to have been transported horizontally into the

polar lower stratosphere and is still distinguishable from the surrounding regions at the same pressure level. The remnant of the wave-breaking event forms an anticyclone in the northern part of the measurement flight. At the same time, a cyclone exists in the southern part (regions A and A'), which forms a vertically localised layer of high-PV air around 10 km. This is unusual and suggests that the air just above the tropopause is stratospheric in character, but bordered from above by tropospheric air.

5.4. Trace Gas Retrieval

5.4.1. Retrieval Setup

The retrieval (see section 2.3) was set up with the 15 spectral windows listed in table 5.2. As the a posteriori instrument characterisation of GLORIA is still ongoing at present, the measurement error covariance matrix $\mathbf{S}_\epsilon$ was set up using a priori predictions of the noise equivalent spectral radiance. The spectral averaging over n samples has been accounted for by assuming fully Gaussian errors, i.e. the standard deviation is assumed to be reduced by a factor of $\sqrt{n}$.

For regularisation, the Tikhonov approach presented in section 2.3.2 is employed using a priori data based on the MIPAS initial guess climatology (Remedios, 1999). Some a priori data are instead taken from ECMWF (H_2O and temperature). Assumed volume mixing ratios for non-retrieved constituents are also read from this a priori data set, with CO_2, HCFC-22, CFC-11 and CH_4 values taken from WACCM.

In addition to the principal targets temperature, nitric acid, ozone and water vapour, presented in the next section, auxiliary targets have been retrieved, namely the chlorofluorocarbon CFC-12 and five aerosol extinction channels. CFC-12 does not show high variability within the limited altitude range that can be measured from the HALO aircraft, but needs to be fitted because it emits signal in one of the spectral windows used for the retrieval of HNO_3. The aerosol channels serve

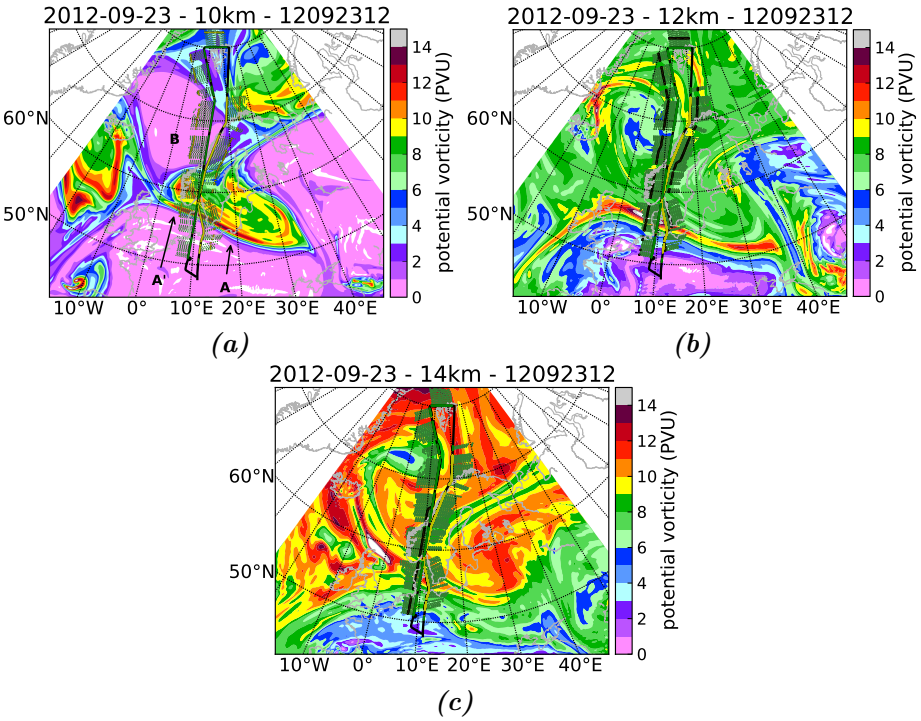

Figure 5.2.: *Synoptic situation for ESMVal Flight 18. Both figures show ECMWF data for potential vorticity. Figure a) shows the situation at 10 km altitude, figure b) at 12 km and figure c) at 14 km. The HALO aircraft's flight path is coloured according to the GLORIA measurement mode: yellow segments denote dynamics mode measurements, green segments mean the instrument was operated in chemistry mode. A subset of tangent points is included to show the areas from which the measurement data were sampled. The regions marked A and A' are where GLORIA measured a high-PV cyclone structure in the lowermost stratosphere and region B is a volume of low-PV air. These regions correspond to those in fig. 5.4.*

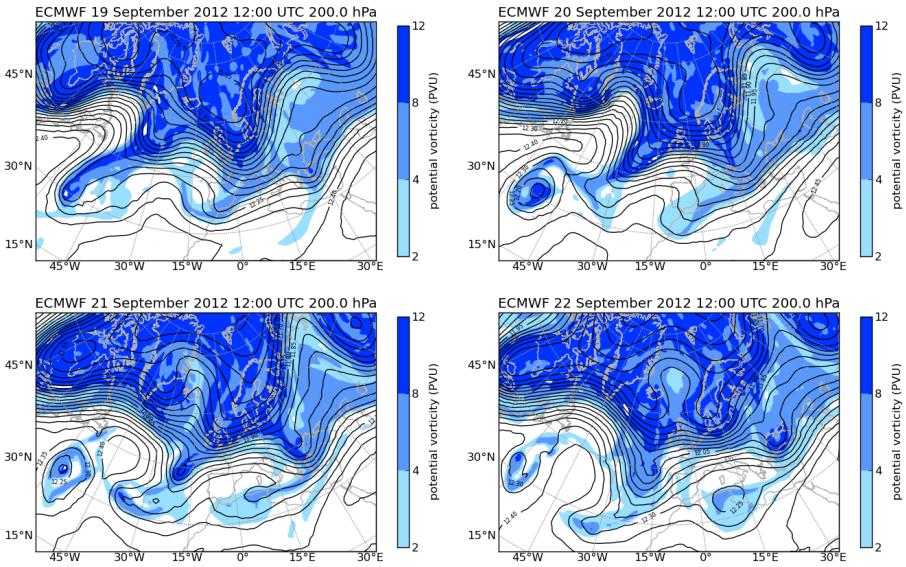

Figure 5.3.: *ECMWF potential vorticity data at a fixed pressure level during the days prior to Flight 18. A wave breaking event in the extratropics is seen which transports low-PV tropospheric air further north into the target volume of GLORIA. Figures courtesy Dr. Jörn Ungermann.*

Centre freq. cm^{-1}	Range cm^{-1}	Samples 1	Noise $W/m^2cm^{-1}sr^1$
792.1875	790.6250–793.7500	6	1.5152e-04
797.1875	795.6250–798.7500	6	1.5152e-04
847.1875	845.0000–849.3750	8	1.3122e-04
852.1875	850.0000–854.3750	8	1.3122e-04
885.9375	883.7500–888.1250	8	7.4982e-05
894.3750	892.5000–896.2500	7	8.0159e-05
901.5625	900.0000–903.1250	6	8.6581e-05
920.9375	918.7500–923.1250	8	7.4982e-05
959.6875	956.8750–962.5000	10	6.7066e-05
982.1875	980.0000–984.3750	8	7.4982e-05
995.0000	992.5000–997.5000	9	7.0693e-05
1003.4375	1000.6250–1006.2500	10	6.7066e-05
1012.1875	1010.0000–1014.3750	8	7.4982e-05
1390.9375	1388.1250–1393.7500	10	6.7066e-05
1396.5625	1394.3750–1398.7500	8	7.4982e-05

Table 5.2.: *Spectral windows and associated noise levels utilised for the trace gas retrieval. The noise values have been determined from simplified model predictions performed during instrument development. These estimates are subject to change once instrument characterisation has progressed further.*

to account for spectrally smooth residual calibration errors, as well as actual atmospheric aerosol extinction along the line of sight.

An offset error of $5\,nW/cm^2cm^{-1}sr$ and a gain error of 1% have been assumed to account for remaining uncertainties in the calibration. Additionally, the attitude control system is assumed to keep the elevation angle stabilised with an error of 0.023°, and a general elevation offset of 0.1°is added. The elevation offset was estimated from qualitatively comparing retrieved temperature profiles with those obtained from ECMWF; it is subject to change as the post-flight characterisation of the attitude control system is performed.

5.4.2. Retrieval Results

Cross-Sections and Observed Structures

Cross-sections consisting of the retrieved vertical profiles for nitric acid, ozone, water vapour and temperature are shown in figures 5.4 through 5.7. In addition to the retrieval results, the vertical resolution as estimated from the width of the averaging kernels (see section 2.3.4) and CLaMS simulations are plotted on the same grid for comparison. For both nitric acid and ozone, a resolution of 200–500 m is achieved which improves with increasing altitude. Water vapour is resolved typically between 300 and 700 m, with worse results toward the end of the flight. Temperature has been regularised more heavily than the other targets, resulting in a resolution between 500 m and 1 km.

For the most part, the measurements and the CLaMS simulations agree qualitatively with regard to the spatial structures observed, which is especially visible for HNO_3. However, the retrieved volume mixing ratios in the lowermost stratosphere appear to be systematically higher than those predicted by CLaMS. In order to understand the dynamical situation better, it is useful to compare the retrieved cross-sections with the PV plots in fig. 5.2, and the PV cross-section shown in fig. 5.8. The eddy created by the breaking Rossby wave creates an anticyclone that is measured by GLORIA during the south-bound returning leg of the flight, between approximately 80° N and 60° N. In both fig. 5.4 and 5.2, the region is marked B. Because HNO_3 is a stratospheric tracer, low values of it are indicative of relatively young air masses that have entered the stratosphere recently and are in an early state of mixing. In the measurements of region B, a volume of particularly low HNO_3 occurence that extends up to flight altitude has been imaged by GLORIA. Volume mixing ratios for nitric acid of less than 0.3 ppbv can be observed up to a height of 13 km in this region. Between 11:00 UTC and 12:00 UTC, an almost isolated filament of what appears to be older air from the polar stratosphere is visible. Within the core of the filament, HNO_3 assumes

volume mixing ratios between 1.0 and 1.5 ppbv.

Another interesting phenomenon occurs on the north-bound leg of the flight, between 55 and 65° N, corresponding to the time between 07:00 and 08:30 UTC. These measurements correspond to the high-PV cyclone structure at 10 km in fig. 5.2 (region A). GLORIA observations show high occurrence of HNO_3 in this region and low occurrence above, consistent with the elevated ECMWF PV values. Between 13:00 UTC and 14:30 UTC (region A'), towards the end of the south-bound leg, the smaller western part of this structure is observed, where the troposphere forms a "trough" filled with very HNO_3-rich air. What is remarkable about this observation is that stratospheric air seems to be trapped between the tropopause and a layer of originally tropospheric air. Interestingly, the measurements of the cyclone are the ones that differ most significantly from the CLaMS simulation.

Origin of Air Masses

To investigate this further, backwards trajectories were calculated starting from the GLORIA retrieval grid. For these computations, the CLaMS trajectory programme *traj* was employed using wind data from ECMWF. The backwards trajectories obtained from *traj* trace the origins of air parcels through time, and can be used as an aid in the interpretation of the GLORIA results. Figure 5.9a shows 96-hour backwards trajectories for the measurements between 07:00 UTC and 08:00 UTC, for tangent points in an altitude range between 10 and 12.3 km. These are the measurements of the high-PV cyclone observed at the beginning of the northbound leg of Flight 18 (region A). This seems to confirm the initial view that this typically tropospheric air mass has been transported into the stratosphere by an STE (stratosphere-troposphere exchange) process.

The anticyclone observed during the southbound leg can also be investigated in this manner (see fig. 5.9b). To this end, trajectories were calculated backwards from the measurements between 11:10 UTC and

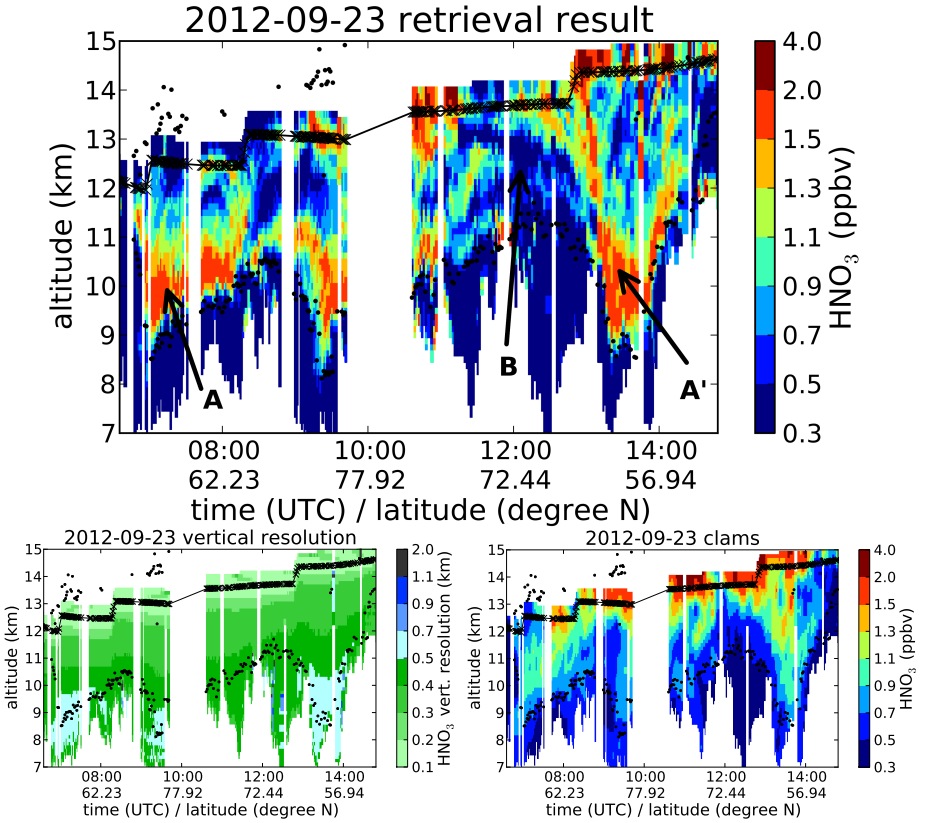

Figure 5.4.: *Cross-sections of Level-2 results, vertical resolution and CLaMS calculations for nitric acid during Flight 18, performed on September 23rd, 2012. The black crosses near the top of the plotted data represent the aircraft (and instrument) altitude. Black dots are estimates of the thermal tropopause derived from the GLORIA temperature retrieval and contain artifacts for some profiles. The marked observations correspond to the high-PV cyclone (A and A') and the low-PV anticyclone (B) seen in the ECMWF data (fig. 5.2).*

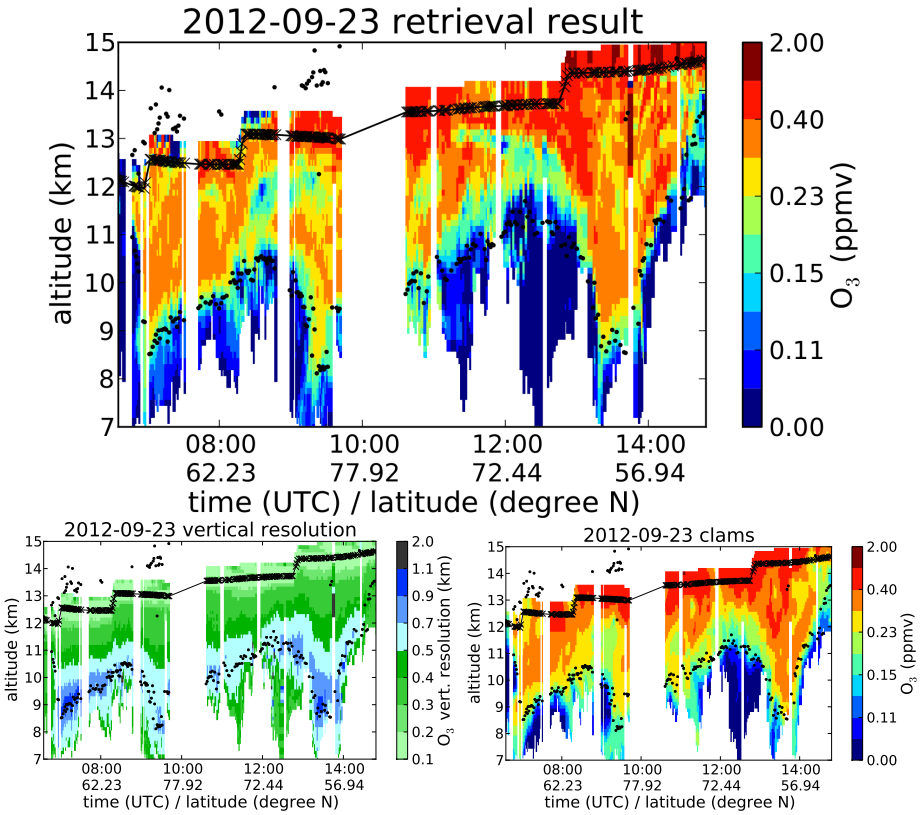

Figure 5.5.: *ESMVal Flight 18 2012-09-23 Ozone*

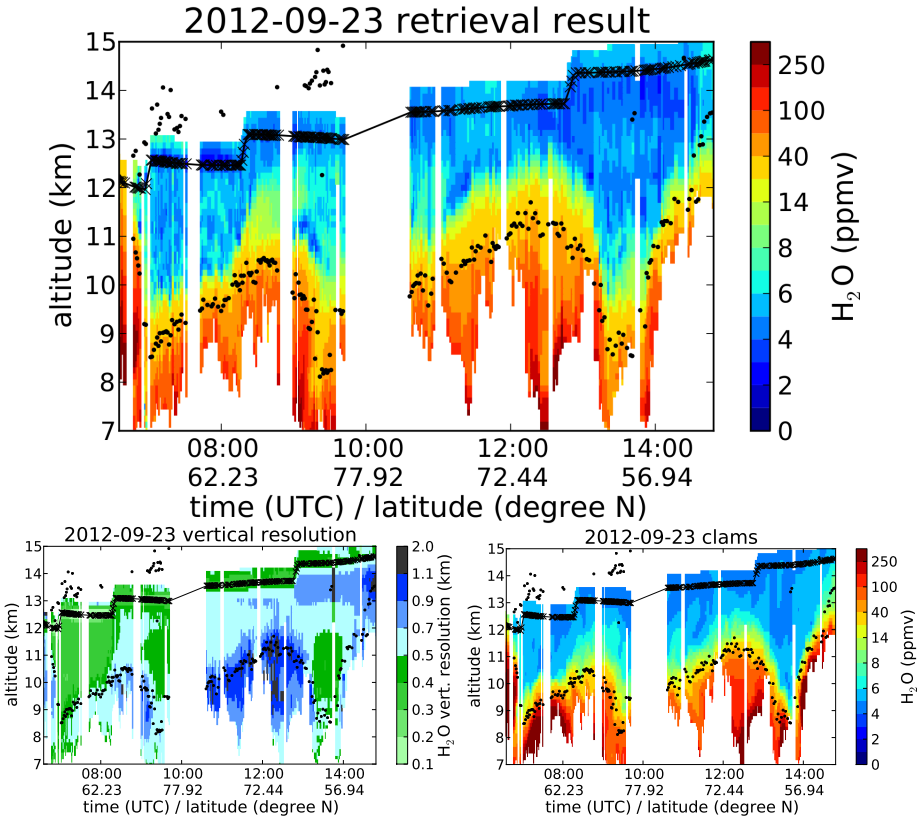

Figure 5.6.: *ESMVal Flight 18 2012-09-23 Water Vapour*

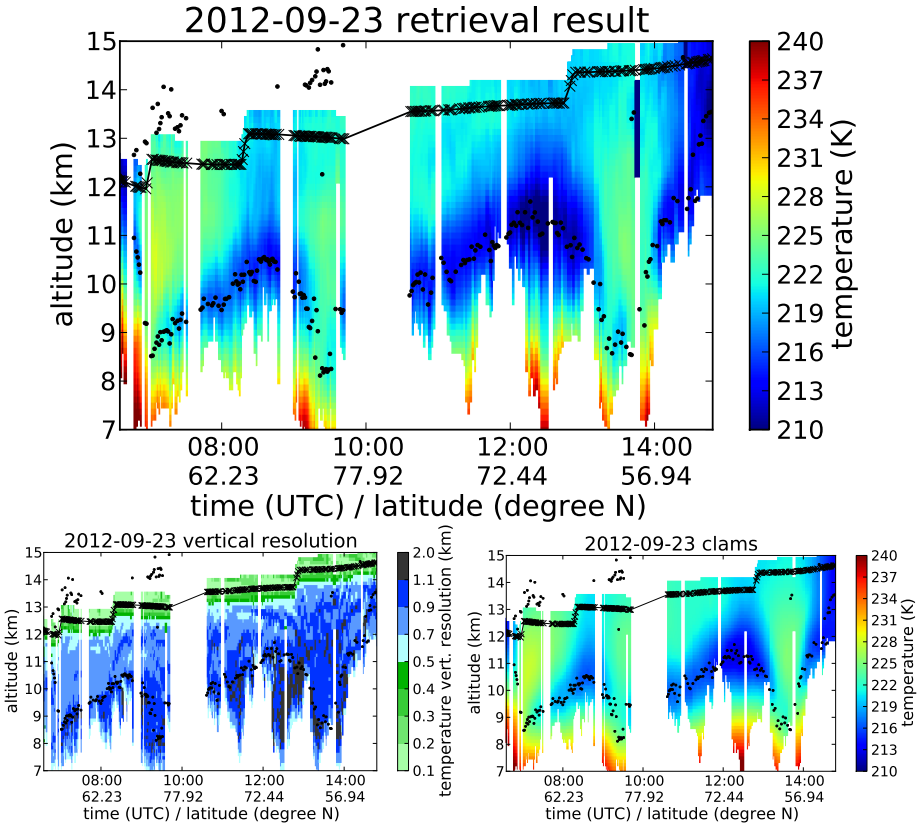

Figure 5.7.: *ESMVal Flight 18 2012-09-23 Temperature*

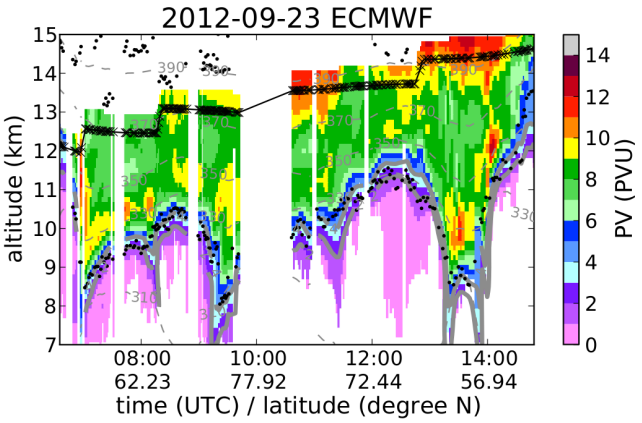

Figure 5.8.: *ECMWF PV values interpolated onto the GLORIA retrieval grid for comparison with the Level-2 results.*

11:30 UTC (region B), within an altitude range between 10 and 13 km. The 96-hour calculations place the origin of these low-HNO_3 air masses within the mid-latitude region over North America, consistent with the hypothesis that the anticyclone was formed by tropospheric air transported in an eddy broken off in this region.

Generally, the backwards trajectories lend support to the interpretation formed after comparison of the retrieval results with ECMWF PV data. However, it should be noted that this method has its limitations. The calculations performed here are limited to advection, i.e. mixing of air parcels is not simulated. This may be one reason why not all of the trajectories behave in the expected manner: some of the low-HNO_3 measurements are traced back to the polar regions, and the high-HNO_3 filament within the anticyclone are not. So while the trajectories clearly indicate an influx of mid-latitude and polar air into GLORIA's target volumes, consistent with the observations, it is generally not possible to confidently trace back individual small-scale structures using this method alone.

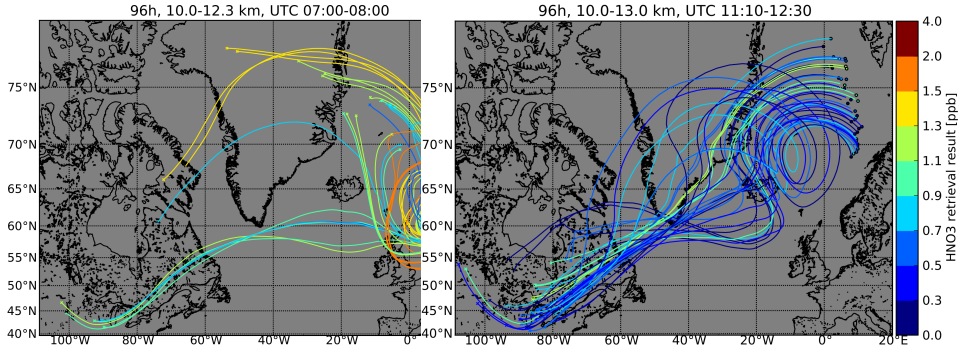

(a) *northbound leg cyclone* ***(b)*** *southbound leg anticyclone*

Figure 5.9.: *96-hour backwards trajectory calculations performed with the CLaMS* traj *tool. The trajectories were initialised at GLORIA retrieval grid points; the colour of each trajectory corresponds to the retrieved volume mixing ratio at these points. Figure a) shows the high-PV cyclone with measurements from the northbound leg of Flight 18. Figure b) shows the anticyclone during the southbound leg.*

Example Profile

Figures 5.10 and 5.11 show the results for a single measurement, together with their respective five leading sources of error. The profile was recorded at 11:10:02 UTC, with tangent points along a line of sight between 77.8°–79.3° N and 2.4° W–13.1° E. The retrieved values for O_3, H_2O and especially HNO_3 are in very good agreement with the CLaMS simulation above the tropopause, but O_3 and HNO_3 in particular show some small-scale structures that CLaMS does not.

Comparisons of the first GLORIA data from the ESSenCe campaign with CLaMS performed by Blank (2014) have already demonstrated that GLORIA can resolve filamentary structures in the UTLS that CLaMS cannot accurately model. Small-scale disagreements such as the ones seen for HNO_3 and O_3 are therefore to be expected. Comparing the profiles in fig. 5.10 with the corresponding section of fig. 5.4 and 5.5, one

finds that the retrieved profiles are slightly enhanced relative to CLaMS between 11 and 13 km altitude. At the tropopause level, the GLORIA measurements are instead markedly lower than the simulated values. Although CLaMS sees the same stratospheric filament in HNO_3 and O_3, the scene portrayed by GLORIA shows a more defined structure.

The results for temperature also show the largest differences at the tropopause level, with a temperature difference of 3 K to CLaMS. A possible explanation for the disagreements between the retrieved profiles and CLaMS at the tropopause is a still unaccounted for elevation error. All targets are sensitive to elevation uncertainties, especially at altitudes with steep gradients, such as the tropopause. However, more studies will be necessary to ascertain the source of these differences and whether it lies with GLORIA or the model data.

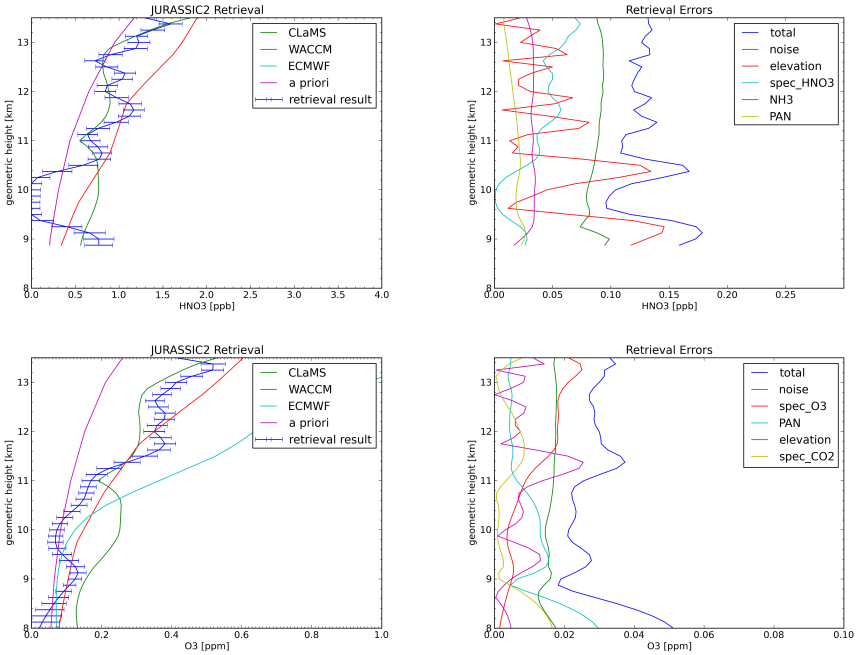

Figure 5.10.: *Retrieval results and error contributions for a single profile, measured at 11:10:02 UTC. Nitric acid and ozone are in good agreement with CLaMS calculations. Noise, elevation and PAN are leading sources of uncertainty for both gases.* HNO_3 *is also sensitive to uncertainties in the assumed volume mixing ratio of ammonia (*NH_3*) and in its own emission characteristics.* O_3 *is sensitive to errors both in its own spectroscopic data as well as that of* CO_2*.*

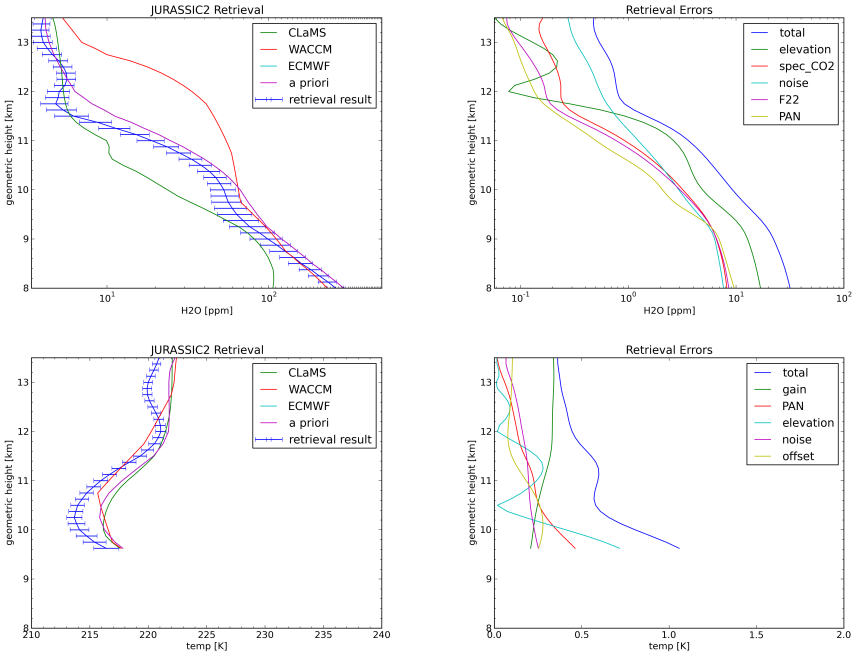

Figure 5.11.: *Additional retrieval results for water vapour (H_2O) and temperature. Water vapour has been plotted on a logarithmic axis for better visibility of the small stratosopheric values in the order of several ppm. Leading errors for both again include noise and elevation. H_2O is also sensitive to errors in NH_3 and HCFC-22 volume mixing ratios, as well as spectroscopic CO_2 errors. The temperature retrieval is sensitive to calibration errors, especially uncertainties in the radiometric gain function, but also to offset errors. PAN volume mixing ratios are an additional source of error for the temperature profile.*

6. Conclusions and Outlook

The GLORIA limb imager is a technologically ambitious project spearheading a new generation of infrared remote sensing instruments. Its combination of high spatial and spectral resolution provides entirely new avenues for the study of UTLS composition and exchange processes. However, such an instrument can only be scientifically exploited when the software used to process the measurements enables rapid data analysis and iterative improvements to quality.

The work presented here achieved two principal goals. With *gloripy*, a new comprehensive framework for the processing of GLORIA data was designed and implemented. The *gloripy* software marks a paradigm shift in that it integrates many traditionally separate aspects of the processing, specifically the Level-0 and Level-1 processors. This new degree of interoperability, ease of use and efficiency enabled the timely availability of first calibrated data for the TACTS/ESMVal measurements recorded by GLORIA. Immediately afterward, first Level-2 results could be produced. Although preliminary at first, these early trace gas retrievals proved invaluable for two reasons. Firstly, they served as a "quick view" of the observed meteorological situations, which helped prioritise further processing and enabled a first exchange with other instrument teams. Secondly, the Level-2 data themselves gave vital information on the quality of the calibrated spectra. For instance, the inclusion of faulty pixels or just too much noise in the radiometric offset would cause artifacts (cf. fig. 4.4). These artifacts could be mistaken for atmospheric features if evaluated only on a single profile. As *gloripy* enabled the processing of hundreds of profiles in just a few hours, calibrations could be tested on cross-sections along whole flights, where the horizontal correlation

of the artifacts would indicate their presence. The short development and testing cycle would then allow for quick experimentation with new calibration methods, culminating in the novel techniques presented in section 4.3.

The second goal was to apply this new processing chain to GLORIA data from the TACTS/ESMVal measurement campaign and demonstrate GLORIA's exceptional suitability for the study of UTLS dynamics. Selected measurements from a flight into the northern polar regions in September of 2012 were processed and the volume mixing ratios of trace gases were successfully retrieved from the calibrated spectra using the JURASSIC2 Level-2 processor. The distribution of stratospheric tracers, especially HNO_3, showed a highly inhomogeneous lower stratosphere. Comparisons with ECMWF potential vorticity data suggests that the synoptic situation was dominated by the remnants of a mid-latitude Rossby wave breaking event that took place 3-4 days prior. This is consistent with GLORIA observations of relatively low, more tropospheric HNO_3 mixing ratios in the lower stratosphere within this region. Presumably in tandem with this anticyclone in the North, a vertically localised cyclone of high-PV air was formed in the southern part of the measured area was formed. This, too, could be shown to be consistent with GLORIA observations showing a region of HNO_3- and O_3-rich, stratospheric air, bordered from above by air with low concentrations of the stratospheric tracers. Complementary trajectory calculations add further support to the view that these structures are caused by tropospheric air being transported into the polar stratosphere. Comparisons with CLaMS model calculations show GLORIA observations to be in generally very good agreement, although the details of some of the observed structures and the absolute values of volume mixing ratios differ between model and measurement, especially in the vicinity of the tropopause.

Although the data presented here already show the scientific potential of GLORIA and the TACTS/ESMVal data set, work on all stages of data processing and on the instrument characterisation is still in progress.

Future data versions will enable the retrieval of more trace species, such as CFC-11. Now that the groundwork has been laid, the full potential of GLORIA can begin to be exploited. The results presented in this work were based on a limited selection of measurements and strictly one-dimensional retrievals of vertical profiles. Horizontal regularisation of GLORIA measurements (Ungermann, 2013) can be expected to lead to further improvements in vertical resolution. Even more promising is the prospect of 3D-tomographic retrievals, utilising the full range of dynamics mode measurements. For a closed flight pattern, the very first tomographic results with unprecedented horizontal resolution could already be produced by Blank (2014). Without these flight patterns, linear flight tomography can be attempted to improve spatial resolution and mitigate the traditional weakness of the limb geometry against gradients along the line of sight. Flight 18, performed on September 23rd, 2012, and presented in this work, is certainly among the first candidates for an application of this technique.

Another prospect, for data quality assurance as well as a scientific topic in its own right, is the improvement of the currently used cloud detection method. Avenues for improvement here are using less conservative filters to obtain more trace gas information, and trying to study clouds themselves using more sophisticated methods, such as e.g. the studies performed on CRISTA-NF measurements in the past by Spang et al. (2008). These developments are essential and can be expected to be at least partially transferable to later balloon or satellite instruments similar to GLORIA.

Appendices

A. Level-0 algorithms

Modern compilers can usually be assumed to produce very efficient machine code. This is true especially for languages like C, C++ and Fotran which are extensively used for numerical calculations. However, in some cases, manual optimisation of critical operations can still significantly increase runtime performance.

Computer CPUs commonly incorporate an SIMD[1] instruction set and corresponding registers which are optimised for vectorised computations. For instance, *Intel x86* compatible CPUs define and implement various versions of the *SSE*[2] instruction set (see Intel Corporation, 2013, for reference).

While compilers such as GCC are able to make use of these instructions, they cannot do so as aggressively as a human programmer simply because they lack comprehensive knowledge about the problem the code is supposed to solve. For the GLORIA data processing chain, SSE instructions could be used to improve the performance of some of the processing steps. The two with the most impact are described in this chapter.

A.1. Cuboid Transposition

As has been explained in chapter 4.1, the Level-0 processor has to transpose the raw CUB data as the first processing step. The straightforward implementation of the transposition is just a double loop:

[1] single-instruction, multiple data
[2] *Streaming SIMD Extensions*

```
for i in range(n):
  for j in range(m):
      transposed_data[i, j] = orig_data[j, i]
```

This process can be trivially parallelised by partitioning the n rows which are then transposed by parallel threads. However, each thread still processes only a single CUB value at once.

The CUB values are *words*, i.e. 16-bit integers. Modern CPUs usually employ general-purpose registers of *quadword* width which can store 64 bit values. Additionally, processors of the x86 family possess *vector registers* for use with the SSE instruction set. These registers are of *double quadword* width and can therefore hold 128 bits of information each. Moreover, they are specifically designed to operate on multiple values in parallel, e.g. add two pairs of 64-bit floating point values. These instructions include operations that interpret the register content as a vector of eight 16-bit values, i.e. a single vector register can hold eight CUB values at once.

Consider a *block matrix* $\mathbf{M}$ of the form

$$\mathbf{M} = \begin{pmatrix} \mathbf{A} & \mathbf{B} \\ \mathbf{C} & \mathbf{D} \end{pmatrix} \tag{A.1}$$

The transpose of this block matrix can be found by transposing the constituent blocks:

$$\mathbf{M}^T = \begin{pmatrix} \mathbf{A} & \mathbf{B} \\ \mathbf{C} & \mathbf{D} \end{pmatrix}^T = \begin{pmatrix} \mathbf{A}^T & \mathbf{C}^T \\ \mathbf{B}^T & \mathbf{D}^T \end{pmatrix} \tag{A.2}$$

This means that the CUB data can be transposed by first dividing the whole CUB into a number of blocks, then transposing the blocks and storing them in the correct location within the result. As the SSE registers can hold 8 CUB values each, it is efficient and convenient to treat the CUB as a block matrix consisting of a number of 8x8 blocks.

Eight values can be now be read from memory at a time instead of just one. After eight load operations, a single 8x8 block comprised of 64 CUB values has been fully loaded. The transpose of the block is calculated completely inside the CPU using *parallel unpack* instructions and then written to the correct location in memory, again storing eight values at once.

A.2. Fast Vectorised Convolution

Section 4.1.2 describes how the Level-0 processor performs the resampling of interferograms from the time domain into the spatial domain. The resampling is achieved by convolving the measured values with a sinc-function. The values of this window function are reduced to a finite-length pre-tabulated kernel. Effectively, this means that each point of the result is obtained from a standard scalar product (cf. eq. 4.8). Many modern processors implement special instructions that allow for the fast evaluation of such products. For the GLORIA Level-0 processor, the SSE instruction set's *multiply-and-add* operation was used to significantly enhance performance.

The algorithm assumes that the pre-tabulated kernel is exactly 16 elements wide, with each element being represented by a signed 16-bit integer. Using only two *load* operations, one kernel can be loaded into the CPU's SSE vector registers. The same is done with the 16 interferogram values, represented by unsigned 16-bit integers.

After the *load* operations, two registers hold 8 values of the kernel each, while another two registers hold the interferogram values. Using the *multiply-and-add* instruction twice produces 2×4 signed 32-bit values. These are then added together and subjected to appropriate conversions to produce the final result as a signed 64-bit integer.

B. Mathematical References

B.1. Discrete Fourier Transforms

Due to GLORIA being an FTS, large parts of the data processing revolves around the discrete Fourier tansform (DFTs) and their properties. This chapter is intended as a reference for the most important relations.

B.1.1. Definition and Basic Properties

Let $(x_n)_{n\in\{0,\dots,N-1\}} \subset \mathbb{C}$ be an arbitary series of complex numbers. The DFT of (x_n) is defined as the sequence $(\tilde{x}_k)_{k\in\{0,\dots,N-1\}}$, with

$$\tilde{x}_k = \sum_{n=0}^{N-1} \mathrm{e}^{-2\pi i \frac{kn}{N}} x_n \tag{B.1}$$

Conversely, the *inverse* DFT of (x_n) is defined as

$$\hat{x}_l = \frac{1}{N} \sum_{n=0}^{N-1} \mathrm{e}^{2\pi i \frac{ln}{N}} x_n \tag{B.2}$$

and is, in fact, the inverse mapping of the DFT:

$$\hat{\tilde{x}}_n = x_n \tag{B.3}$$

Like its continuous counterpart, the DFT is *linear*. Let (x_n) and (y_n) be complex sequences, and let $\alpha \in \mathbb{C}$ be an arbitary number. Then the

DFT of the liner combination is the linear combination of DFTs:

$$\widetilde{(\alpha x + y)}_k = \alpha \tilde{x}_k + \tilde{y}_k \tag{B.4}$$

An important property of the DFT is the *convolution theorem*. For two sequences (x_n) and (y_n), the DFT of their convolution is the product of their respective DFTs:

$$\widetilde{(x * y)}_k = \tilde{x}_k \tilde{y}_k \tag{B.5}$$

This relation is important because the computational complexity of convolving two arrays of length N is $\mathcal{O}\left(N^2\right)$, whereas the multiplication is merely $\mathcal{O}\left(N\right)$.

B.1.2. Real-Valued Input

The case of a DFT of a real-valued input sequence is particularly interesting for many applications, including GLORIA analysis. In this special case, the DFT has a useful property. Let $(x_n) \subset \mathbb{R}$ now be a real-valued series of length N, and let $(\tilde{x}_n)$ be its DFT. Then it follows

for all $k \in 0, \ldots, N-1$:

$$\tilde{x}_{N-k} = \sum_{n=0}^{N-1} x_n \mathrm{e}^{-2\pi i \frac{(N-k)n}{N}} \tag{B.6}$$

$$= \sum_{n=0}^{N-1} x_n \mathrm{e}^{-2\pi i n} \mathrm{e}^{2\pi i \frac{kn}{N}} \tag{B.7}$$

$$= \sum_{n=0}^{N-1} 1 \cdot x_n \mathrm{e}^{2\pi i \frac{kn}{N}} \tag{B.8}$$

$$= \sum_{n=0}^{N-1} \left(x_n \mathrm{e}^{-2\pi i \frac{kn}{N}} \right)^* \tag{B.9}$$

$$= \tilde{x}_k^* \tag{B.10}$$

This means that the DFT of a real-valued series exhibits *Hermitian symmetry*. If N is even, then

$$\tilde{x}_{N/2+k} = \tilde{x}_{N-N/2+k} = \tilde{x}_{N/2-k}^* \tag{B.11}$$

i.e. the symmetry axis is between $\tilde{x}_{N/2}$ and $\tilde{x}_{N/2+1}$. If N is odd, then

$$N - (N+1)/2 = N + 1 - (N+1)/2 - 1 = (N+1)/2 - 1 \tag{B.12}$$

$$\tilde{x}_{(N+1)/2+k} = \tilde{x}_{N-(N+1)/2-k} = \tilde{x}_{(N+1)/2-1-k}^* \tag{B.13}$$

i.e. in this case, the symmetry axis is $\tilde{x}_{(N+1)/2} \in \mathbb{R}$. In both cases, given N, the series can be reconstructed completely with knowledge of only the first $[N/2] + 1$ elements simply by complex conjugation. The remaining elements do not carry any additional information. For this reason, specialised DFT algorithms (e.g. RFFT) exist for real-valued inputs which, in addition to using real instead of complex multiplication, reduce the computing effort and memory usage by only calculating the first $[N/2] + 1$ elements. These algorithms are commonly used when the

terms "DFT" or "FFT" are employed in practice.

B.1.3. Linear Phase Components and Interferogram Shifts

Let (x_n) be a sequence (with periodic boundaries) of real numbers with $n \in [0, \ldots, N-1]$ and $(\tilde{x}_k) = (r_k \exp i\phi_k)$ its discrete Fourier transform. Consider the *shifted* sequence $(x'_n) = (x_{n-s})$. The original series can be recovered using the inverse transform (see eq. (B.2)):

$$x_n = \frac{1}{N} \sum_k e^{2\pi i \frac{kn}{N}} \tilde{x}_k \tag{B.14}$$

It follows for the shifted sequence:

$$x'_n = \frac{1}{N} \sum_k e^{2\pi i \frac{k(n-s)}{N}} \tilde{x}_k \tag{B.15}$$

$$= \frac{1}{N} \sum_k e^{2\pi i \frac{kn}{N}} r_k e^{i\phi_k} e^{-2\pi i \frac{ks}{N}} \tag{B.16}$$

$$= \frac{1}{N} \sum_k e^{2\pi i \frac{kn}{N}} \tilde{x}'_k \tag{B.17}$$

Note that the newly introduced $(\tilde{x}'_k)$ is the discrete Fourier transform of the shifted sequence (x'_n). For the phase of $\tilde{x}'_k$, it follows

$$\phi'_k = -2\pi \frac{s}{N} \cdot k + \phi_k \tag{B.18}$$

i.e. the phase of the shifted sequence's Fourier transform is the original phase with an additive term linear in k. Conversely, from the slope α of a linear phase term, the shift s can be computed:

$$s = -\frac{N\alpha}{2\pi} \tag{B.19}$$

Generalised to the case of non-discrete shifts σ, this becomes:

$$\sigma = -\frac{N\alpha}{2\pi}\Delta x \tag{B.20}$$

where Δx is the sampling distance of (x_n).

Danksagungen

In den etwas mehr als drei Jahren des Weges hin zu dieser Arbeit wurde ich von vielen Menschen begleitet und unterstützt, denen ich an dieser Stelle meinen Dank aussprechen möchte.

Zunächst möchte ich mich bei meinem Doktorvater, Herrn Professor Martin Riese, bedanken, der meine Arbeit stets unterstützt und mir die Teilnahme an zwei GLORIA-Messkampagnen sowie mehreren internationalen Konferenzen ermöglicht hat. Direkt im Anschluss sind meine beiden Betreuer, Martin Kaufmann und Peter Preuße, zu nennen, die besonders durch zahlreiche wertvolle Anregungen und Kommentare zum Erfolg des Projektes beigetragen haben.

Meinen beiden Mitarbeitern aus dem GLORIA-Retrieval-Team am IEK-7, Jörg Blank und Jörn Ungermann, möchte ich für die jahrelange gute Zusammenarbeit danken. Besonders von ihrer Erfahrung im Bereich der Softwareentwicklung, aber auch in der mir zu Anfang noch fremden Methodik der Fernerkundung, konnte ich in den letzten Jahren vielfach profitieren. Bärbel Vogel und Jens-Uwe Grooß haben mit bereitgestellten CLaMS-Daten und damit verbundener Expertise sehr zur Auswertung und Interpretation der GLORIA-Messergebnisse beigetragen. Auch bei den übrigen Mitarbeitern aus dem IEK-7 möchte ich mich für anregende Diskussionen und ein angenehmes Arbeitsklima bedanken.

Bei meiner Arbeit wurde ich nicht nur durch meine Institutskollegen, sondern auch vom übrigen GLORIA-Team unterstützt: Norbert Bayer, Robin Dapp, Andreas Ebersoldt, Herbert Fischer, Felix Friedl-Vallon, Friederike Graf, Thomas Gulde, Frank Hase, Michael Höpfner, Anne Kleinert, Erik Kretschmer, Thomas Kulessa, Thomas Latzko, Guido Maucher, Tom Neubert, Hans Nordmeyer, Hermann Oelhaf, Friedhelm Olschewski, Johannes Orphal, Christoph Piesch, Heinz Rongen, Christian Sartorius, Georg Schardt, Johan Schillings, Herbert Schneider, Axel

Schönfeld, Mahesh Kumar Sha, Olga Sumińska-Ebersoldt und Vicheith Tan. Besonders hervorzuheben sind Anne Kleinert und Felix Friedl-Vallon vom Karlsruher Institut für Technologie, auf deren umfangreiches Wissen zu Instrumenteneffekten, Signalverarbeitung und zur radiometrischen Kalibration ich stets zurückgreifen konnte. Zum Level-0-Prozessor wurde von Anne Kleinert, Tom Neubert und Ricardo Ribalda umfangreiche Vorarbeit geleistet, auf der ich bei der *gloripy*-Entwicklung aufbauen konnte.

Charlotte und Michael Hoppe sowie Hendrik Elbern danke ich für die Fahrgemeinschaft, die das tägliche Pendeln von Köln bzw. Hürth nach Jülich sowohl wirtschaftlicher als auch erheblich unterhaltsamer gemacht hat.

Meinem Bürogenossen Silvio Kalisch bin ich zu Dank verpflichtet für diverse anregende Gespräche und insbesondere für die Tolerierung meines lautstarken Tastenanschlags in den letzten Monaten.

Meinen Eltern Annelie Kahlert-Guggenmoser und Franz-Josef Guggenmoser danke ich für ihre Unterstützung; gleiches gilt auch für meine langjährigen Freunde Kay, Christiane, Florian, Malte und Fabian.

Bibliography

Beer, R. (1992). *Remote sensing by Fourier transform spectrometry*, volume 170. Wiley-Interscience.

Blank, J. (2014). *Tomographic retrieval of trace gases observed by GLORIA*. PhD thesis, Bergische Universität Wuppertal. to be published.

Brault, J. W. (1996). New approach to high-precision Fourier transform spectrometer design. *Appl. Optics*, 35(16):2891–2896.

Curtis, A. R. (1952). Discussion of 'A statistical model for water vapour absorption' by R. M. Goody. *Quart. J. Roy. Meteorol. Soc.*, 78:638–640.

Einstein, A. (1905). Zur Elektrodynamik bewegter Körper. *Ann. Phys. (Berlin)*, 322(10):891–921.

ESA (2012). *Report for Mission Selection: PREMIER*, volume 3 of *ESA SP-1324*. European Space Agency, Noordwijk, The Netherlands.

Fischer, H., Birk, M., Blom, C., Carli, B., Carlotti, M., von Clarmann, T., Delbouille, L., Dudhia, A., Ehhalt, D., Endemann, M., Flaud, J. M., Gessner, R., Kleinert, A., Koopman, R., Langen, J., López-Puertas, M., Mosner, P., Nett, H., Oelhaf, H., Perron, G., Remedios, J., Ridolfi, M., Stiller, G., and Zander, R. (2008). MIPAS: an instrument for atmospheric and climate research. *Atmos. Chem. Phys.*, 8(8):2151–2188.

Fischer, H., Wienhold, F., Hoor, P., Bujok, O., Schiller, C., Siegmund, P., Ambaum, M., Scheeren, H., and Lelieveld, J. (2000). Tracer correlations in the northern high latitude lowermost stratosphere: Influence of cross-tropopause mass exchange. *Geophys. Res. Lett.*, 27(1):97–100.

Friedl-Vallon, F., Maucher, G., Seefeldner, M., Trieschmann, O., Kleinert, A., Lengel, A., Keim, C., Oelhaf, H., and Fischer, H. (2004). Design and characterization of the balloon-borne Michelson Interferometer for Passive Atmospheric Sounding (MIPAS-B2). *Appl. Optics*, 43(16):3335–3355.

Friedl-Vallon, F., Riese, M., Maucher, G., Lengel, A., Hase, F., Preusse, P., and Spang, R. (2006). Instrument concept and preliminary performance analysis of GLORIA. *Adv. Space Res.*, 37:2287–2291.

Frigo, M. and Johnson, S. G. (1998). FFTW: An adaptive software architecture for the FFT. In *Proceedings of the 1998 IEEE International Conference on Acoustics, Speech and Signal Processing*, volume 3, pages 1381–1384.

Gettelman, A., Hoor, P., Pan, L., Randel, W., Hegglin, M., and Birner, T. (2011). The extratropical upper troposphere and lower stratosphere. *Rev. Geophys.*, 49(3):RG3003.

Godson, W. L. (1953). The evaluation of infra-red radiative fluxes due to atmospheric water vapour. *Quart. J. Roy. Meteorol. Soc.*, 79:367–379.

Gordley, L. L. and Russell, J. M. (1981). Rapid inversion of limb radiance data using an emissivity growth approximation. *Appl. Optics*, 20:807–813.

Griessbach, S., Hoffmann, L., Spang, R., and Riese, M. (2014). Volcanic ash detection with infrared limb sounding: MIPAS observations and radiative transfer simulations. *Atmos. Meas. Tech.*, 7(5):1487–1507.

Guggenmoser, T., Ungermann, J., Blank, J., Kleinert, A., Grooss, J.-U., and Vogel, B. (2013). Spatial structures in UTLS trace gases imaged by the GLORIA instrument during the TACTS/ESMVal campaign in 2012. In *EGU General Assembly Conference Abstracts*, volume 15, page 12239.

von Hobe, M., Bekki, S., Borrmann, S., Cairo, F., D'Amato, F., Di Donfrancesco, G., Dörnbrack, A., Ebersoldt, A., Ebert, M., Emde, C., Engel, I., Ern, M., Frey, W., Genco, S., Griessbach, S., Grooß, J.-U., Gulde, T., Günther, G., Hösen, E., Hoffmann, L., Homonnai, V., Hoyle, C. R., Isaksen, I. S. A., Jackson, D. R., Jánosi, I. M., Jones, R. L., Kandler, K., Kalicinsky, C., Keil, A., Khaykin, S. M., Khosrawi, F., Kivi, R., Kuttippurath, J., Laube, J. C., Lefèvre, F., Lehmann, R., Ludmann, S., Luo, B. P., Marchand, M., Meyer, J., Mitev, V., Molleker, S., Müller, R., Oelhaf, H., Olschewski, F., Orsolini, Y., Peter, T., Pfeilsticker, K., Piesch, C., Pitts, M. C., Poole, L. R., Pope, F. D., Ravegnani, F., Rex, M., Riese, M., Röckmann, T., Rognerud, B., Roiger, A., Rolf, C., Santee, M. L., Scheibe, M., Schiller, C., Schlager, H., Siciliani de Cumis, M., Sitnikov, N., Søvde, O. A., Spang, R., Spelten, N., Stordal, F., Sumińska-Ebersoldt, O., Ulanovski, A., Ungermann, J., Viciani, S., Volk, C. M., vom Scheidt, M., von der Gathen, P., Walker, K., Wegner, T., Weigel, R., Weinbruch, S., Wetzel, G., Wienhold, F. G., Wohltmann, I., Woiwode, W., Young, I. A. K., Yushkov, V., Zobrist, B., and Stroh, F. (2013). Reconciliation of essential process parameters for an enhanced predictability of arctic stratospheric ozone loss and its climate interactions (RECONCILE): activities and results. *Atmos. Chem. Phys.*, 13(18):9233–9268.

Hoffmann, L., Spang, R., Kaufmann, M., and Riese, M. (2005). Retrieval of CFC-11 and CFC-12 from Envisat MIPAS observations by means of rapid radiative transfer calculations. *Adv. Space Res.*, 36:915–921.

Holton, J. R., Haynes, P. H., McIntyre, M. E., Douglass, A. R., Rood,

R. B., and Pfister, L. (1995). Stratosphere-troposphere exchange. *Rev. Geophys.*, 33(4):403–439.

Höpfner, M., Stiller, G. P., Kuntz, M., von Clarmann, T., Echle, G., Funke, B., Glatthor, N., Hase, F., Kemnitzer, H., and Zorn, S. (1998). The Karlsruhe optimized and precise radiative transfer algorithm. Part II: Interface to retrieval applications. In Wang, J., Wu, B., Ogawa, T., and Guan, Z., editors, *Optical Remote Sensing of the Atmosphere and Clouds, Beijing, China, 15–17 September 1998*, volume 3501, pages 186–195.

Intel Corporation (2013). *Intel® 64 and IA-32 Architectures Software Developer's Manual*.

Kaufmann, M., Blank, J., Friedl-Vallon, F., Gerber, D., Guggenmoser, T., Hoepfner, M., Kleinert, A., Sha, M. K., Oelhaf, H., Riese, M., Suminska-Ebersoldt, O., and Woiwode, W. (2013). Technical assistance for the deployment of airborne limb sounders during ESSenCe, final report. Technical report, European Space Agency, Noordwijk, The Netherlands.

Kleinert, A. (2006). Correction of detector nonlinearity for the balloon-borne Michelson Interferometer for Passive Atmospheric Sounding. *Appl. Optics*, 45(3):425–431.

Kleinert, A., Aubertin, G., Perron, G., Birk, M., Wagner, G., Hase, F., Nett, H., and Poulin, R. (2007). MIPAS level 1B algorithms overview: operational processing and characterization. *Atmos. Chem. Phys.*, 7(5):1395–1406.

Kleinert, A., Friedl-Vallon, F., Guggenmoser, T., Höpfner, M., Neubert, T., Ribalda, R., Sha, M. K., Ungermann, J., Blank, J., Ebersoldt, A., Kretschmer, E., Latzko, T., Oelhaf, H., Olschewski, F., and Preusse, P. (2014). Level 0 to 1 processing of the imaging Fourier transform

spectrometer GLORIA: generation of radiometrically and spectrally calibrated spectra. *Atmos. Meas. Tech. Discuss.*, 7(3):2827–2878.

Kretschmer, E. (2014). *Modelling of the Instrument Spectral Response of Conventional and Imaging Fourier Transform Spectrometers*. PhD thesis, Université Laval.

Kretschmer, E., Dapp, R., Schardt, G., Gulde, T., Friedl-Vallon, F., Bachner, M., Guggenmoser, T., Hartmann, V., Maucher, G., Schmitt, C., Schönfeld, A., and Tan, V. (2014). In-flight control and communication of the GLORIA imaging limb-sounder on atmospheric research aircraft. *Atmos. Meas. Tech.* in preparation.

Marshall, B. T., Gordley, L. L., and Allen Chu, D. (1994). BANDPAK: Algorithms for modeling broadband transmission and radiance. *J. Quant. Spectrosc. Radiat. Transfer*, 52(5):581–599.

McKenna, D. S., Konopka, P., Grooß, J.-U., Günther, G., Müller, R., Spang, R., Offermann, D., and Orsolini, Y. (2002). A new Chemical Lagrangian Model of the Stratosphere (CLaMS) 1. Formulation of advection and mixing. *J. Geophys. Res.*, 107(D16):ACH 15–1–ACH 15–15.

Michelson, A. A. and Morley, E. W. (1887). On the Relative Motion of the Earth and of the Luminiferous Ether. *Am. Jour. Sci.*, XXXIV(203):333–345.

Monte, C., Gutschwager, B., Adibekyan, A., Kehrt, M., Ebersoldt, A., Olschewski, F., and Hollandt, J. (2013). Radiometric calibration of the in-flight blackbody calibration system of the GLORIA interferometer. *Atmos. Meas. Tech.*, 6:5251–5295.

Naylor, D. A. and Tahic, M. K. (2007). Apodizing functions for Fourier transform spectroscopy. *J. Opt. Soc. Am.*, 24(11):3644–3648.

Nocedal, J. and Wright, S. J. (1999). *Numerical Optimization*, volume 2. Springer New York.

Norton, R. H. and Beer, R. (1976). New apodizing functions for Fourier spectrometry. *J. Opt. Soc. Am.*, 66(3):259–264.

Oelhaf, H., Clarmann, T., Fischer, H., Friedl-Vallon, F., Fritzsche, C., Linden, A., Piesch, C., Seefeldner, M., and Völker, W. (1994). Stratospheric ClONO2 and HNO3 profiles inside the arctic vortex from MIPAS-B limb emission spectra obtained during EASOE. *Geophys. Res. Lett.*, 21(13):1263–1266.

Offermann, D., Grossmann, K.-U., Barthol, P., Knieling, P., Riese, M., and Trant, R. (1999). Cryogenic Infrared Spectrometers and Telescopes for the Atmosphere (CRISTA) experiment and middle atmosphere variability. *J. Geophys. Res.*, 104(D13):16311–16325.

Olschewski, F., Ebersoldt, A., Friedl-Vallon, F., Gutschwager, B., Hollandt, J., Kleinert, A., Monte, C., Piesch, C., Preusse, P., Rolf, C., Steffens, P., and Koppmann, R. (2013). The in-flight blackbody calibration system for the GLORIA interferometer on board an airborne research platform. *Atmos. Meas. Tech.*, 6(11):3067–3082.

Petty, G. W. (2006). *A First Course in Atmospheric Radiation*. Sundog Publishing, Madison, Wi., USA.

Preusse, P., Schroeder, S., Hoffmann, L., Ern, M., Friedl-Vallon, F., Ungermann, J., Oelhaf, H., Fischer, H., and Riese, M. (2009). New perspectives on gravity wave remote sensing by spaceborne infrared limb imaging. *Atmos. Meas. Tech.*, 2(1):299–311.

Remedios, J. J. (1999). Extreme atmospheric constituent profiles for MIPAS. In *Proceedings of the European Symposium on atmospheric measurements from space*, volume 2, pages 779–783.

Revercomb, H. E., Buijs, H., Howell, H. B., LaPorte, D. D., Smith, W. L., and Sromovsky, L. (1988). Radiometric calibration of IR Fourier transform spectrometers: solution to a problem with the High-Resolution Interferometer Sounder. *Appl. Optics*, 27(15):3210–3218.

Riese, M., Friedl-Vallon, F., Spang, R., Preusse, P., Schiller, C., Hoffmann, L., Konopka, P., Oelhaf, H., von Clarmann, T., and Höpfner, M. (2005). GLObal limb Radiance Imager for the Atmosphere (GLORIA): Scientific objectives. *Adv. Space Res.*, 36:989–995.

Riese, M., Küll, V., Tie, X., Brasseur, G., Offermann, D., Lehmacher, G., and Franzen, A. (2000). Modeling of nitrogen species measured by CRISTA. *Geophys. Res. Lett.*, 27:2221–2224.

Riese, M., Manney, G. L., Oberheide, J., Tie, X., Spang, R., and Küll, V. (2002). Stratospheric transport by planetary wave mixing as observed during CRISTA-2. *J. Geophys. Res.*, 107(D23):8179.

Riese, M., Ploeger, F., Rap, A., Vogel, B., Konopka, P., Dameris, M., and Forster, P. (2012). Impact of uncertainties in atmospheric mixing on simulated UTLS composition and related radiative effects. *J. Geophys. Res.*, 117(D16).

Riese, M., Preusse, P., Spang, R., Ern, M., Jarisch, M., Grossmann, U., and Offermann, D. (1997). Measurements of trace gases by the Cryogenic Infrared Spectrometers and Telescopes for the Atmosphere (CRISTA) experiment. *Adv. Space Res.*, 19:563–566.

Riese, M., Spang, R., Preusse, P., Ern, M., Jarisch, M., Offermann, D., and Grossmann, K. U. (1999a). Cryogenic Infrared Spectrometers and Telescopes for the Atmosphere (CRISTA) data processing and atmospheric temperature and trace gas retrieval. *J. Geophys. Res.*, 104:16349–16367.

Riese, M., Tie, X., Brasseur, G., and Offermann, D. (1999b). Three-dimensional simulation of stratospheric trace gas distributions measured by CRISTA. *J. Geophys. Res.*, 104:16419–16435.

Rodgers, C. D. (2000). *Inverse Methods for Atmospheric Sounding – Theory and Practice*, volume 2 of *Series on Atmopsheric, Oceanic and Planetary Physics*. World Scientific Publishing Co. Pte. Ltd., Singapore.

Roedel, W. and Wagner, T. (2011). *Physik unserer Umwelt: Die Atmosphäre*. Springer, Berlin, 4th edition.

Rothman, L., Gordon, I., Barbe, A., Benner, D., Bernath, P., Birk, M., Boudon, V., Brown, L., Campargue, A., Champion, J.-P., Chance, K., Coudert, L., Dana, V., Devi, V., Fally, S., Flaud, J.-M., Gamache, R., Goldman, A., Jacquemart, D., Kleiner, I., Lacome, N., Lafferty, W., Mandin, J.-Y., Massie, S., Mikhailenko, S., Miller, C., Moazzen-Ahmadi, N., Naumenko, O., Nikitin, A., Orphal, J., Perevalov, V., Perrin, A., Predoi-Cross, A., Rinsland, C., Rotger, M., Šimečková, M., Smith, M., Sung, K., Tashkun, S., Tennyson, J., Toth, R., Vandaele, A., and Auwera, J. V. (2009). The HITRAN 2008 molecular spectroscopic database. *Journal of Quantitative Spectroscopy and Radiative Transfer*, 110(9–10):533–572.

Schwarzschild, K. (1914). Über Diffusion und Absorption in der Sonnenatmosphäre. In *Sitzber. Kgl. Preuss. Ak. Wiss.*, volume LXVII, pages 1183–1200.

Schwarzschild, K. (1916). Über das Gravitationsfeld eines Massenpunktes nach der Einsteinschen Theorie. In *Sitzber. Kgl. Preuss. Ak. Wiss.*, pages 189–196. From the session on February 3rd, 1916.

Shannon, C. E. (1948). A mathematical theory of communication. *Bell System Technical Journal*, 27:379–423, 623–656.

Shannon, C. E. (1949). Communication in the presence of noise. *Proceedings of the IRE*, 37(1):10–21.

Solomon, S., Qin, D., Manning, M., Alley, R., Berntsen, T., Bindoff, N., Chen, Z., Chidthaisong, A., Gregory, J., Hegerl, G., Heimann, M., Hewitson, B., Hoskins, B., Joos, F., Jouzel, J., Kattsov, V., Lohmann, U., Matsuno, T., Molina, M., Nicholls, N., J.Overpeck, Raga, G., Ramaswamy, V., Ren, J., Rusticucci, M., Somerville, R., Stocker, T., Whetton, P., Wood, R. A., and Wratt, D. (2007). *Climate Change 2007 - The Physical Science Basis. Contribution of Working Group I to the Fourth Assessment Report of the Intergovernmental Panel on Climate Change*, chapter Technical Summary. Cambridge University Press, Cambridge, United Kingdom and New York, NY, USA.

Spang, R., Eidmann, G., Riese, M., Offermann, D., Preusse, P., Pfister, L., and Wang, P.-H. (2002). CRISTA observations of cirrus clouds around the tropopause. *J. Geophys. Res.*, 107:CRI 2–1–CRI 2–18.

Spang, R., Hoffmann, L., Kullmann, A., Olschewski, F., Preusse, P., Knieling, P., Schroeder, S., Stroh, F., Weigel, K., and Riese, M. (2008). High resolution limb observations of clouds by the CRISTA-NF experiment during the SCOUT-O3 tropical aircraft campaign. *Adv. Space Res.*, 42(10):1765–1775.

Spang, R., Remedios, J., and Barkley, M. (2004). Colour indices for the detection and differentiation of cloud types in infra-red limb emission spectra. *Adv. Space Res.*, 33(7):1041–1047.

Steck, T. and von Clarmann, T. (2001). Constrained profile retrieval applied to the observation mode of the Michelson Interferometer for Passive Atmospheric Sounding. *Appl. Optics*, 40:3559–3571.

Stiller, G. P., editor (2000). *The Karlsruhe Optimized and Precise Radiative Transfer Algorithm (KOPRA)*, volume 6487 of *Wissenschaftliche*

Berichte des Forschungszentrums Karlsruhe. Forschungszentrum Karlsruhe, Karlsruhe.

Suminska-Ebersoldt, O. (2013). First retrieval results of the GLORIA chemistry mode measurements. In *EGU General Assembly Conference Abstracts*, volume 15, page 8901.

Tikhonov, A. N. and Arsenin, V. Y. (1977). *Solutions of ill-posed problems*. Winston, Washington D.C.

Trieschmann, O. (2000). *Phasenkorrektur und Radiometrie gekühlter Fourierspektrometer: Charakterisierung des Instrumentes MIPAS-B2*. PhD thesis, Universität Karlsruhe (TH).

Twomey, S. (1977). *Introduction to the Mathematics of Inversion in Remote Sensing and Indirect Measurements*, volume 3 of *Developments in Geomathematics*. Elsevier, Amsterdam.

Ungermann, J. (2011). *Tomographic reconstruction of atmospheric volumes from infrared limb-imager measurements*, volume 106 of *Schriften des Forschungszentrums Jülich, Reihe Energie und Umwelt*. Forschungszentrum Jülich GmbH, Jülich.

Ungermann, J. (2013). Improving retrieval quality for airborne limb sounders by horizontal regularisation. *Atmos. Meas. Tech.*, 6(1):15–32.

Ungermann, J., Blank, J., Lotz, J., Leppkes, K., Hoffmann, L., Guggenmoser, T., Kaufmann, M., Preusse, P., Naumann, U., and Riese, M. (2011). A 3-D tomographic retrieval approach with advection compensation for the air-borne limb-imager GLORIA. *Atmos. Meas. Tech.*, 4(11):2509–2529.

Ungermann, J., Hoffmann, L., Preusse, P., Kaufmann, M., and Riese, M. (2010a). Tomographic retrieval approach for mesoscale gravity

wave observations by the PREMIER infrared limb-sounder. *Atmos. Meas. Tech.*, 3(2):339–354.

Ungermann, J., Kalicinsky, C., Olschewski, F., Knieling, P., Hoffmann, L., Blank, J., Woiwode, W., Oelhaf, H., Hösen, E., Volk, C., et al. (2012). CRISTA-NF measurements with unprecedented vertical resolution during the RECONCILE aircraft campaign. *Atmos. Meas. Tech.*, 5(5):1173–1191.

Ungermann, J., Kaufmann, M., Hoffmann, L., Preusse, P., Oelhaf, H., Friedl-Vallon, F., and Riese, M. (2010b). Towards a 3-D tomographic retrieval for the air-borne limb-imager GLORIA. *Atmos. Meas. Tech.*, 3(6):1647–1665.

Ungermann, J., Pan, L. L., Kalicinsky, C., Olschewski, F., Knieling, P., Blank, J., Weigel, K., Guggenmoser, T., Stroh, F., Hoffmann, L., and Riese, M. (2013). Filamentary structure in chemical tracer distributions near the subtropical jet following a wave breaking event. *Atmos. Chem. Phys.*, 13(20):10517–10534.

Woiwode, W., Oelhaf, H., Gulde, T., Piesch, C., Maucher, G., Ebersoldt, A., Keim, C., Höpfner, M., Khaykin, S., Ravegnani, F., et al. (2012). MIPAS-STR measurements in the Arctic UTLS in winter/spring 2010: instrument characterization, retrieval and validation. *Atmos. Meas. Tech.*, 5(6):1205–1228.

List of Figures